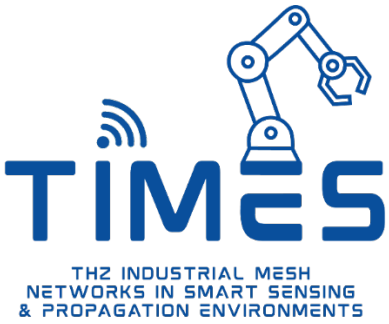

Grant Agreement No: 101096307

Full Title: THz Industrial Mesh Networks in Smart Sensing and Propagation Environments

Start date: 01/01/2023

End date: 31/12/2025

Duration: 36 Months

D3.4

Final Report on Channel Models for industrial environments at sub-THz frequencies

Document Type	Deliverable
Title	D3.4 Final Report on Channel Models for industrial environments at sub-THz frequencies
Contractual due date	30/06/2025 (M30)
Actual submission date	14/07/2025 (M30)
Nature	R
Dissemination Level	SEN
Lead Beneficiary	HWDU
Responsible Author	Mate Boban (HWDU)
Contributions from	Varvara Elesina (TUBS), Carla Reinhardt (TUBS), Alessia Tarozzi (CNIT), Tommaso Zugno (HWDU), Mengfan Wu (HWDU), Antonio D'Amico (CNIT), Luca Antonelli (CNIT), Marco Moretti (CNIT), Giacomo Bacci (CNIT), Tommaso Bacchielli (CNIT), Andrea Giorgetti (CNIT)

Revision history

Version	Issue Date	Changes	Contributor(s)
v0.1	10/04/2025	Initial structure	Mate Boban (HWDU)
v0.2	10/05/2025	Input to sections 2, 3, 4, 5, 6	Varvara Elesina, Carla Reinhardt (TUBS), Alessia Tarozzi (CNIT), Antonio D'Amico (CNIT), Luca Antonelli (CNIT), Marco Moretti (CNIT), Giacomo Bacci (CNIT), Tommaso Bacchielli (CNIT), Andrea Giorgetti (CNIT), Tommaso Zugno (HWDU), Mengfan Wu (HWDU), Mate Boban (HWDU)
V0.3	20/05/2025	Introduction, Scope, Structure, formatting, final comments to contributors	Mate Boban (HWDU)
V0.31	23/05/2025	Further input on RIS and restructuring of the document	Mate Boban (HWDU), Varvara Elesina, Carla Reinhardt (TUBS)
V0.33	04/06/2025	Further input on RIS and 2nd order statistics for THz channels, editorials	Varvara Elesina (TUBS), Tommaso Zugno (HWDU), Mate Boban (HWDU)
V0.34	03/07/2025	Further input on RIS section	Varvara Elesina (TUBS)
V1.1	11/07/2025	Final version	Mate Boban (HWDU)
V1.2	11/07/2025	Final review and acceptance	Luca Sanguinetti (CNIT), Thomas Kurner (TUBS)

Disclaimer

The content of the publication herein is the sole responsibility of the publishers, and it does not necessarily represent the views expressed by the European Commission or its services.

While the information contained in the documents is believed to be accurate, the authors(s) or any other participant in the TIMES consortium make no warranty of any kind with regard to this material including, but not limited to the implied warranties of merchantability and fitness for a particular purpose.

Neither the TIMES Consortium nor any of its members, their officers, employees or agents shall be responsible or liable in negligence or otherwise howsoever in respect of any inaccuracy or omission herein.

Without derogating from the generality of the foregoing neither the TIMES Consortium nor any of its members, their officers, employees or agents shall be liable for any direct or indirect or consequential loss or damage caused by or arising from any information, advice, inaccuracy, or omission herein.

Copyright message

© TIMES Consortium, 2022-2025. This deliverable contains original unpublished work except where clearly indicated otherwise. Acknowledgement of previously published material and of the work of others has been made through appropriate citation, quotation, or both. Reproduction is authorised provided the source is acknowledged.

Table of Contents

List of Abbreviations

AGV Automated Guided Vehicle

AoA / AoD Angle of Arrival / Angle of Departure

ASA / ASD Azimuth Spread of Arrival / Departure

CDL Clustered Delay Line

DBSCAN Density-Based Spatial Clustering of Applications with Noise

GBSCM Geometry Based Stochastic Channel Model

InF Indoor Factory

IRS Intelligent Reflecting Surface (interchangeable with RIS)

ISAC Integrated Sensing and Communications

LoS Line of Sight

MIMO Multiple-Input-Multiple-Output

ML Machine Learning

NLoS Non-Line of Sight

PLE Path Loss Exponent

RF Random Forest (ML classifier)

RIS Reconfigurable Intelligent Surface

RT Ray Tracing

SL / UL Supervised Learning / Unsupervised Learning

THz Terahertz

UE User Equipment

XPR Cross-Polarization Ratio

ZSA / ZSD Zenith Spread of Arrival / Departure

Executive Summary

This deliverable presents a comprehensive study of THz-band channel modeling in industrial environments, forming a critical component for enabling reliable, high-performance wireless communication in future Industry 4.0 applications. Leveraging deterministic, stochastic, and machine-learning approaches, the report delivers insights into the characterization of the unique propagation conditions in industrial settings—especially relevant in the sub-THz frequency domain.

Key contributions include:

- Development and enhancement of deterministic and stochastic models, including those that address near-field, line-of-sight (LoS)/non-line-of-sight (NLoS), and RIS-assisted propagation.
- Integration of advanced ray-tracing simulations calibrated to realistic industrial layouts.
- Use of machine learning techniques for channel feature extraction and multipath component clustering, improving model generalizability and parameter estimation.
- Extension of existing geometry-based stochastic channel models (e.g., 3GPP 38.901 InF) to support THz-specific behavior, validated by empirical measurements.

The insights and models developed through this work are foundational for the design and performance assessment of 6G wireless networks in smart manufacturing and industrial automation.

1 Introduction

Scope

This deliverable outlines the final channel modeling framework developed within the TIMES project for industrial environments at sub-THz frequencies. It addresses the limitations of current models in representing the unique propagation effects in such high-frequency and obstacle-rich settings, providing refined approaches through theory, simulation, measurement, and data-driven methods.

The main objectives of this report are:

- To extend existing channel models to accurately capture key phenomena at THz frequencies in industrial layouts.
- To provide validated modeling techniques incorporating near-field effects, reconfigurable intelligent surfaces (RIS), and integrated sensing and communication (ISAC).
- To develop and apply machine learning methods for dynamic and adaptable channel modeling, including classification, regression, and clustering of multipath components.
- To analyze using ray tracing techniques the path loss, shadowing, and second order statistics of industrial THz channels.

Structure

The rest of the document is structured as follows:

- Section 2 presents extensions to support modeling of THz channels, including near-field propagation, LoS MIMO models, and integrated sensing and communication (ISAC) scenarios.
- Section 3 describes updates to existing channel models based on TIMES measurements, including enhancements to the 3GPP 38.901 Indoor Factory model and application-specific geometry-based stochastic channel models.
- Section 4 focuses on machine learning-based approaches for THz channel modeling, including feature extraction, LoS/NLoS classification, multipath component clustering, and computer vision-based indoor mapping.
- Section 5 reports on channel measurements and modeling of Reconfigurable Intelligent Surfaces (RIS) in the THz band, including initial measurements and ray-tracing-based evaluation.
- Section 6 presents a ray-tracing-based evaluation of path loss and shadow fading in industrial scenarios, supported by numerical simulations and analysis.
- Section 7 concludes the deliverable with key findings and future directions.

2 Extensions to support modeling of THz channels

This section discusses critical theoretical extensions necessary for accurate THz channel modeling in industrial environments. It covers near-field channel effects, line-of-sight (LoS) scenarios, and MIMO communications, while also addressing modeling considerations for integrated sensing and communication (ISAC) systems. The models span from spherical wavefront to planar approximations, enabling more precise characterization at sub-THz frequencies. The extensions and models developed herein are based on the existing literature and adapted to THz bands as needed.

Extensions for modeling THz channels in the near field

LoS Scenario

Consider a narrowband communication system in which the receiver is equipped with *N* antennas and the transmitter is a single-antenna device. We want to derive the expression of the channel coefficient between the transmitter and the receiving antennas, in a free-space propagation scenario, characterized by the absence of scatterers and obstacles. This is the so-called free-space Line of Sight (LoS) propagation scenario.

Far-field and Near-Field Regions of Antennas

We start by reporting the following definitions of *far-field* and *near-field* region of an antenna [**Bal2005**].

- The far-field region "*is that region of the field of an antenna where the angular field distribution is essentially independent of the distance from the antenna.*"
- The near-field region "*is that part of space between the antenna and the far-field region.*"

In the far-field region, the transmitting antenna behaves like a *source point* so that the radiated field can *approximately* be characterized by spherical wave fronts. If the antenna has a maximum dimension L_t, which is large compared to the wavelength, the far-field region is commonly taken to exist at distances greater than $2L_t^2/\lambda$ from the antenna, λ being the wavelength. In practice, L_t can be viewed as the diameter of the smallest sphere that completely contains the antenna. The quantity $2L_t^2/\lambda$ is referred to as the *Fraunhofer distance*.

Consider a point *P* in the far-field region of a transmitting antenna, and let *r* be the distance from the centroid of the antenna to *P*. The received electric field in *P* can be approximated as [**Bal2005**, Eq. (2-92)]

$$\mathbf{E}(P) = -\mathrm{j}kZ_0 i_\mathrm{A} \frac{e^{-\mathrm{j}\frac{2\pi}{\lambda}r}}{4\pi r} \mathbf{l}_{\mathrm{eff}}^{(\mathrm{t})}(\theta_{\mathrm{DoD}}, \phi_{\mathrm{DoD}}) \quad (1)$$

where $k = 2\pi/\lambda$ is the wavenumber, Z_0 is the free-space impedance, i_A is the current feeding the antenna, and $\mathbf{l}_{\mathrm{eff}}^{(\mathrm{t})}(\theta_{\mathrm{DoD}},\phi_{\mathrm{DoD}})$ is the effective length [**Bal2005**, Eq. (2-91)] of the transmit antenna in the direction-of-departure (DoD), identified by the pair $(\theta_{\mathrm{DoD}},\phi_{\mathrm{DoD}})$ of the elevation and azimuth angles (measured with respect to an arbitrary reference system).

Now, assume that the point *P* is the centroid of a receive antenna, and that the electromagnetic wave produced by the transmitting antenna can be approximated by a plane wave. This plane wave approximation can be made provided that the distance between the transmit and receive antenna is greater than $2L_r^2/\lambda$, where L_r represents the maximum dimension of the *receive* antenna. It is worth observing that such a condition is equivalent to the condition that defines the far-field region of the receive antenna. Accordingly,

we can say that the spherical wave front of the transmit antenna can *locally* be approximated with a planar wave front if the transmit antenna is in the far-field region of the receive antenna. Here, *locally* means "in the region occupied by the receive antenna". A pictorial representation of the far-field regions of the transmit and receive antennas is given in **Error! Reference source not found.**. Under the plane-wave approximation, the open-circuit voltage at the receive antenna terminals *h* can be written as [1, Eq. (2-93)]

$$v_{oc} = \mathbf{E}(P) \cdot \mathbf{l}_{eff}^{(r)}(\theta_{DoA}, \phi_{DoA}) \tag{2}$$

where $l_{eff}^{(r)}(\theta_{DoA},\phi_{DoA})$ is the *effective length* of the receive antenna in the direction-of-arrival (DoA) $(\theta_{DoA},\phi_{DoA})$ of the electromagnetic wave, and a · b denotes the dot (or scalar) product between the vectors a and b. Taking (1) into account, we can write

$$v_{oc} = -jZ_0 i_A \sqrt{\beta} e^{-j\frac{2\pi}{\lambda}r} \tag{3}$$

where

$$\beta = \left[k \frac{\mathbf{l}_{eff}^{(t)}(\theta,\phi) \cdot \mathbf{l}_{eff}^{(r)}(\theta,\phi)}{4\pi r} \right]^2 \tag{4}$$

In writing (4), it has been considered that in a LoS scenario the direction-of-departure coincides with the direction-of-arrival, and we have set $\theta_{DoD} = \theta_{DoA} = \theta$ and $\phi_{DoD} = \phi_{DoA} = \phi$. The term β in

(3) accounts for the path-loss (through the factor $1/r^2$) and the polarization loss, due to $\mathbf{l}_{eff}^{(t)}(\theta,\phi) \cdot \mathbf{l}_{eff}^{(r)}(\theta,\phi)$ [**Bal2005**, Sect. 2.12.2]. Based on (3), we define the channel gain as

$$h = \sqrt{\beta} e^{-j\frac{2\pi}{\lambda}r} \tag{5}$$

LoS Channel Model with Antenna Arrays

The derivation of the channel model for the receiver antenna array will be made on the basis of the following assumptions (also, see Figure 1 and Figure 2).

1. Each receiving antenna of the array is located in the far field of the transmitting antenna.
2. The incident electromagnetic wave produced by the transmitting antenna and impinging on a receive antenna of the array can be approximated by a plane wave.
3. The mutual coupling between the array elements is negligible.

Based on the above assumptions and on the results in the previous section, the complex baseband channel from the transmitting antenna to the *n*th receiving antenna can be written as

$$h_n = \sqrt{\beta_n} e^{-j\frac{2\pi}{\lambda}d_n} \qquad n = 0, \ldots, N-1, \tag{6}$$

where β_n accounts for the path loss and the transmit/receive antenna gains, whereas d_n denotes the Euclidean distance between the centers of the transmitting and the *n*-th receiving antenna.

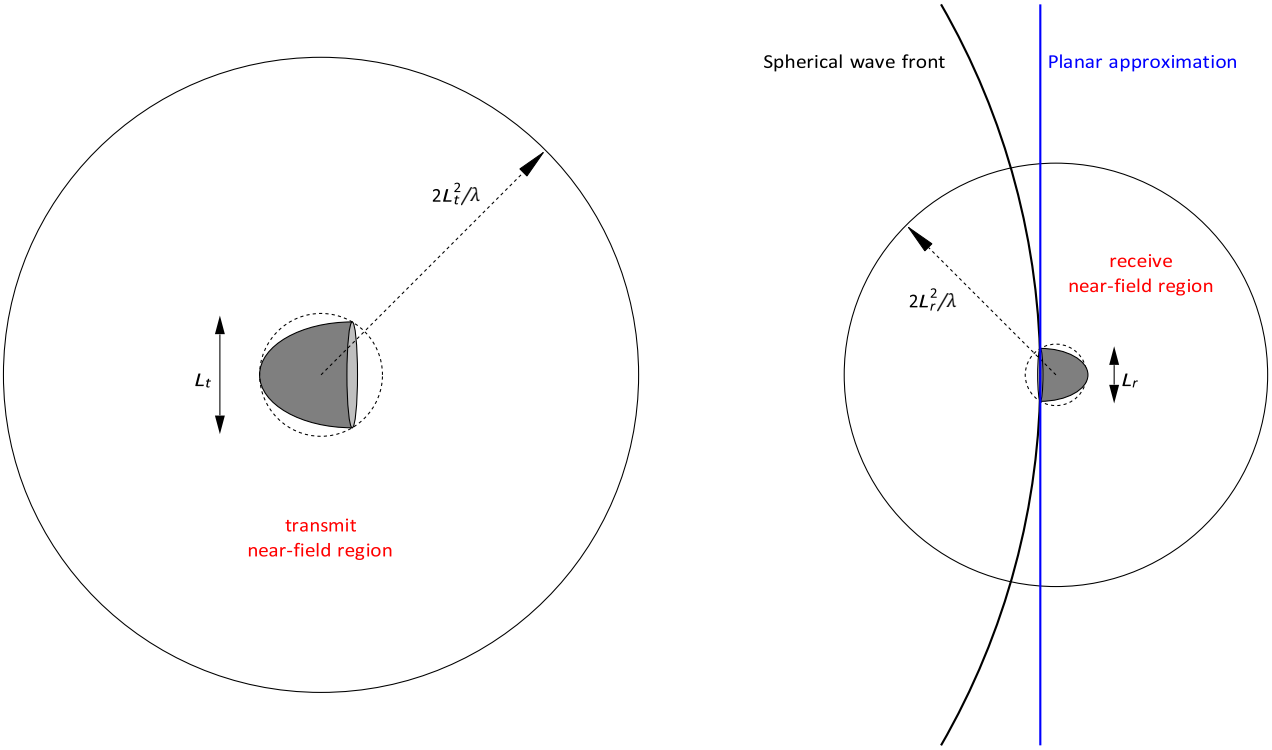

Figure 1 Meaning of Assumptions 1 and 2. Both the transmit and receive antennas are in the far-field regions of each other. At the receive antenna, the spherical wave fronts can be approximated by locally planar wavefronts.

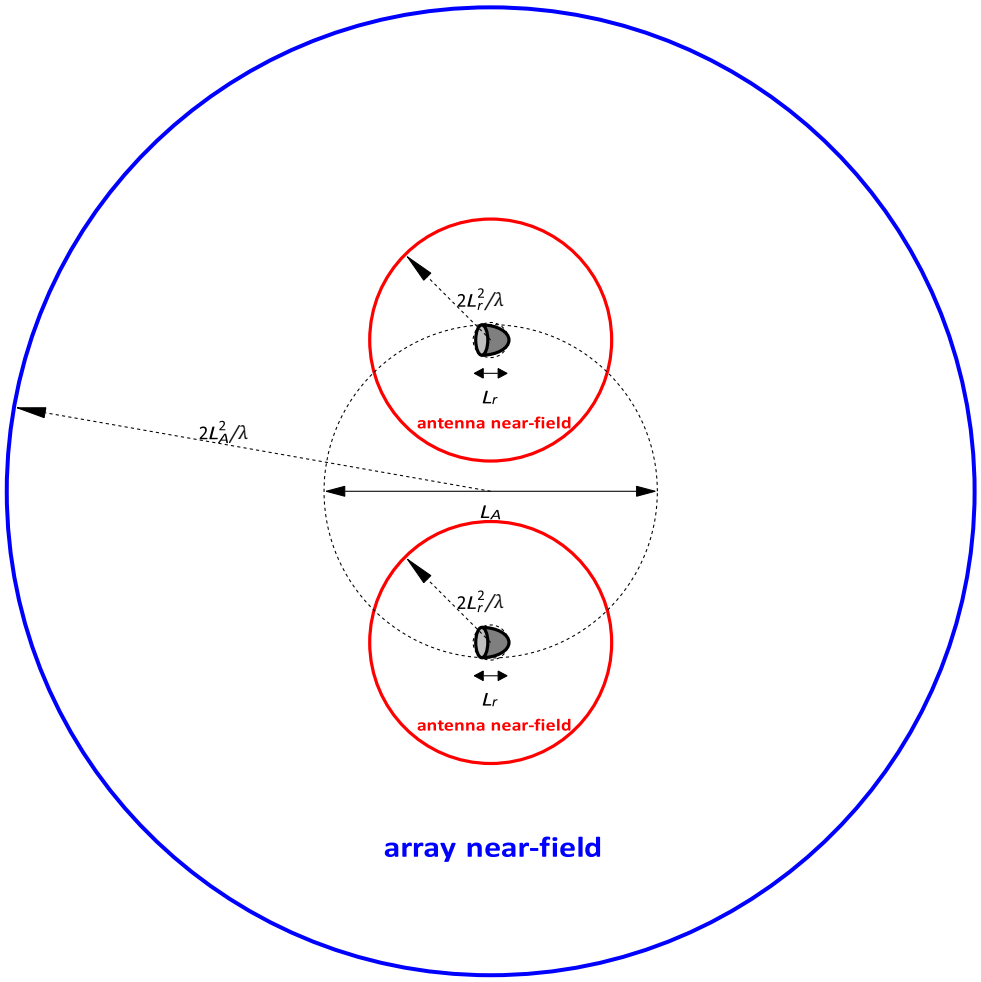

Figure 2 Antenna near-field and array near-field for an array with two antennas.

Alternative LoS Channel Models

When the size of the array is smaller than the transmission distance, two approximations of the channel model can be adopted. The first is the so-called parabolic model [**Do2023**] while the other is the well-known planar model, commonly used in Multiple-Input-Multiple-Output (MIMO) communication systems operating at sub−6 GHz.

Parabolic Wave Front Model

In a cartesian coordinate system *OXYZ*, let s, r_n and c denote the position vectors of the transmit antenna, the *n*th receive antenna, and the center of the receive array, respectively. Accordingly, we can write $r_n = c+\delta_n$, where δ_n is the displacement from c to r_n. Letting $d_C = s-c$ be the displacement from s to c, the distance d_n from the transmitter to the *n*th receive antenna is given by

$$
\begin{aligned}
d_n &= ||\mathbf{s} - \mathbf{r}_n|| = ||\mathbf{d}_C - \delta_n|| \\
&= \sqrt{d_C^2 + \delta_n^2 - 2(\mathbf{d}_C \cdot \delta_n)} \\
&= d_C \sqrt{1 + \frac{\delta_n^2}{d_C^2} - \frac{2(\mathbf{d}_C \cdot \delta_n)}{d_C^2}}
\end{aligned}
\tag{7}
$$

where $d_C = ||\mathbf{d}_C||$ is the distance between the transmitter and the center of the receive array, and $\delta_n = ||\delta_n||$.

Assume now that the transmitter is at a distance much larger than the array size, i.e., $d_C \gg \delta_n$. In this case, we can use the Taylor approximation $\sqrt{1+x} \approx 1 + x/2 - x^2/8$ in (7) to write

$$
\begin{aligned}
d_n &\approx d_C \left\{ 1 + \frac{1}{2}\left[\frac{\delta_n^2}{d_C^2} - \frac{2(\mathbf{d}_C \cdot \boldsymbol{\delta}_n)}{d_C^2}\right] - \frac{1}{8}\left[\frac{\delta_n^2}{d_C^2} - \frac{2(\mathbf{d}_C \cdot \boldsymbol{\delta}_n)}{d_C^2}\right]^2 \right\} \\
&= d_C \left\{ 1 - \frac{\mathbf{d}_C \cdot \boldsymbol{\delta}_n}{d_C^2} + \frac{1}{2}\left[\frac{\delta_n^2}{d_C^2} - \frac{(\mathbf{d}_C \cdot \boldsymbol{\delta}_n)^2}{d_C^4}\right] + o\left(\frac{\delta_n^2}{d_C^2}\right) \right\} \\
&\approx d_C \left\{ 1 - \frac{\mathbf{d}_C \cdot \boldsymbol{\delta}_n}{d_C^2} + \frac{1}{2}\left[\frac{\delta_n^2}{d_C^2} - \frac{(\mathbf{d}_C \cdot \boldsymbol{\delta}_n)^2}{d_C^4}\right] \right\} \\
&= d_C \left\{ 1 - \frac{\delta_n \cos\alpha_n}{d_C} + \frac{1}{2}\left(\frac{\delta_n^2}{d_C^2} - \frac{\delta_n^2 \cos^2\alpha_n}{d_C^2}\right) \right\} \\
&= d_C \left\{ 1 - \frac{\delta_n \cos\alpha_n}{d_C} + \frac{1}{2}\left[\frac{\delta_n^2 (1 - \cos^2\alpha_n)}{d_C^2}\right] \right\} \\
&= d_C - \delta_n \left(\cos\alpha_n - \frac{\delta_n \sin^2\alpha_n}{2 d_C} \right) \triangleq d_n^{(parabolic)}
\end{aligned}
\tag{8}
$$

where $\alpha_n \triangleq \frac{\mathbf{d}_C}{d_C} \cdot \frac{\boldsymbol{\delta}_n}{\delta_n}$. Plugging (8) into (6) the following parabolic model is obtained:

$$
h_n^{(parabolic)} = \sqrt{\beta_n} e^{-j\frac{2\pi}{\lambda} d_n^{(parabolic)}}. \tag{9}
$$

It is worth observing that the dependence of h_n on d_n is much more significant in terms of phase than amplitude. Hence, for the computation of β_n we can safely consider $d_n \approx d_C$.

Planar Wave Front Model

The planar approximation is obtained by considering in (8) only the first order term, i.e.,

$$
d_n^{(planar)} \triangleq d_C - \delta_n \cos\alpha_n \tag{10}
$$

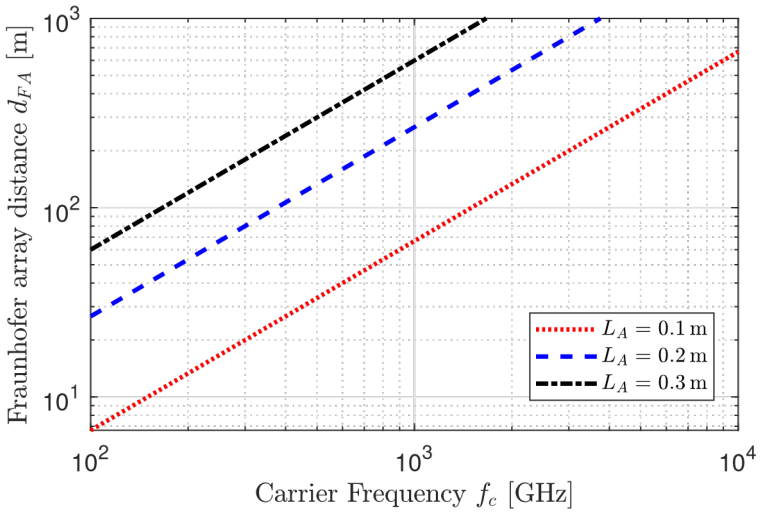

Figure 3 Fraunhofer array distance d_{FA} as a function of the carrier frequency f_c over the whole Terahertz (THz) band.

leading to the planar channel model in the form

$$h_n^{(planar)} = \sqrt{\beta_n} e^{-j\frac{2\pi}{\lambda} d_n^{(planar)}}. \tag{11}$$

Fraunhofer Distance of a Receive Array

Since the second-order approximation terms at the exponent are multiplied by $2\pi/\lambda$, dropping them requires that

$$\frac{2\pi\delta_n^2}{2\lambda d_C} \ll 1$$

or, equivalently,

$$d_C \gg \frac{\pi\delta_n^2}{\lambda}.$$

Denoting by L_A the maximum dimension of the *receive array*[1], the above condition is commonly replaced by

$$d_C \gg \frac{2L_A^2}{\lambda} \triangleq d_{FA} \tag{12}$$

where d_{FA} represents the Fraunhofer distance for the receive array. Accordingly, we can say that the planar approximation represents a valid channel model provided that the transmitter is in the *far-field region of the receive array*. A pictorial explanation of the near-field and far-field regions of an array with two antennas is shown in **Error! Reference source not found.**.

[1] Again, L_A can be viewed as the diameter of the smallest sphere that completely contains the array.

Figure 3 shows the Fraunhofer distance as a function of the carrier frequency $f_c \triangleq c/\lambda$, where c denotes the speed of light in vacuum, for three different values of L_A. We see that with $L_A = 0.1$ m (which could correspond to a planar square array whose side is $0.1/\sqrt{2}$ m) $d_{FA} \approx 20$ m at $f_c = 300$ GHz, and

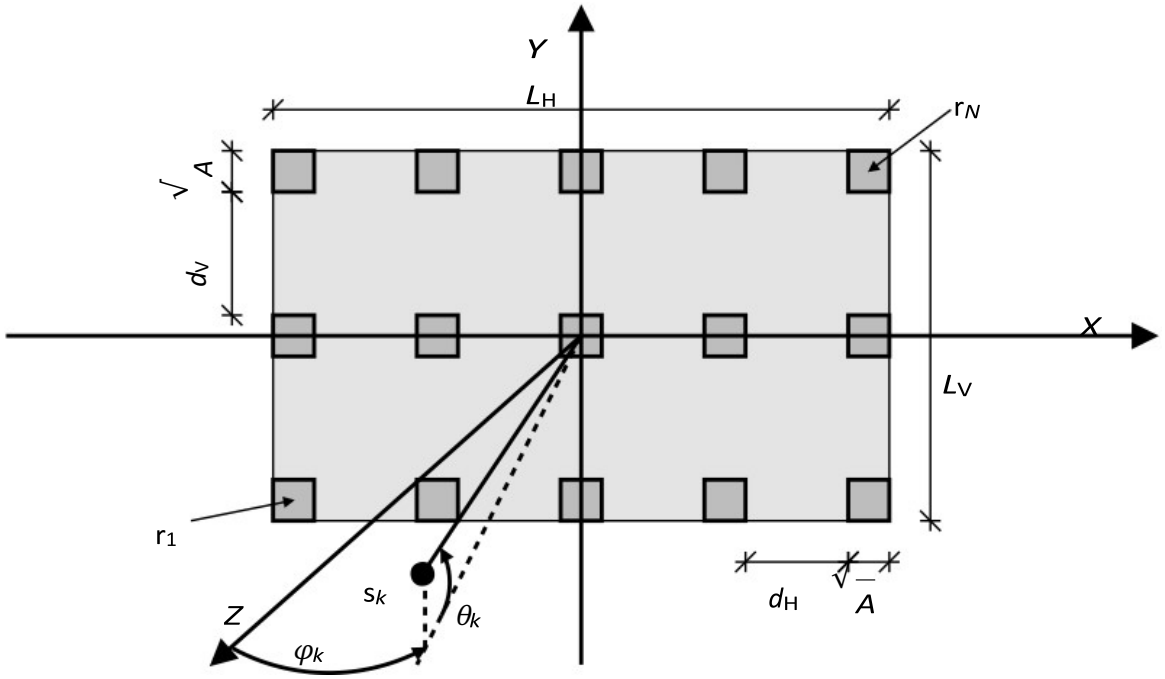

Figure 4 Diagram of the 2D planar array located in the XY -plane.

increases to $d_{FA} \approx 67$ m at $f_c = 1$ THz. These values can be much larger than the typical distances in many practical scenarios.

LoS MIMO Communications

We consider the planar array shown in Figure 4. The array consists of N_V horizontal rows and N_H antennas per row, for a total of $N = N_H N_V$ antennas. Each antenna is a squared patch antenna and has an area A. The spacing (between edges) is d_H and d_V along the horizontal and vertical directions, respectively. Thus, the horizontal and vertical lengths of the array are respectively given by

$$L_H = N_H\sqrt{A} + (N_H - 1)\, d_H \tag{13}$$

$$L_V = N_V\sqrt{A} + (N_V - 1)\, d_V. \tag{14}$$

The antennas are numbered from left to right and from the bottom row to the top row so that antenna n is located at $\mathbf{r}_n = [r_{n,x}, r_{n,y}, 0]^T$, where

$$r_{n,x} = \Delta_H \left(-\frac{N_H - 1}{2} + \mathrm{mod}\,(n-1, N_H) \right) \tag{15}$$

$$r_{n,y} = \Delta_V \left(-\frac{N_V - 1}{2} + \lfloor (n-1)/N_H \rfloor \right) \tag{16}$$

with $\Delta_H = \sqrt{A} + d_H$ and $\Delta_V = \sqrt{A} + d_V$.

Channel Model

To model h, we consider a User Equipment (UE) equipped with a lossless isotropic antenna located at s = $[s_x,s_y,s_z]^T$ that transmits a *Y* -polarized signal when traveling in the *Z* direction. The squared amplitude β_n of the free-space channel coefficient at receive antenna *n*, located at r_n, is given by

[**Bjo2020**, **Bac2023**]

$$\beta_n = \frac{1}{12\pi}\sum_{i=0}^{1}\sum_{j=0}^{1}\frac{g_i\left(s_{k,x}-r_{n,x}\right)g_j\left(s_{k,y}-r_{n,y}\right)\left|s_{k,z}\right|}{\left[g_j^2\left(s_{k,y}-r_{n,y}\right)+s_{k,z}^2\right]\sqrt{g_i^2\left(s_{k,x}-r_{n,x}\right)+g_j^2\left(s_{k,y}-r_{n,y}\right)+s_{k,z}^2}} + \frac{1}{6\pi}\sum_{i=0}^{1}\sum_{j=0}^{1}\tan^{-1}\left(\frac{g_i\left(s_{k,x}-r_{n,x}\right)g_j\left(s_{k,y}-r_{n,y}\right)}{\left|s_{k,z}\right|\sqrt{g_i^2\left(s_{k,x}-r_{n,x}\right)+g_j^2\left(s_{k,y}-r_{n,y}\right)+s_{k,z}^2}}\right) \tag{18}$$

The channel entry h_n, denoting the channel from UE to receive antenna *n*, is obtained as $h_n = \sqrt{\beta_n}e^{-j\psi_n}$

$$\psi_n = 2\pi \bmod \left(\frac{d_n}{\lambda}, 1\right) \tag{19}$$

with $d_n = ||s - r_n||$.

Finally, note that the extensions to support near field for GBSCM system and link level simulations (in particular, extensions for 3GPP TR38.901 [**3GPP2018**]) have been described in Section 0.

Channel modeling considerations for ISAC

Extended Target Model

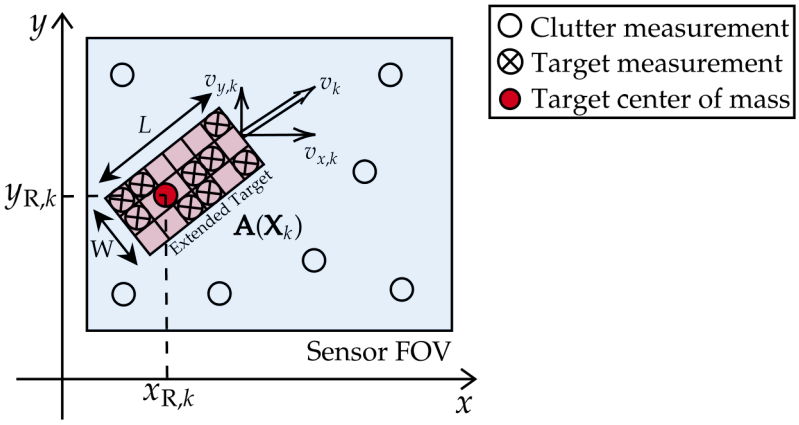

Figure 5 Extended target modeled as a set of scatterers corresponding to grid elements within a rectangular region with fixed size, W and L, and area A.

In this work, as proposed in [**Deh2023**], the target is modeled as a set of grid elements P within a designated rectangular region $\mathbf{A} \subset \mathrm{R}^2$ with a fixed size and an area of $|\mathbf{A}|$, as shown in Figure 5.

At each time step the sensor measurement is made, the extended target is composed of a random number $n_\mathrm{T} < |\mathrm{P}|$ of scatterers. Given that each grid element inside $\mathbf{A}$ can be active, i.e., the target scatterer is localized inside that element, with probability q, the number of active points, or target scatterers, follows a binomial distribution, with probability q and number of trials $|\mathrm{P}|$, i.e., $n_\mathrm{T} \sim B(q,|\mathrm{P}|)$.

But, if we have no detailed knowledge of the extended target, it is a common practice to model the number of target measurements in a frame as a Poisson distribution with mean λ_T. Thus, the proposed extended target model may seem to be in contrast to the Poisson assumption. However, if we consider a finite but very large number of elements on the grid, i.e., $|\mathrm{P}| \to \infty$, each of which is independent active or non-active, the binomial distribution can also be very well approximated by a Poisson distribution, with mean $\lambda_\mathrm{T} = q|\mathrm{P}|$.

General Far/Near-Field Channel Model for Bistatic OFDM-based ISAC

Introduction - System Model

This work considers a bistatic multiple-input multiple-output (MIMO) orthogonal frequency-division multiplexing (OFDM)-based integrated sensing and communication (ISAC) system at THz. In particular, such a system consists of a transmitter (Tx) and a receiver (Rx) to form a bistatic pair, which is used to jointly communicate with user equipments (UEs) and simultaneously localize extended targets in the surrounding environment. The Tx and the Rx can be connected by a fronthaul link to a central unit that coordinates sensing operations, e.g., by performing synchronization between Tx and Rx.

At Tx we assume to illuminate one scanning direction at a time using a beamformer $\mathbf{w} \in \mathrm{C}^{N_\mathrm{t}\times 1}$, where N_t is the number of transmit antennas, and scan the environment from one direction to another using a time division technique. In each direction, we consider that the Tx transmits a frame consisting of M OFDM symbols, for a duration equal to MT_s, and a bandwidth of $B = K\Delta f$, where Δf is the subcarrier spacing, $T_\mathrm{s} \triangleq 1/\Delta f + T_\mathrm{cp}$ is the total OFDM symbol duration including the cyclic prefix, and K is the total number of subcarriers, in order to perform the sensing task, i.e., to illuminate targets. Moreover, we assume that the system operates over a channel with carrier frequency $f_\mathrm{c} \gg B$, such that the narrowband array response assumptions hold [**Tre2002**].

Near/Far Field Channel Model

The proposed channel model is general, thus it is suitable both for near and far-field conditions [**Deh2023**]. In particular, we consider a generic scenario with a single extended target l modeled as set of P scatterers, as explained in Section 2.2.1, and line of sight (LoS) propagation conditions between the transceiver and the scatterers. For the sake of simplicity, we start the channel derivation by considering a single scatterer p located at $\mathbf{p}_p = r_{\mathrm{t},p}\,[cos\phi_{\mathrm{t},p}, sin\phi_{\mathrm{t},p}]^T$ and a transmit uniform linear array (ULA) having N_t elements located at $p_{\mathrm{t},n} = [0,nd]^T$, with $n = -(N_\mathrm{t}-1)/2,\ldots,(N_\mathrm{t}-1)/2$, the transmit antenna index, d the spacing between the elements, here set to half the wavelength, and $r_{\mathrm{t},p}$, $\phi_{\mathrm{t},p}$ respectively the

reference distance and the reference angle of departure (AoD) between the Tx and the scatterer p, calculated with respect to the center of the array.

In LoS conditions, the equivalent low-pass complex channel coefficient for the channel between the single antenna element t_n and the scatterer p at the k-th subcarrier $f_k = f_c + k\Delta f$, with $k = -K/2,\ldots,K/2-1$, and the m-th OFDM symbol can be written as

$$h_{t_n,p}[k,m] = \sqrt{\xi_{t_n,p}} e^{-j(2\pi(\frac{r_{t_n,p}}{c} f_k - mT_s f_{D_{t,p}}) + \varphi_0)} \tag{20}$$

where $f_{D_{t,p}}$ is the Doppler frequency, $r_{t_n,p} = ||\mathbf{p}_p - \mathbf{p}_{t_n}||_2$ is the distance between the t_n-th antenna of the Tx t and the scatterer p, c is the speed of light, $\varphi_0 \in U_{[0,2\pi)}$ is the phase offset between Tx and Rx. Furthermore, $\xi_{t_n,p}$ is the gain factor of the channel between the Tx antenna t_n and the scatterer p, which can be written, considering LoS propagation conditions, as

$$\xi_{t_n,p} = \frac{P_T G_T \sigma_{t,p}}{K 4\pi r_{t_n,p}^2} \tag{21}$$

where P_T is the total transmitted power, G_T is the transmitting antenna gain, and $\sigma_{t,p}$ is the radar cross section (RCS) of the scatterer p, illuminated by the Tx.

The channel vector $\mathbf{h}_{t,p}[k,m] \in C^{1\times N_t}$ associated with subcarrier k and the scatterer p at time instant m, can be obtained by performing simple algebraic manipulations on (20) leading to

$$\mathbf{h}_{t,p}[k,m] = \alpha_{t,p} e^{j2\pi(mT_s f_{D_{t,p}} - k\Delta f \tau_{t,p})} \mathbf{a}^H(\phi_{t,p}, r_{t,p}) \tag{22}$$

where $\alpha_{t,p} = \sqrt{\xi_{t,p}} e^{-j(2\pi f_c \tau_{t,p} + \varphi_0)}$ is the reference channel coefficient associated to scatterer p and computed with respect to the center of the Tx ULA antenna, $\tau_{t,p} = r_{t,p}/c$ is the reference propagation delay, $r_{t,p}$ is the reference scatterer distance, and $\xi_{t,p}$ the reference channel gain, while $\mathbf{a}(\phi_{t,p}, r_{t,p}) \in C^{N_t\times 1}$, is the array response vector, given by

$$\mathbf{a}(\phi_{t,p}, r_{t,p}) = \begin{pmatrix} \frac{r_{t,p}}{r_{t_0,p}} \exp(-j\frac{2\pi f_c}{c}(r_{t_0,p} - r_{tp}) \\ \frac{r_{t,p}}{r_{t_1,p}} \exp(-j\frac{2\pi f_c}{c}(r_{t_1,p} - r_{t,p}) \\ \vdots \\ \frac{r_{t,p}}{r_{t_{N_t-1},p}} \exp(-j\frac{2\pi f_c}{c}(r_{t_{N_t-1},p} - r_{t,p}) \end{pmatrix}. \tag{23}$$

It can be easily proved, that by considering the Fresnel approximation, i.e., the second order Taylor expansion [**Fri2019**], of the relationship between the reference distance $r_{t,p}$ and the distance of the t_n-th Tx antenna element from the scatterer p, and by assuming $nd \ll r_{t,p} \forall n$, $d = \lambda/2$, and $r_{t,p}/r_{t_n,p} \approx 1$, which are reasonable in the far-field, we obtain the well-known array response vector in the far-field

$$\mathbf{a}(\phi_{t,p}) = [e^{-j\frac{N_T-1}{2}\pi \sin\phi_{t,p}}, \ldots, e^{j\frac{N_T-1}{2}\pi \sin\phi_{t,p}}]^T. \tag{24}$$

Similarly, the vector $\mathbf{h}_{p,r}[k,m] \in C^{N_r\times 1}$, representing the channel between the scatterer p and the Rx, consisting of N_r antenna elements, corresponding to the k-th subcarrier at time instant m is given by

$$\mathbf{h}_{p,\mathrm{r}}[k,m] = \beta_{p,\mathrm{r}} e^{j2\pi(mT_{\mathrm{s}}f_{\mathrm{D}_{p,\mathrm{r}}} - k\Delta f \tau_{p,\mathrm{r}})} \mathbf{b}(\theta_{p,\mathrm{r}}, \gamma_{p,\mathrm{r}}) \tag{25}$$

where $\tau_{p,\mathrm{r}} = \gamma_{p,\mathrm{r}}$ is the reference propagation delay from the scatterer p to the center of the Rx antenna array, $\beta_{p,\mathrm{r}} = \sqrt{\zeta_{p,\mathrm{r}}} e^{-j2\pi f_{\mathrm{c}} \tau_{p,\mathrm{r}}}$ is the channel coefficient, and $\mathbf{b}(\theta_{p,\mathrm{r}},\gamma_{p,\mathrm{r}}) \in \mathrm{C}^{N_{\mathrm{r}}\times 1}$ is the array response vector defined in (23), with $\theta_{p,\mathrm{r}}$ the reference angle of arrival (AoA). Considering LoS propagation conditions and isotropic antenna elements with effective area $A = c^2/(4\pi f_{\mathrm{c}}^2)$, the gain factor $\zeta_{p,\mathrm{r}}$ can be written as

$$\zeta_{p,\mathrm{r}} = \frac{c^2}{(4\pi f_{\mathrm{c}} \gamma_{p,\mathrm{r}})^2}. \tag{26}$$

In the end, the generalized near/far-field $N_{\mathrm{r}} \times N_{\mathrm{t}}$ bistatic MIMO channel between the Tx and the Rx, considering the presence of P scatterers from an extended target, at k-th subcarrier and m-th time instant can be written as

$$\begin{aligned} \mathbf{H}_{\mathrm{t,r}}[k,m] &= \sum_{p=1}^{P} \epsilon_p e^{j2\pi(mT_{\mathrm{s}}f_{\mathrm{D}_p} - k\Delta f \tau_p)} \\ &\times \mathbf{b}(\theta_{p,\mathrm{r}}, \gamma_{p,\mathrm{r}}) \mathbf{a}^{\mathrm{H}}(\phi_{\mathrm{t},p}, r_{\mathrm{t},p}) \end{aligned} \tag{27}$$

where $\epsilon_p = \alpha_{\mathrm{t},p}\beta_{p,\mathrm{r}}$ and $\tau_p = \tau_{\mathrm{t},p} + \tau_{p,\mathrm{r}}$ are the bistatic complex channel factor and bistatic propagation delay, respectively, associated with the p-th scatterer, while f_{D_p} is the bistatic Doppler shift, defined as

$$f_{\mathrm{D}_p} = f_{\mathrm{D}_{\mathrm{t},p}} + f_{\mathrm{D}_{p,\mathrm{r}}} = \frac{2v_p}{\lambda} \cos\delta \cos\beta/2 \tag{28}$$

where v_p is the modulus of the relative velocity of scatterer p, while β and δ are the bistatic angle and the angle between the velocity direction and the bistatic bisector, respectively.

Input-Output Relationship

The continuous-time OFDM signal transmitted from Tx to the extended target l is defined as

$$\mathbf{s}_{\mathrm{t},p}(t) = \mathbf{w}_l \sum_{k=0}^{K-1} \sum_{m=0}^{M-1} x_{\mathrm{t},p}[k,m] g_{k,m}(t) \tag{29}$$

where $\mathbf{w}_l$ is a (unit-norm) transmit beamforming (in the far-field) or beam-focusing (in the near-field) vector to point toward the extended target l, and $x_{\mathrm{t},p}[k,m]$ is a generic complex modulation symbol of the $K \times M$ OFDM resource grid used at the Tx to estimate range, angle, and velocity parameters of the scatterer p, while $g_{k,m}(t)$ is the modulating pulse.

The noise-free continuous-time signal transmitted by Tx, scattered by p, and received from the Rx is given by

$$\mathbf{r}_{\mathrm{t,r}}(t) = \sum_{p=1}^{P} \epsilon_p e^{j2\pi f_{\mathrm{D}_p} t} \mathbf{b}(\theta_{p,\mathrm{r}}, \gamma_{p,\mathrm{r}}) \mathbf{a}^{\mathrm{H}}(\phi_{\mathrm{t},p}, r_{\mathrm{t},p}) \mathbf{s}_{\mathrm{t},p}(t - \tau_p) \tag{30}$$

Then, after the OFDM demodulator, considering negligible inter-carrier interference (ICI) and inter-symbol interference (ISI) and including noise, a received time-frequency grid of complex elements $y[k,m]$ is obtained at each antenna element. Therefore, considering the channel model in (27), the vector $\mathbf{y}$ of received complex modulation symbols of dimension $N_{\mathrm{r}} \times 1$ is given by

$$\begin{aligned} \mathbf{y}[k,m] &= \mathbf{H}_{\mathrm{t,r}}[k,m]\mathbf{w}_l x_{\mathrm{t},p}[k,m] \\ &= \sum_{p=1}^{P} \epsilon_p \mathbf{b}(\theta_{p,\mathrm{r}}, \gamma_{p,\mathrm{r}}) \mathbf{a}^{\mathrm{H}}(\phi_{\mathrm{t},p}, r_{\mathrm{t},p}) \mathbf{w}_l x_{\mathrm{t},p}[k,m] \\ &\times \quad e^{j2\pi(mT_{\mathrm{s}} f_{\mathrm{D}_p} - k\Delta f \tau_p)} + \tilde{\mathbf{n}}[k,m] \end{aligned} \tag{31}$$

where $\tilde{\mathbf{n}} \sim \mathcal{CN}(\mathbf{0}, \sigma_{\tilde{\mathbf{n}}}^2 \mathbf{I}_{N_{\mathrm{r}}})$ is the complex Gaussian noise.

By stacking the $K \times M$ OFDM transmitted symbol grid into a $KM \times 1$ vector $\underline{\mathbf{x}}$, the received signal $\underline{\mathbf{y}} \in \mathbb{C}^{N_{\mathrm{r}}KM \times 1}$ can be rewritten as

$$\underline{\mathbf{y}} = \sum_{p=1}^{P} \epsilon_p \mathbf{G}(f_{\mathrm{D}_p}, r_{\mathrm{t},p}, \gamma_{p,\mathrm{r}}, \theta_{p,\mathrm{r}}, \phi_{\mathrm{t},p}) \underline{\mathbf{x}} + \underline{\tilde{\mathbf{n}}} \tag{32}$$

where $\mathbf{G}(\cdot)$ is the effective channel matrix of dimension $N_{\mathrm{r}}KM \times KM$, defined for a single scatterer p, as

$$\begin{aligned} &\mathbf{G}(f_{\mathrm{D}_p}, r_{\mathrm{t},p}, \gamma_{p,\mathrm{r}}, \theta_{p,\mathrm{r}}, \phi_{\mathrm{t},p}) \triangleq \\ &\mathbf{T}(\tau_p, f_{\mathrm{D}_p}) \otimes \left(\mathbf{b}(\theta_{p,\mathrm{r}}, \gamma_{p,\mathrm{r}}) \mathbf{a}^{\mathrm{H}}(\phi_{\mathrm{t},p}, r_{\mathrm{t},p}) \mathbf{w}_l\right) \end{aligned} \tag{33}$$

with $\mathbf{T}(\tau_p, f_{\mathrm{D}_p}) \in \mathbb{C}^{KM \times KM}$ defined as

$$\begin{aligned} \mathbf{T}(\tau_p, f_{\mathrm{D}_p}) = \mathrm{diag}\Big(&[1, \ldots, e^{j2\pi m T_{\mathrm{s}} f_{\mathrm{D}_p}}, \ldots, e^{j2\pi(M-1)T_{\mathrm{s}} f_{\mathrm{D}_p}}]^{\mathrm{T}} \\ &\otimes [1, \ldots, e^{-j2\pi k \Delta f \tau_p}, \ldots, e^{-j2\pi(K-1)\Delta f \tau_p}]^{\mathrm{T}} \Big). \end{aligned} \tag{34}$$

3 Updates to existing channel models based on TIMES results

This section provides updates to existing channel models (specifically, 3GPP 38.901 Indoor Factory model and application-specific GBSCM models) based on extensive measurements performed within TIMES.

Updates to 3GPP 38.901 Indoor Factory (InF) geometry based stochastic model

InF model was developed based on channel measurements and ray tracing simulations in different industrial settings, with supported frequencies ranging between 0.5 GHz and 100 GHz. This section summarizes the updates to Indoor Factory (InF) channel model as defined by 3GPP TR38.901 [**3GPP2018**], in particular new measurement-based parameters for path loss and large-scale parameters (extracted from the measurements performed in industrial environments within SNS TIMES), as well as extensions to support near-field channel effects.

Modification of 3GPP InF-SL parameters based on TIMES THz measurements

We performed simultaneous multi-band ultra-wideband dual-polarized double-directional measurements at sub-6 GHz (center frequency, 6.25 GHz), mmWave (74.25 GHz), and sub-THz (308.2 GHz) in LOS and NLOS in an industrial setting depicted in Figure 6 and detailed in [**TIMES2023-2**]. Referring to the InF scenarios defined in [**3GPP2018**], this environment best matches the InF-SL (sparse clutter, low BS) scenario.

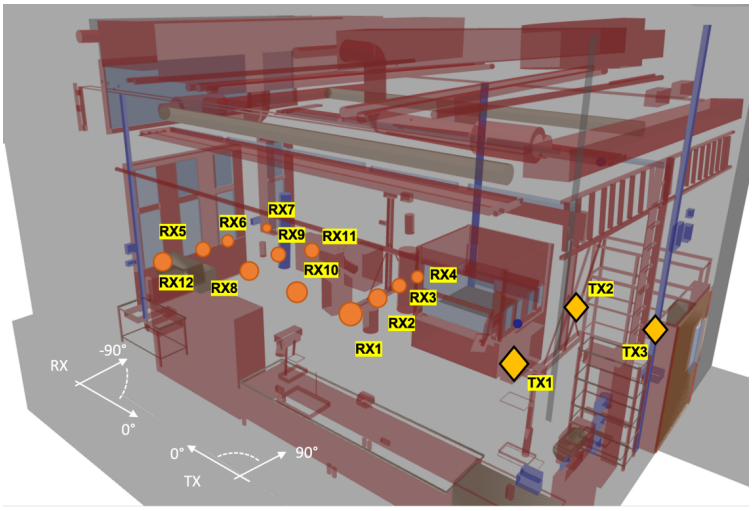

Figure 6 THz channel measurements in industrial setting.

Based on the channel measurement results, we modified the path loss equation and some of the fast-fading channel parameters of the 3GPP procedure from [**3GPP2018**] for each of the three frequencies, the one in 308.2 GHz being of particular relevance. If using the 3GPP model to simulate THz channels, we suggest the following:

- Implementing parameters specified in Table 1 and Table 2 into the 3GPP channel coefficient generation procedure [**3GPP2018**];
- For parameters not specified in Table 1 and Table 2, using existing InF parameters defined in [**3GPP2018**] for 0.5-100 GHz.

Table 1 Multi-band Large Scale Parameters (LSPs) in industrial settings for LOS and NLOS.

		DS				ASA				ASD			
		LOS		NLOS		LOS		NLOS		LOS		NLOS	
		$\mu_{\lg DS}$	$\sigma_{\lg DS}$	$\mu_{\lg DS}$	$\sigma_{\lg DS}$	$\mu_{\lg ASA}$	$\sigma_{\lg ASA}$	$\mu_{\lg ASA}$	$\sigma_{\lg ASA}$	$\mu_{\lg ASD}$	$\sigma_{\lg ASD}$	$\mu_{\lg ASD}$	$\sigma_{\lg ASD}$
Measurements	6.75 GHz	-8.32	0.29	-8.11	0.13	1.61	0.18	1.69	0.15	1.35	0.04	1.73	0.18
	74.25 GHz	-8.33	0.30	-8.09	0.27	1.44	0.36	1.65	0.26	1.18	0.24	1.65	0.23
	305.27 GHz	-8.24	0.42	-8.12	0.19	1.57	0.27	1.71	0.25	1.52	0.24	1.74	0.17
3GPP TR 38.901 InF-SL	6.75 GHz	-7.69	0.15	-7.60	0.19	1.62	0.31	1.72	0.30	1.56	0.25	1.57	0.20
	74.25 GHz					1.44	0.43						
	305.27 GHz					1.33	0.50						

Table 2 ABG pathloss parameters from standards and TIMES measurements

Model	**Visibility**	α	β	γ	σ
Measurements	LOS	2.28	30.7	2.06	1.27
	NLOS	0.22	53.74	2.12	5.52
3GPP TR38.901 InF-SL	LOS	2.15	31.84	1.9	4.3
	NLOS	2.55	33	2	5.07
ITU-R P.1238-11	LOS	2.31	24.52	2.06	2.69
	NLOS	3.79	21.01	1.34	9.05

Extension for considering near-field channel effects

In Section 2.1, we provided the theoretical background to treat the near-field channel modeling and have discussed how the single-tap channel considers the near-field effect. In this section, we extended the discussion to model the near-field effect in multipath channels. In particular, we extend the 3GPP TR38.901 channel model to support near-field channel modeling.

In the Fresnel region, the plane wave approximation is no longer valid and a spherical wavefront model should be used instead. In this case, the wave vector $\vec{k}(x, y, z)$ is no longer constant but varies in the space. As a consequence, $\vec{k}(x, y, z)$ impinges each antenna element with a different direction which depends not only on the incident angle but also on the radius of the spherical wavefront r_w. Figure 7 represents the phase variation over a 64×64 UPA computed with planar and spherical wavefront models, and $r_w = 0.01 \cdot d_{FA}$. Figure 7-c represents the phase error caused by the planar wavefront assumption.

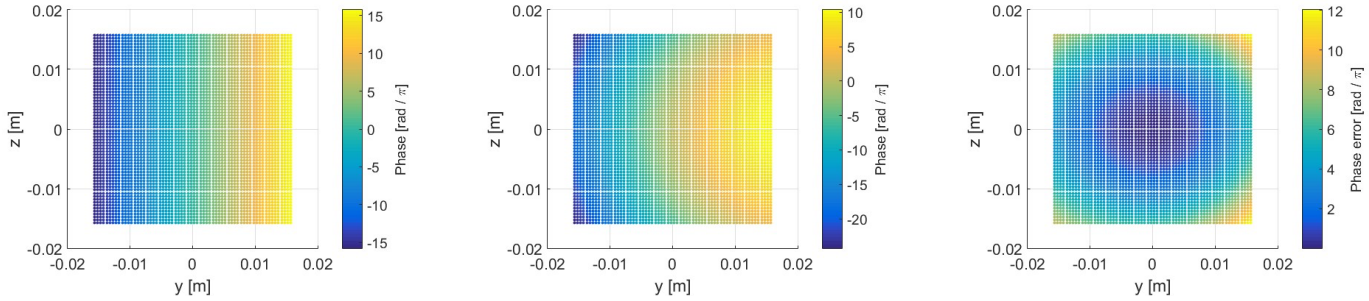

(a) Planar model. (b) Spherical model. (c) Approximation error.

Figure 7: Phase variation over a 64×64 UPA computed with planar and spherical wavefront models, and approximation error due to the planar wavefront assumption.

In the following, we discuss how the channel model in 3GPP TR38.901 can be extended to support the modeling of spherical wavefronts introduced in Section 2. We only consider the effects of wave's curvature on the phase, while we neglect any amplitude variation. This condition is satisfied when $r_w \geq d_B$, where $d_B = 2D\sqrt{N}$ is the Bjornson distance [Bjo2021]. We notice that for large arrays, d_B is much shorter than d_{FA} as it increases with the squared root of the number of elements. A geometric representation of the proposed extension is depicted in Figure 8.

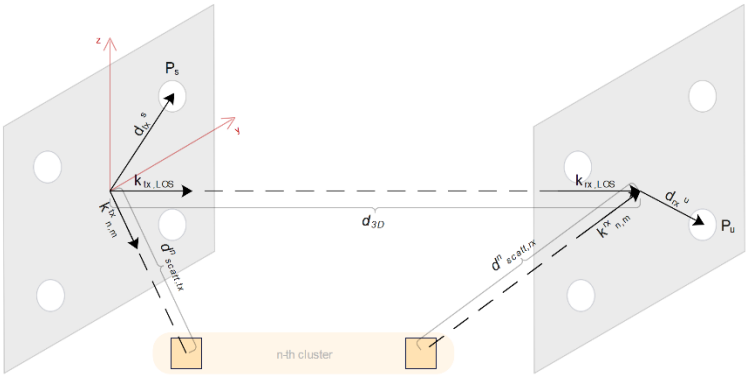

Figure 8 Representation of the proposed extension.

LOS component

The channel impulse response of the LOS path between s-th transmit and the u-th receive elements is expressed as

$$\begin{aligned} h_{u,s}^{LOS}(t,\tau) &= e^{-\frac{j2\pi}{\lambda}d_{3D}} e^{\frac{j2\pi}{\lambda}\Delta\Phi_{LOS}^{s,u}} \delta(\tau - \tau_{LOS}) \\ &= e^{-\frac{j2\pi}{\lambda}d_{3D}} e^{\frac{j2\pi}{\lambda}\Delta\Phi_{tx,LOS}^{s}} e^{\frac{j2\pi}{\lambda}\Delta\Phi_{rx,LOS}^{u}} \delta(\tau - \tau_{LOS}), \end{aligned}$$

where d_{3D} corresponds to the distance between the center of the transmit and receive arrays, λ is the wavelength, τ_{LOS} is the delay of the LOS path, and $\Delta\Phi_{LOS}^{s,u} = \Delta\Phi_{tx,LOS}^{s} + \Delta\Phi_{rx,LOS}^{u}$ represents the phase variation due to the array geometries.

When adopting a spherical wavefront model, the phase variation $\Delta\Phi_{LOS}^{s,u}$ is equivalent to the distance between the s-th transmit and u-th receive antenna elements. By setting the origin of the coordinate system at the center of the transmit array, the position of the *s*-th transmit element is $P_s = \vec{d}_{tx}^{s}$, while the position

of the *u*-th receive element is $P_u = d_{3D} \cdot \vec{k}_{tx,LOS} + \vec{d}_{rx}^{u}$, where $\vec{k}_{tx,LOS}$ is the spherical unit vector of the LOS ray. Then, the phase excitation can be computed as

$$\begin{aligned} \Delta\Phi_{LOS}^{s,u} &= d_{3D} - ||P_s - P_u|| \\ &= d_{3D} - ||\vec{d}_{tx}^{s} - d_{3D} \cdot \vec{k}_{tx,LOS} - \vec{d}_{rx}^{u}||, \end{aligned} \tag{35}$$

where a normalization with respect to d_{3D} is needed to avoid a double contribution of the phase shift due to the propagation distance.

NLOS components

The channel impulse response for the NLOS components between the s-th transmit and u-th receive antenna elements can be expressed as

$$h_{u,s}^{NLOS}(t,\tau) = \sum_{n=1}^{N} \sum_{m=1}^{M} \sqrt{\frac{P_n}{M}} e^{\frac{j2\pi}{\lambda}\Delta\Phi_{tx,n,m}^{s}} e^{\frac{j2\pi}{\lambda}\Delta\Phi_{rx,n,m}^{u}} \delta(\tau - \tau_n),$$

where *N* is the number of clusters, *M* is the number of rays, P_n is the cluster power, τ_n is the cluster delay, and the terms $\Delta\Phi_{tx,n,m}^{s}$ and $\Delta\Phi_{rx,n,m}^{u}$ represents the phase excitation of path *m* in cluster *n* due to the transmit and receive array geometries.

For the NLOS components, C_w corresponds to the position of the first (in case of departing wave) or last (in case of arriving wave) scatterer, as represented in Figure 8. Therefore, the phase excitation can be expressed as:

$$\Delta\Phi_{tx,n,m}^{s} = d_{scatt,tx}^{n} - d_{scatt,tx}^{n,s} \tag{36}$$

$$\Delta\Phi_{rx,n,m}^{u} = d_{scatt,rx}^{n} - d_{scatt,rx}^{n,u} \tag{37}$$

where $d_{scatt,tx}^{n,s}$ is the distance between the *s*-th antenna element at the transmitter and the first scatterer hit by cluster *n*, $d_{scatt,tx}^{n}$ is the distance between the center of the transmit array and the first scatterer hit by cluster *n*, $d_{scatt,rx}^{n,u}$ is the distance between the *u*-th antenna element at the receiver and the last scatterer hit by cluster *n*, and $d_{scatt,rx}^{n}$ is the distance between the center of the receive array and the last scatterer hit by cluster *n*. Eq. 36 and 37 can be written as:

$$\Delta\Phi_{tx,n,m}^{s} = d_{scatt,tx}^{n} - ||d_{scatt,tx}^{n} \cdot \vec{k}_{tx,n,m} - \vec{d}_{tx,s}|| \tag{38}$$

$$\Delta\Phi_{rx,n,m}^{u} = d_{scatt,rx}^{n} - ||d_{scatt,rx}^{n} \cdot \vec{k}_{rx,n,m} - \vec{d}_{rx,u}|| \tag{39}$$

where $\vec{k}_{tx,n,m}$ and $\vec{k}_{rx,n,m}$ are the spherical unit vector of the m-th ray belonging to the n-th cluster, for the transmitter and receiver. Here we make an implicit assumption that all rays belonging to the same cluster interact with the same scattering objects. This is reasonable since all rays in a cluster experience the same propagation delay[2].

To apply Eq. 38 and 39, we need to determine the distances $d_{scatt,tx}^{n}$ and $d_{scatt,rx}^{n}$ between the center of the transmit (receive) array and the first (last) scattering objects. The 3GPP framework does not provide any explicit modeling of the scattering object, therefore $d_{scatt,tx}^{n}$ and $d_{scatt,rx}^{n}$ cannot be determined directly. A possible approach is the one proposed in [Jae2014], which involves the solution of an optimization problem

[2] 3GPP TR 38.901 subdivides the three strongest NLOS clusters into sub-clusters with different propagation delays. In this case, the same formulation applies at a sub-cluster level.

for determining $d^n_{scatt,tx}$ and $d^n_{scatt,rx}$ such that the distance between the first bounce and last bounce scatterer is minimized. Another approach is to regard these quantities as random variables whose distribution is derived from simple geometrical considerations. From the propagation delay, we can compute the propagation distance of the n-th cluster as $d_n = \tau_n \cdot c + d_{3D}$, where c is the speed of light and d_{3D} is the 3D distance between the transmit and receive arrays. d_n represents an upper bound for determining $d^n_{scatt,tx}$ and $d^n_{scatt,rx}$, because the overall propagation distance is greater or equal to the sum of lengths of the first and last segments:

$$d^n_{scatt,tx} + d^n_{scatt,rx} <= d_n \tag{40}$$

The equality is reached when cluster *n* interacts with a single scatterer before reaching the receiver. Based on these consideration, $d^n_{scatt,tx}$ and $d^n_{scatt,rx}$ can be determined with the following procedure:

1. compute the overall propagation distance as $d_n = \tau_n \cdot c + d_{3D}$;
2. draw $d^n_{scatt,tx} \sim U[d_B, d_n - d_B]$;
3. draw $d^n_{scatt,rx} \sim U[d_B, d_n - d^n_{scatt,tx}]$.

where the lower bound is set to d_B to avoid significant amplitude variations over the array caused by the wave's curvature.

To include the modeling of spherical wavefronts, the procedure should be extended as shown in Figure 9. In particular, an additional step after step 5 is needed for computing the terms $d^n_{scatt,tx}$ and $d^n_{scatt,rx}$ as described above. Moreover, step 11 has to be modified for computing the phase components $\Delta\Phi^{s,u}_{LOS}$, $\Delta\Phi^{s}_{tx,n,m}$, and $\Delta\Phi^{u}_{rx,n,m}$ using Eq. 35, 38, and 39.

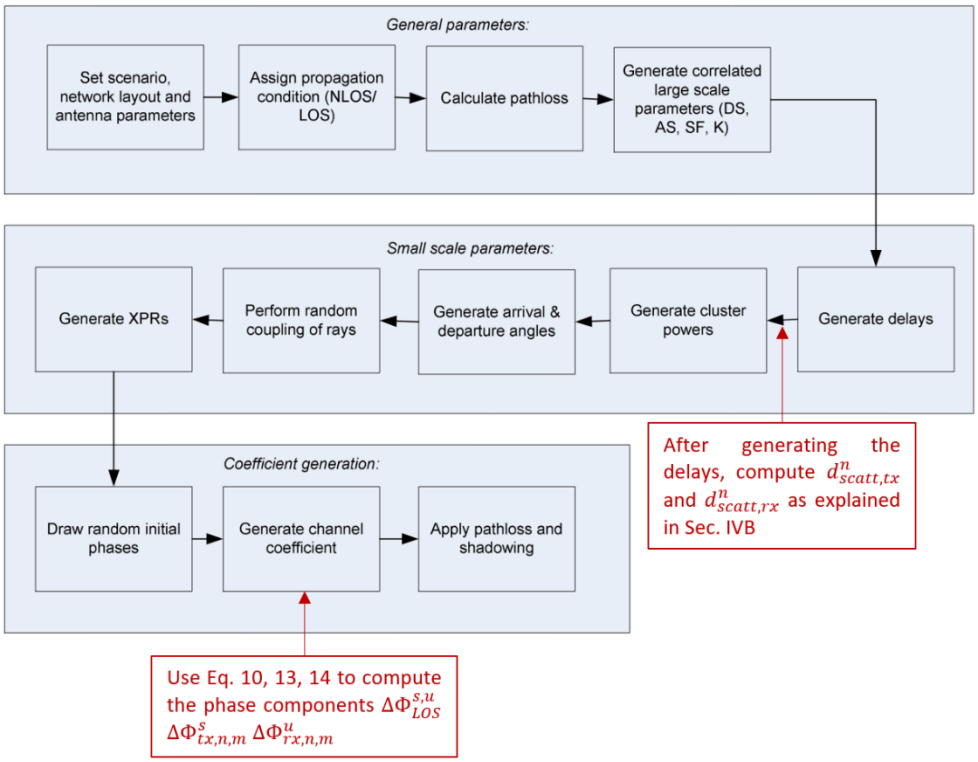

Figure 9 Modified channel coefficient generation procedure.

To validate the proposed extension, we simulated two nodes placed at a distance d and of the same height. The receiver is equipped with a 64×64 array, while the transmitter has a single-element antenna. The channel modeling parameters are selected according to the UMa scenario and the operating frequency is set to 300 GHz. We varied the distance d between $0.1 \cdot d_{FA}$ and $2 \cdot d_{FA}$, generating 100 independent channel realizations at each step. For each realization, we evaluated the phase error experienced by the element at the upper-right corner of the array caused by LOS and NLOS paths. The motivation behind this choice is that elements at the border of the array are more affected by the effect of spherical wavefronts.

The results are shown in Figure 10. The yellow line represents the approximation error of the LOS path, computed as the difference between the phase components calculated with the original model (i.e., following the plane-wave approximation) and with the extended model (i.e., including the modeling of spherical wavefronts). Instead, blue line represents the approximation error of NLOS paths averaged over all independent channel realizations. For a single realization, the approximation error of NLOS paths is computed as:

$$\epsilon = \sum_{n=1}^{N} \frac{P_n}{M} \sum_{m=1}^{M} \left| \Delta\Phi_{rx,n,m}^{FF} - \Delta\Phi_{rx,n,m}^{NF} \right|,$$

where $\Delta\Phi_{rx,n,m}^{FF}$ corresponds to the phase component calculated with the original model, while $\Delta\Phi_{rx,n,m}^{NF}$ corresponds to the phase component calculated with the proposed extension.

It can be seen that the approximation error decreases as d increases, because the radius of the spherical waves increases and plane wave model is approached at the limit. When d is larger than the Fraunhofer array distance d_{FA}, the phase error is smaller than π/8 (red dashed line), which corresponds to the maximum error in the far-field approximation. For short distances, the phase error of the LOS path is larger than the average phase error of NLOS paths, because it is more likely that scatterers are at a distance greater than the LOS distance d. For large d, the order of the curves flips because the probability of having scatterers that are closer to the transmitter or receiver than the LOS distance is increased.

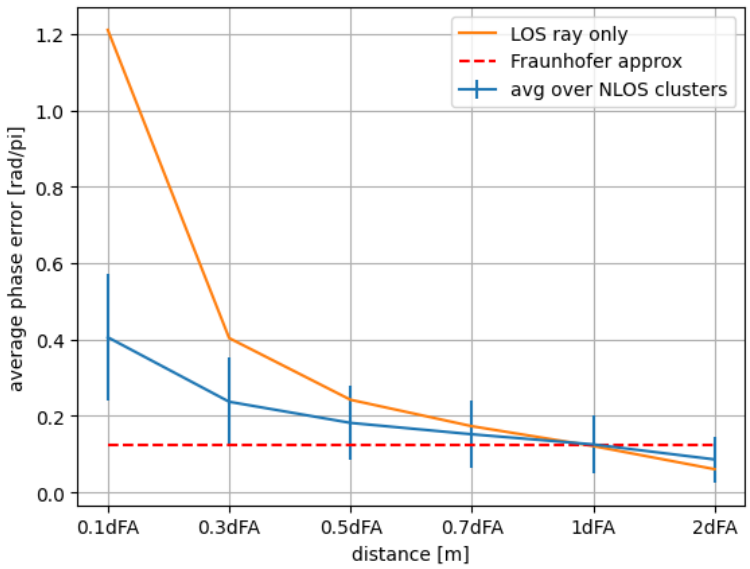

Figure 10 Phase approximation error over distance.

Updates to application-specific GBSCM models

In TIMES IR3.1 [**TIMES2023-3**], THz Geometric Based Stochastic Channel Model (GBSM) for Indoor Office was described. This model was developed by TU Braunschweig Institute of Communication Technologies and allows modeling in broadband frequency domain and in time domain with considering spatial channel characteristics. Model was introduced for the frequency range from 275 to 325 GHz [**Pri2013-2**].

However, provided model parameters have been obtained for a particular office. In this case, the idea is to use the same approach but for comprehensive industrial workspace in which measurements presented in D3.1 [**TIMES2023-2**] were performed. Although channel measurements in the environment of interest have already been performed, it is also necessary to use ray tracing (RT) to create a comprehensive dataset, which is important for the implementation of the stochastic model. For the propagation modeling Simulator for Mobile Networks (SiMoNe) RT tool is planned to be used. SiMoNe is a platform that was developed by TUBS and includes: a system-level simulator, a link-level simulator and a ray tracing tool. This tool was described in detail in TIMES D2.2 [**TIMES2023-4**].

Scenario description: The scenario of the interest reproduced THz wireless communication between an access point (AP) located on the wall, and sensor nodes (SN) on the machines in an industrial environment. This environment is a comprehensive industrial workspace with various types of machinery, metal surfaces, non-standard ceilings, and different height levels (Figure 11). A schematic view of the workspace is shown in Figure 12. The workspace has dimensions 36m x 22m x 11m, height of the upper level is 4m, height of the suspended ceilings (beams) is 7.3m. All other dimensions can be obtained from the schematic view. To simplify the description of length, two walls were designated as Reference walls (Wall 1 and Wall 2, Figure 12). The part of the workspace where measurements were taken, and which is the most interesting for modeling, is marked by a red square.

A simplified 3D model of the environment, intended to serve as a starting point for further RT simulation, is shown in Figure 13.

Figure 11 Industrial workspace.

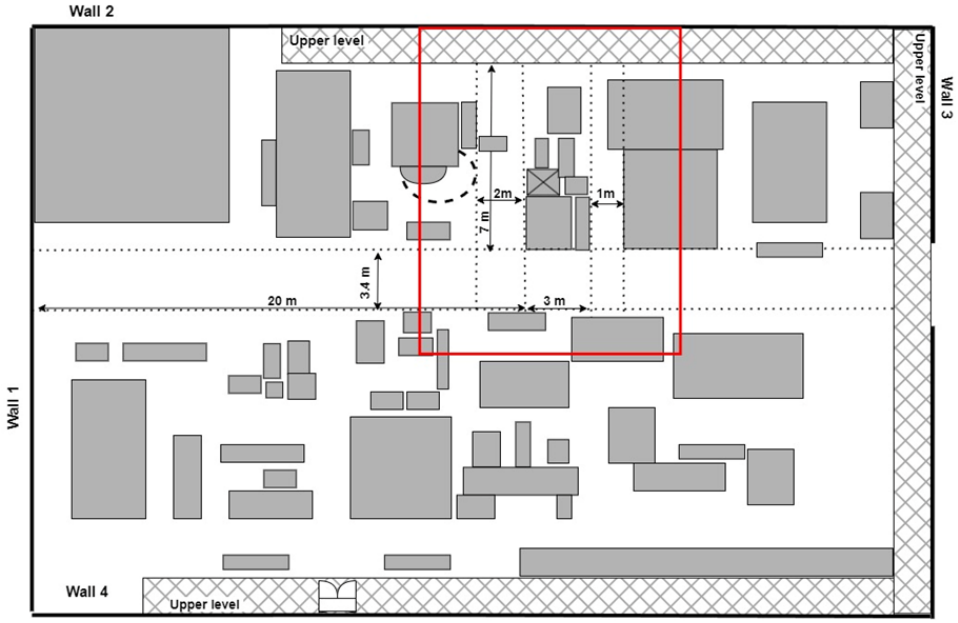

Figure 12 Industrial workspace schematic view.

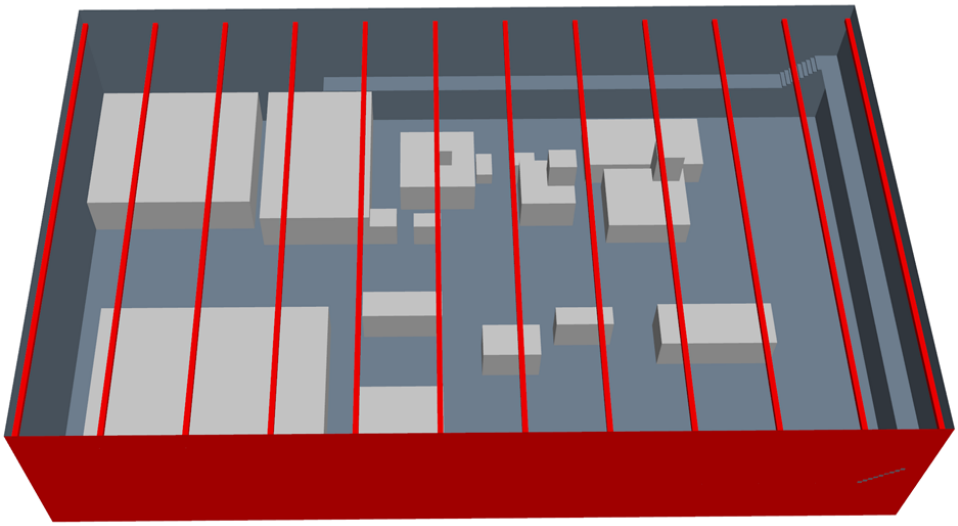

Figure 13 Simplified 3D model of the investigated industrial workspace environment.

Channel measurements setup is presented in the Figure 14. The transmitter (Tx) represented AP and the receiver (Rx) represented SN. Tx was fixed on the tripod and located on the upper level of the workspace. Rx unit was fixed on the tripod and located on the bottom level. There were 4 different positions of Rx. Two of them were positioned on one side of the massive machine, and the other two were positioned on the opposite side.

The setup parameters are presented in Table 3, where h_{TX}, h_{RX} are Tx and Rx heights; $d_{TX\text{-}W1}$ is the distance between Tx and Wall 1; $d_{TX\text{-}W2}$ is the distance between Tx and Wall 2; $d_{RX\text{-}W1}$ is the distance between Rx and Wall 1; $d_{RX\text{-}W2}$ is the distance between Rx and Wall 2.

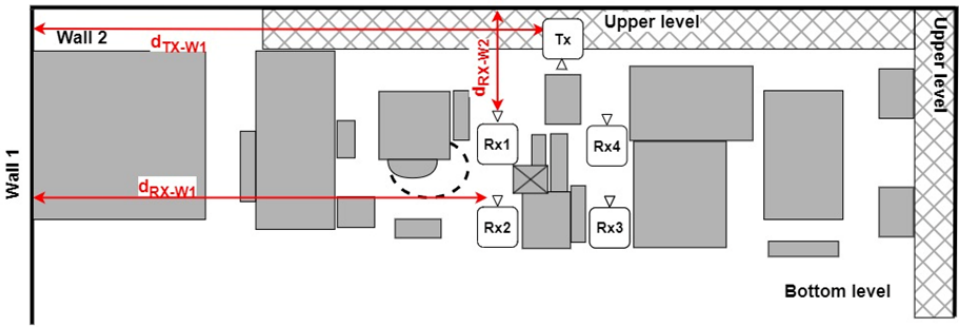

Figure 14 Channel measurements setup.

Table 3 Measurement setup parameters.

Setup number	h_{Tx}, m	h_{Rx}, m	d_{Tx-W1}, m	d_{Tx-W2}, m	d_{Rx-W1}, m	d_{Rx-W2}, m
1	5.25	1.25	21.5	1	19	8
2	5.25	1.25	21.5	1	19	6.5
3	5.25	1.25	21.5	1	24.5	8
4	5.25	1.25	21.5	1	24.5	6.5

Using RT, it is planned to investigate three different Tx locations, one like in the measurement setup, between Rx positions (d_{Tx-W1} = 21.5 m); the second with d_{Tx-W1} = 19 m; and the third with d_{Tx-W1} = 24.5 m. To obtain statistics of model parameters derivation, 72 Rx positions are planned to be investigated (this number may be increased). The room setup for the simulations is shown in Figure 15 and parameters of Rx positions grid are presented in Table 4.

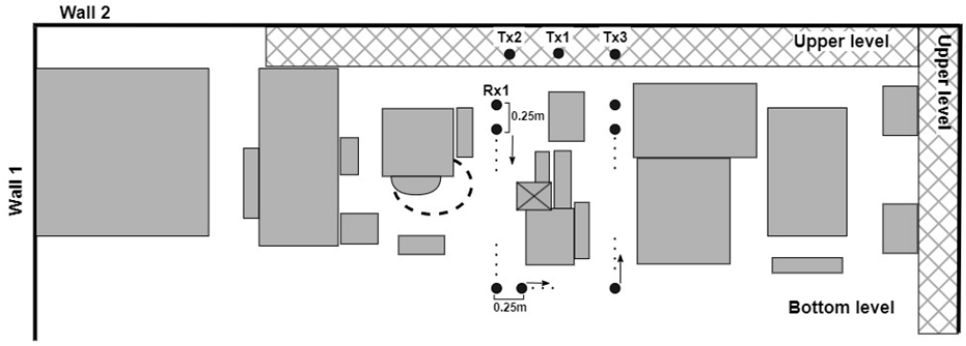

Figure 15 Setup for RT simulation.

Table 4 Simulation setup parameters.

Setup number	h_{Tx}, m	h_{Rx}, m	d_{Tx-W1}, m	d_{Tx-W2}, m	d_{Rx-W1}, m	d_{Rx-W2}, m
1	5.25	1.25	21.5	1	19	4
2	5.25	1.25	21.5	1	19	4.25
3	5.25	1.25	21.5	1	19	4.5

...	...	...	...	...	...	...
26	5.25	1.25	21.5	1	19	10
27	5.25	1.25	21.5	1	19.25	10
28	5.25	1.25	21.5	1	15.5	10
...	...	...	...	...	...	...
42	5.25	1.25	21.5	1	24.25	10
43	5.25	1.25	21.5	1	24.5	10
44	5.25	1.25	21.5	1	24.5	9.5
45	5.25	1.25	21.5	1	24.5	9.25
...	...	...	...	...	...	...
71	5.25	1.25	21.5	1	24.5	4.25
72	5.25	1.25	21.5	1	24.5	4

Channel model realization procedure: The provided channel modeling approach based on spatial path-specific channel function and consists of seven stage that are implemented step by step:

1) Calculation of the LOS amplitude (a_{LOS}) and time of arrival (τ_{LOS});
2) Evaluation of the number of reflection paths and their orders, which are determined based on statistics derived from data generated by RT;
3) Forming ToA vector. That contain τ_{LOS}, and times of arrival (ToA) of all reflection's orders. At first step earliest first order reflection paths, that the same for all Rx positions, reflected from ceiling/walls geometrically calculated. At the second step, higher order reflection first paths approximated with exponential function. Then, all other reflected paths calculated recursively with an interval time that described by statistical distribution;
4) Calculation of the phase-frequency correlation function;
5) Frequency dispersion function. For LOS dispersion coefficient always equal 1. And for reflected path's function can be approximated with a log-linear attenuation over frequency for all reflected rays;
6) Fully polymetric amplitudes obtained with the ToA-amplitude function;
7) AoAs/AoDs evaluation based on the RT statistics.

Model inputs: d, Tx position; f (frequencies vector);
Model outputs: fully polarimetric amplitudes; ToA vector; frequency dispersion; AoAs/AoDs in both elevation and azimuth.

4 Machine Learning approaches for THz channel modeling

This section explores the application of machine learning (ML) in modeling THz channels. It includes methodologies for channel feature extraction, LoS/NLoS classification, multipath component (MPC) clustering, and indoor map generation. Leveraging supervised and unsupervised learning, the section demonstrates how ML can enhance generalizability and accuracy in highly dynamic industrial environments.

THz channel feature extraction

Channel modeling methods developed in literature can be classified into three main categories. Deterministic methods [**Pri2013-1**] rely on ray tracing (RT) approaches, stochastic models focus on a statistical description [**Pri2013-2**] which estimates the mean value of propagation parameters, and semi-empirical models use hybrid techniques [**Cho2018**].

New machine learning (ML)-based techniques can be exploited to improve the description of signal propagation and generalize its behavior to unknown and dynamic scenarios. ML can accomplish different tasks, including line-of-sight (LoS)/non-LoS (NLoS) link classification and channel parameters extraction. The use of ML for LoS/NLoS classification has been partially investigated in the literature with supervised learning (SL) algorithms which rely on a priori known information, called label, and through unsupervised learning (UL) algorithms when a consistent labelled dataset is not available.

This section proposes a methodology to adaptively and dynamically reconstruct the channel propagation model through the extrapolation of the major channel parameters starting by a partial environment knowledge and space-discrete measurements in Industrial IoT (IIoT) scenarios at sub-6GHz, mmWaves, and THz frequencies. The input dataset created with a RT tool is firstly processed by a ML classifier to detect data referred to a LoS or NLoS link. Then, the best fit line for LoS/NLoS data is derived with a ML regression and it is used to estimate the path loss exponent (PLE) and the shadowing standard deviation and therefore to reconstruct a narrowband channel model.

Scenario

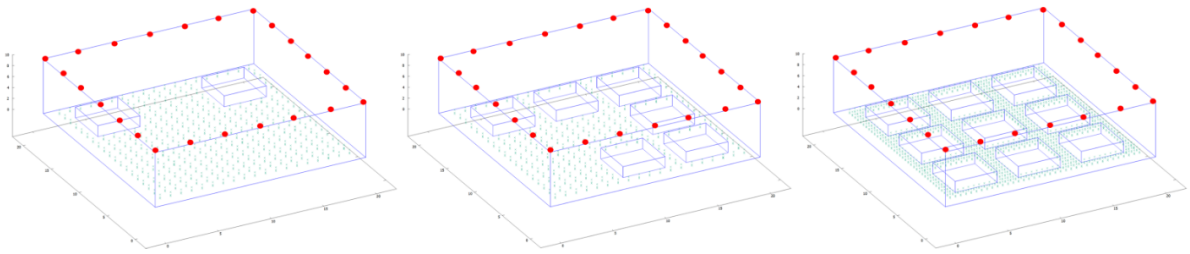

Figure 16 Scenario AGVs with MD = {0.08, 0.24, 0.36} the parallelepiped represents the industrial layout, cubes are the machines, while red and green dots represent the TXs and the RXs, respectively.

The industrial scenario considered is a plant of size $W_x x W_y x W_z$ =20x20x10m^3 in which M machines of size $M_x x M_y x M_z$ =4x4x2m^3 are deployed unevenly with inter-machine distance d_{M2M} =2m and machine-wall distance d_{M2W} =2m. We introduce a parameter to estimate the machines' density, $MD = \frac{\sum_{i=1}^{M} A_{M_i}}{A_W}$, where A_{Mi} is the area occupied by machine $i \in M$ and A_W is the plant's area. Focusing on the downlink, we consider a set of T =24 possible equally spaced BS locations in ($x_{tx,k}$, $y_{tx,k}$, $z_{tx,k}$) with $k \in T$ and a set of R receivers (RXs) placed in ($x_{rx,j}$, $y_{rx,j}$, $z_{rx,j}$) with $j \in R$. Transmitters (TX) and RXs are equipped with omni-directional antennas. RXs of

two categories are considered: mounted over automated guided vehicles (AGVs), Figure *16*, or on a machine, hereafter denoted as machine nodes (MN). AGVs are uniformly distributed in the plant, while MNs are positioned on top and along the edges of the machines, functioning as sensors which collect data from underneath the machine.

Model

This section describes the model implemented for channel parameters estimation and reconstruction which is illustrated in Figure *17*.

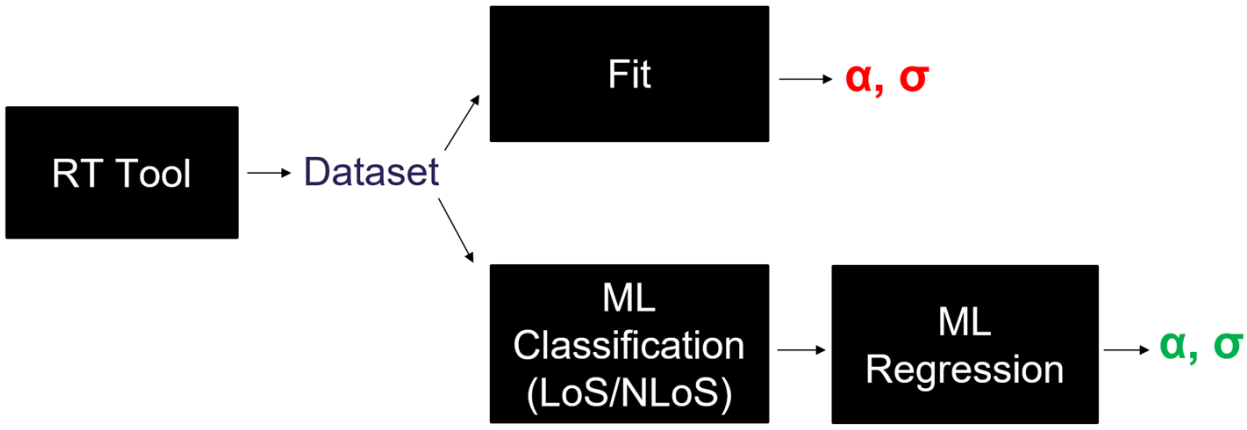

Figure 17 Channel parameter estimation model.

Ray Tracing Tool

The dataset used to train and test our ML algorithms is generated using 3DScat, a ray tracing (RT) tool developed at the University of Bologna in Italy and described with more details in [**Vit2015**] and [**Fus2015**]. 3DScat requires a detailed description of the industrial layout, including information on the location, size, and material characteristics of the plant, machines, and TX and RX nodes. The RT tool classifies with a category which links are in LoS/NLoS condition using a geometrical approach. This is achieved by applying Ray Theory to derive the path loss, PL, and the TX-RX distance d for each link. The resulting dataset is in the format of: (d, PL, category). Electromagnetic parameters of the materials for different working frequencies (sub-6 GHz, mmWaves, and THz range) are described through the relative dielectric constant ε_r and the electrical conductivity σ for building walls, floor, and ceiling composed of concrete (ε_r = 5, σ = 0.01 at f = 3.5 GHz, σ = 0.1 at f = 60 GHz, and σ = 6 at f = 300 GHz) and for machines made of metal (ε_r = 0, σ = 10^9) and considered as perfect electric conductors (PEC). RT simulation involves a series of interactions listed in Table 5. This interaction setting is a suitable balance between precision and computational time. Indeed, the performance seems to saturate when at least three reflections are considered.

3DScat operates in two phases. Firstly, the trajectories of the optical rays between TX and RX are calculated applying an image-RT approach according to the Geometrical Optics Theory and its extensions, such as the Uniform Theory of Diffraction and diffuse scattering models. Later, field propagation evolution along the radii is computed and multipath effects are evaluated on the RX side. To determine the propagating rays, the algorithm recursively sets up a visibility tree, which represents the visibility relationships among devices in the scenario. The visibility tree consists of a succession of layers starting from the root, which corresponds

to the TX, until the n-th layer that contains the objects which can be detected from those belonging to the (n−1)-th layer. The objects are stored in the tree using virtual TXs defined as the symmetric point of the real TX according to the image RT approach. A visibility region is defined for each object, representing the area that can be illuminated by the virtual TX. The presence of a RX within the visibility region indicates the existence of an optical ray connecting TX and RX. Visibility is determined by selecting rays that meet specific requirements, such as having a number of interactions that is less than or equal to the input settings. Once the tracing procedure for the ray is completed, field computation is performed.

The diffuse scattering effect produced by surface irregularities is modelled according to the Effective Roughness model in which the electromagnetic power impinging on a wall is spread according to a scattering coefficient S∈(0, 1), directly related to the amount of power scattered at the expense of specular reflection, and a scattering radiation pattern describing the spatial distribution of the scattered power. In contrast to other interactions, this phenomenon is hardly modelled by a specific interaction point, as it is generated by a multitude of scatterers. For this reason, a ray launching approach is employed. During the visibility assessment process several rays are launched from the TX with a preset angular discretisation and the scattering tiles are identified as the intersection point between the launched rays and the objects. Each tile is regarded as a virtual TX, acting as a secondary source with a fixed area which depends on the source's distance and the angular discretisation. Finally, the interaction coefficients and the rays arriving at the receiver are identified.

Table 5 Interaction settings.

Kind of Interaction	Number
N MAX INTERACTIONS	5
N MAX REFL	3
N MAX DIFF	1
N MAX REFL WITH SCAT	1
N MAX DIFF WITH SCAT	0
N MAX REFL AND DIFF	4

ML Classification

LoS/NLoS link classification is performed using the random forest (RF) algorithm. RF is a linear and rule-based SL classifier which clusters items with same feature values into groups using a collection of rules [**Sar2018**]. It consists in a combination of tree-structured predictors, where each tree depends on the values of a random vector, sampled independently, and with same distribution for all the trees in the forest. Each tree casts a unit vote for the most popular class given the input [**Bre2001**]. The classifier introduces randomness by exploiting a random selection of features at each node, resulting in decision trees with decoupled prediction errors. Averaging these predictions, it can cancel out some errors that generally depend on the strength of the individual trees and the correlation between them. RF is preferred over other ML algorithms because it reduces the variance by combining diverse trees and obtains a higher level of accuracy.

The classification problem is designed as a binary classifier which takes the dataset generated by RT in the format of (d, PL, category) as input and predicts the class of LoS/NLoS as outcome. The labels of LoS/NLoS are referred to as positive P or negative N, respectively, where the input dataset has size N_{test} = N +P. The

classifier assigns a label to each element of the dataset: true positive (TP) and true negative (TN) refer to correctly detected labels, while false positive (FP) and false negative (FN) account for incorrect decisions. These quantities are generally displayed through a 2x2 confusion matrix illustrated in Figure 8.

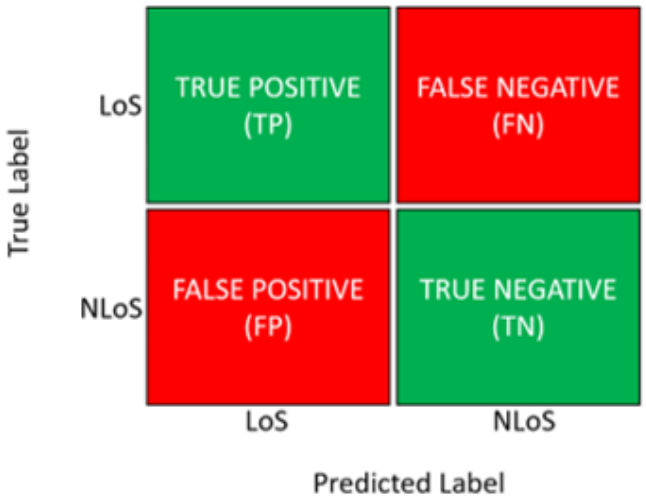

Figure 18 Binary classifier confusion matrix.

The accuracy, or success rate, is used as the metric to evaluate LoS/NLoS classification capabilities. It is defined as the ratio between the number of correct classifications and the total ones:

$$accuracy = \frac{TP+TN}{TP+FP+TN+FN}$$

ML Regression

ML regression is employed to determine the best fit line for points classified in LoS/NLoS condition. Nonlinear regression is a SL technique which models the observed data with a function *f*, that is a nonlinear combination of the estimated parameter vector $\theta = [\theta_0, \theta_1, ..., \theta_n]^T$ and of the independent input variable *x*. The nonlinear regression exploited in this work is the polynomial regression, expressed as:

$$y = f(x) = \theta_0 + \theta_1 x + \theta_2 x^2 + ... + \theta_n x^n = \theta_0 + \sum_{j=1}^{n} \theta_j x^j$$

The goal is to determine the vector θ and the order *n* of the regression which best fit the cloud of points in LoS/ NLoS, respectively.

Parameters Extraction

After obtaining the best fit lines for LoS/NLoS links, mathematical methods are exploited to derive large-scale parameters of the channel, such as PLE and shadowing standard deviation. Assuming far-field conditions (TX-RX distance much greater than wavelength), the narrowband channel model is built as follows. Path loss PL is described as:

$$PL_s(d) = c + 10\alpha_s \log_{10}(d) + \xi_s,$$

where s stands for the binary value of LoS/NLoS condition, d represents the 3D distance between TX and RX, $c = 20\log10(4\pi/\lambda)$ is the path loss at a reference distance $d_{ref} = 1$ m, α_s is the PLE, and ξ_s represents the additional attenuation due to shadowing fluctuations. Shadowing is a phenomenon caused by the presence of obstacles obstructing the direct link between TX and RX, resulting in slow fluctuations. It is a large scale effect modelled through a zero mean Gaussian distribution $\xi_s \sim N(0, \sigma_s^2)$ with standard deviation:

$$\sigma_s = \sqrt{\frac{\sum_{i=1}^{N}(x_i-\mu)^2}{N}}$$

where N is the total number of values, x_i represents the i-th value, and μ is the expected value. This channel model is also applicable at high frequencies because it has been demonstrated that THz frequency effects, such as molecular absorption, have a limited impact on the channel in this moderate sized scenario.

Results

This section investigates the accuracy of LoS/NloS classification and the reconstruction of large-scale parameters in the developed model. The evaluation includes the variation of channel behaviour in terms of PLE and shadowing standard deviation, for different heights of the TX, z_{tx}, for various machine densities MD = {0.08, 0.24, 0.36} (corresponding to M ∈ {2, 6, 9} machines in the scenario, respectively), at different frequencies, f, and for the two use cases with AGVs and MNs. The BS is positioned at a height $z_{tx} \in [2, 10]$m from the ground. AGVs have a height of $z_{rx,AGV}$ = {0.3, 0.5, 1}m, while $z_{rx,MN} = Mz + \delta$, with δ = 0.01m for MNs located on top of the machines, and $z_{rx,MN}$ = {0.3, 0.5, 1}m for MNs located along the edges of the machines. The transmitted power is P_t = 0 dBm, TX and RX antenna gains are G_t, G_r = 0 dB, and the working frequencies are f = 3.5, 60, 300 GHz.

ML Dataset

ML algorithms require a significant amount of data that includes various representative features for the investigated layout. A feature is considered poor if does not allow to clearly separate data between different classes and satisfying otherwise. The proposed model uses an input dataset comprising over 14,000 data points, with 60% allocated to the training phase and 40% for performance validation. Figure 9 illustrates the correlation matrix which describes the correlation between the predicted labels and the dataset features, i.e., 0.45 and 0.57 for distance and path loss, respectively. In fact, LoS/NLoS condition is closely related to the layout geometry. Additionally, LoS probability is generally a decreasing function of distance and path loss. Correlation matrix results demonstrate a high correlation between the selected features and the classified category, proving the effectiveness of the selected features for the classification task. Also, the model is advantageous as it allows to classify data using a limited and easily accessible dataset.

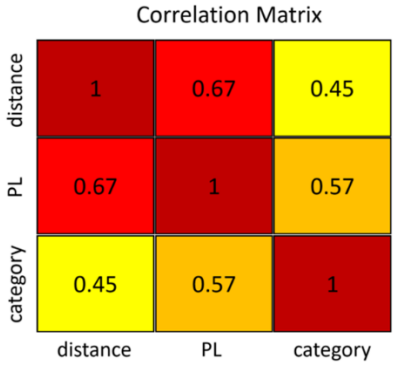

Figure 19 Correlation matrix describing the correlation between predicted labels and dataset features.

LoS/NLoS Classification

Various SL algorithms are exploited to achieve optimal LoS/NLoS link classification. These algorithms include AdaBoost (A), decision tree (DT), gradient boosting decision tree (GBDT), K-nearest neighbor (K-NN), neural network-multi layer perceptron (NN-MLP), and random forest (RF) classifiers. Their mean accuracy and standard deviation for the considered scenarios are listed in Table 2.

Table 6 SL Algorithms accuracy and standard deviation.

Algorithm	Mean Accuracy	Standard Deviation
A	89.33%	7.4
DT	97.01%	3.78
GBDT	90.98%	6.41
K-NN	93.39%	4.47
NN-MLP	89.01%	7.62
RF	97.58%	3.11

From results it is evident that RF classifier, which is the algorithm exploited in this work, achieves the highest mean accuracy of 97.58% and minimum standard deviation of 3.11 across all scenarios. Moreover, DT and RF algorithms have similar accuracy, as RF is a DT-derived algorithm that combines tree-structured predictors.

To investigate the classification capabilities of the algorithms, their accuracy behaviour at the variation of the TX height is studied and listed in Figure 10. It was discovered that accuracy decreases and reaches a minimum value when the TX height is $z_{tx} \in [3, 5]$ m. However, as the TX height increases the accuracy improves. This behaviour is closely related to the path loss experienced by nodes at various TX heights. When the TX is at a height of z_{tx} = 2m most of the links are in NLoS condition. However, increasing the TX height to $z_{tx} \in [3, 5]$m results in a varied channel condition for LoS/NLoS nodes, with an increased number of nodes in LoS. Further increasing the TX height to $z_{tx} \in [8, 10]$ results in the majority of nodes becoming in LoS condition.

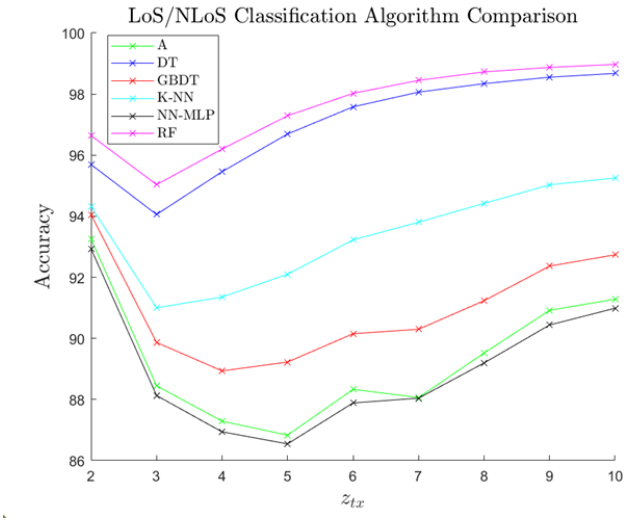

Figure 20 SL Algorithm accuracy with respect to the variation of the transmitter height.

Also, accuracy values obtained with RF algorithm for various layouts are investigated. The classification capability of the ML algorithm depends on the geometry of the industrial layout and, specifically, on the TX height, z_{tx}, and machines density, MD, which corresponds to a different number of obstructing machines. Indeed, these elements affect the PL in LoS/ NLoS and consequently impact the classification capabilities. Figure 11 shows the variation of RF accuracy with respect to the TX height, z_{tx}, for AGVs and MNs at f = 3.5, 60, 300 GHz. Results suggest that frequency plays a crucial role in determining accuracy as they are directly proportional. Lower frequencies result in lower precision, while higher frequencies lead to a higher precision. Indeed, the frequency has an important impact on final PL: at higher frequency LoS and NLoS components have extremely different PL which leads to a simpler classification, while by decreasing the working frequency the difference is reduced.

Finally, it is evaluated the accuracy variation with respect to different TX heights for AGVs and MNs. From results emerges that at z_{tx} = 3m there is a minimum of accuracy due to LoS, NLoS, and obstructed LoS (OLoS) nodes. Indeed, OLoS nodes refer to those in NLoS condition but located closely behind the corner, so that LoS and OLoS nodes experience a similar attenuation and it is harder to classify them. Increasing the TX height further improves accuracy. Also, the accuracy achieved with MNs is higher than that of AGVs, due to the specificity of the scenario considered

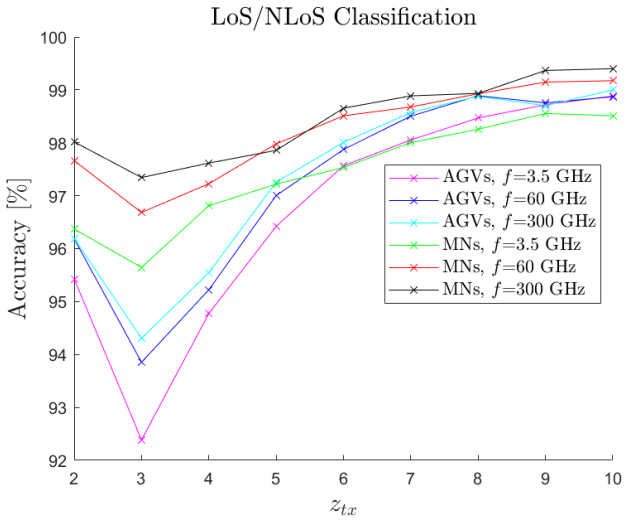

Figure 21 LoS/NLoS classification accuracy with respect to z_{tx} variation for MNs and AGVs at f = 3.5, 60, and 300 GHz.

Path Loss exponent

Regarding the channel behaviour, Figure 12 shows the variation of the PLE, α_s, in LoS/ NLoS conditions with respect to the TX height, z_{tx}, for MD = 0.08, MD = 0.24, and MD = 0.36 at f = 3.5, 60, and 300 GHz respectively. The results obtained demonstrate an extraordinary degree of accuracy. Indeed, Figure 12 illustrates a comparison between the channel parameters achieved by a simple fit, assuming the link LoS/NLoS condition known, and those obtained by applying ML for classification, regression, and successive calculation of large scale parameters with, and without a limitation on the regression order *n*. Results indicate that by increasing the carrier frequency there is an increase of the PLE in NLoS condition, while it remains nearly constant at around α_{LoS} = 2 in LoS. In addition, the attenuation experienced by MNs in NLoS is higher than that experienced by AGVs, while it is invariant in LoS condition.

For what concerns MD = 0.08 results, the optimal placement for the BS in the AGVs scenario is at z_{tx} = 3m, indeed, by changing the TX height the PLE tends to increase. By decreasing the TX height to z_{tx} = 2m it is at the same level as machines, resulting in increased attenuation due to diffraction effects. Instead, by improving the height of the TX, PLE increases due to the specific layout. To address this issue, nodes should be classified into three classes: LoS, NLoS, and OLoS. The PL for OLoS nodes is not extremely high and if the TX height is increased they become in LoS and have an impact on the PLE in LoS. On the other hand, the PLE in NLoS comprises only nodes in heavy NLoS condition, causing an increase in PLE. For MNs, increasing the TX height tends to decrease PLE in NLoS, as nodes previously in NLoS become in LoS. For this reason, an optimal BS placement can be z_{tx} = 10m.

For what concerns MD = 0.24 results, MNs and AGVs scenarios exhibit similar behaviour. Both cases are endowed with an almost constant PLE in NLoS if the TX is located at a height $z_{tx} \in [3, 10]$m. This suggests that each site has the potential to serve as an optimal BS placement for enhancing network performance. While reducing the height of the TX to z_{tx} = 2m increases PLE due to diffraction effects.

In case of MD = 0.36, AGVs' scenario shows higher PLE for a low BS placement and lower PLE for a higher BS employment. The presence of multipath improves the received power in this setting. For MNs, the PLE in NLoS tends to decrease initially if the TX height is $z_{tx} \in [2, 5]$m, then it gradually increases. This behaviour is intensified by increasing the carrier frequency. Thus, a well-placed BS could have z_{tx} = 5m.

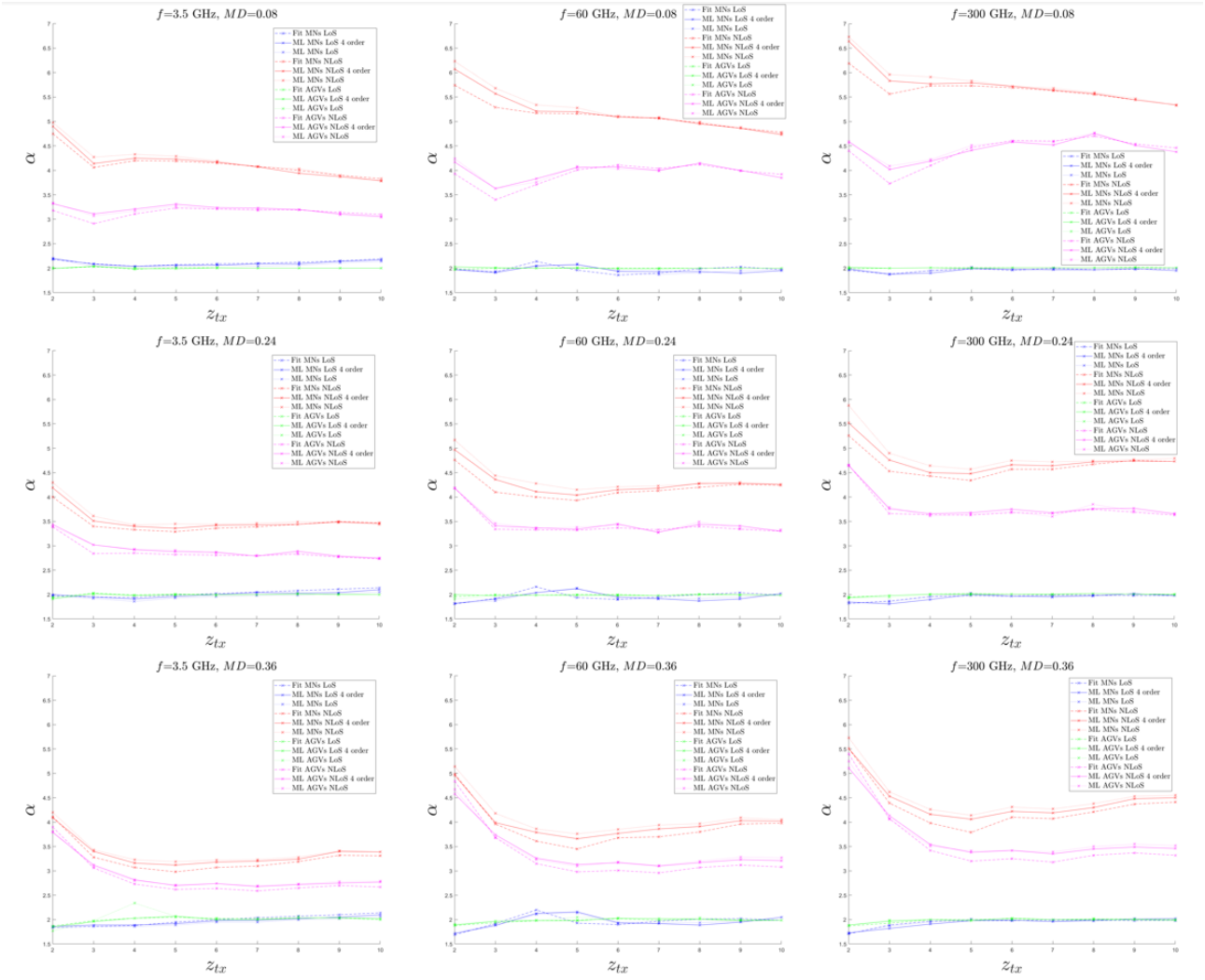

Figure 22 PLE variation with respect to ztx for MNs and AGVs at f = 3.5, 60, 300 GHz and MD = {0.08, 0.24, 0.36}.

Shadowing Standard Deviation

Table 3 lists the shadowing standard deviation, σ_s, in LoS/NLoS for AGVs and MNs for different values of MD and carrier frequency f (expressed in GHz). The results indicate that the shadowing standard deviation in NLoS tends to rise with the carrier frequency, while it decreases in LoS condition. Also, MNs experience a higher shadowing standard deviation than AGVs in both LoS/NLoS conditions. Figure 13 depicts the variation of the shadowing standard deviation σ_s with the TX height z_{tx} at f = 3.5 GHz and MD = 0.24. Results suggest that the standard deviation in NLoS decreases with the TX height for AGVs and MNs scenarios. The LoS shadowing standard deviation is a decreasing function of the TX height for AGVs and has an increasing trend for MNs. Indeed, improving the TX height can change the LoS condition for some nodes that previously were in NLoS, resulting in a significant difference in signal propagation.

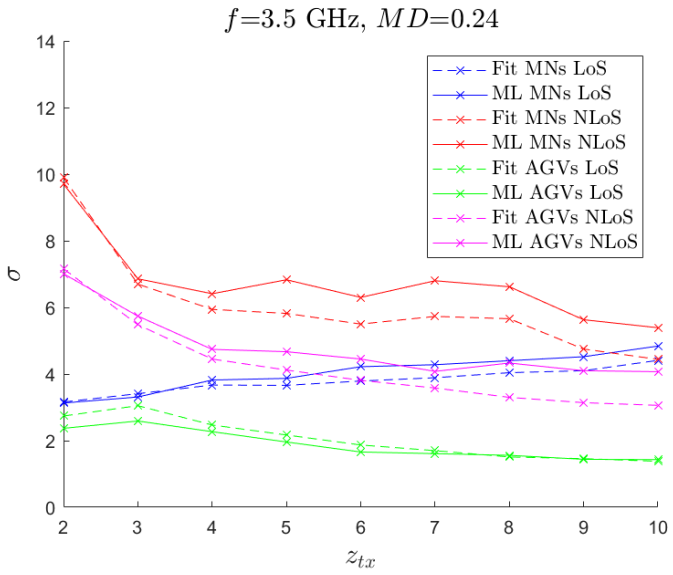

Figure 23 Shadowing standard deviation with respect to ztx variation for MNs and AGVs.

Table 7 Shadowing standard deviation values.

Values		AGVs		MNs	
f	MD	σ_{LoS}	σ_{NLoS}	σ_{LoS}	σ_{NLoS}
3.5	0.08	[0.9, 2.1]	[1.5, 5.1]	[3.2, 5.4]	[4.5, 8.4]
	0.24	[1.4, 2.6]	[4.1, 7.0]	[3.1, 4.8]	[5.4, 9.7]
	0.36	[1.9, 2.2]	[4.8, 6.5]	[2.6, 4.8]	[5.3, 7.5]
60	0.08	[0.9, 2.1]	[1.1, 6.8]	[2.6, 4.4]	[4.8, 9.0]
	0.24	[1.1, 2.7]	[6.6, 9.2]	[2.3, 3.9]	[7.3, 11.5]
	0.36	[1.9, 2.6]	[7.5, 9.2]	[2.1, 3.5]	[6.9, 8.9]
300	0.08	[0.9, 2.2]	[1.9, 8.5]	[2.3, 3.6]	[4.6, 8.6]
	0.24	[1.2, 2.6]	[8.6, 11.1]	[2.3, 3.4]	[7.5, 11.7]
	0.36	[1.9, 2.7]	[8.4, 10.9]	[1.9, 3.5]	[7.4, 9.9]

Remarks

In this section it was implemented an innovative ML-based channel model which can be dynamically applied in a variety of IIoT scenarios with sensing capabilities at sub-6 GHz, mmWaves, and THz bands. The model exploited ML to classify data in LoS/NLoS using a dataset generated with RT simulation. Subsequently, a ML regression is applied to determine the best fit line and derive the main channel parameters, including the PLE and the standard deviation of shadowing. The results proved that the developed model is highly accurate, achieving an accuracy of over 99.1%, and illustrated PLE and shadowing variation in LoS/NLoS for MNs and AGVs in different industrial layouts and at various frequency ranges. The final goal was to investigate the impact of the industrial layout on the variation of channel parameters. Moreover, the parameters extracted by the extensive RT simulations can be utilised for the purpose of evaluating network performance in IIoT scenarios.

Subsections below list several channel models that can be used within SNS TIMES, depending on the target application of the model, the simulation scope (e.g., link vs system level simulations), the type of communication system evaluated (e.g., single vs multi-antenna simulations), etc.

Identification and clustering of multipath components

Wireless communication is a trending topic in transforming and modernizing industrial applications, including automation, manufacturing, monitoring, and maintenance. With its ease of deployment, together with mobility and flexibility, wireless communication is preferred over conventional wired systems to be deployed in complex and dynamic environments like manufacturing floors with machinery. Nevertheless, industrial settings also pose challenges to wireless communication due to the presence of industrial objects, often with metallic surfaces. The resulting complex propagation phenomena, such as reflection, scattering, and diffraction, can severely affect the quality and reliability of signals. As a result, analyzing and understanding the propagation environment in industrial settings is essential for advancing wireless communication in industrial scenarios.

While the conventional frequency bands (sub-6 GHz) are effective for numerous traditional applications, challenges exist for deploying them in industrial applications. Limited capacity and interference, considering the multitude of devices to be equipped with communication capability, can constrain the performance of wireless communication in terms of throughput and latency. To overcome these challenges, there is a pressing need to explore and exploit new frequency bands, particularly in the terahertz (THz) and millimeter-wave (mmWave) ranges. With a wider spectrum, THz and mmWave communication could alleviate congestion in conventional bands and could also provide new propagation characteristics to be harnessed. Moreover, the short communication range of mmWave and THz bands is less serious a problem because the typical communication in industrial settings occurs over short distances.

Regardless of frequency, the complex propagation effects in industrial settings yield a multipath effect, where signals arriving at the receiver due to different points of reflection, etc. can lead to both constructive and destructive interference. Therefore, modeling wireless channels that incorporate multipath components (MPCs) become essential for optimizing wireless communication systems in industrial applications. To this end, wireless channel models are often built upon modeling electromagnetic propagation with a finite number of MPCs, with each of the components characterized by its unique amplitude, delay, and angles of arrival and departure. In practice, MPCs with similar characteristics are grouped into clusters, so as to facilitate processing received signals in batches and reduce channel estimation complexity. Moreover, distinguishing clusters of MPCs is beneficial for systems like rake receivers and multiple-input multiple-output (MIMO) to select useful and dominant MPCs with less interferences. Clusters with distinct spatial directions can be exploited with beam forming to enhance channel capacity.

In terms of the identification of MPCs, classic approaches include using parameter estimators on measurements, simulating the propagation via ray tracing, and manual inspection on the signals. MPCs are often represented as the peak points in the received signal with angular information. For measurements with noise, parameter estimators for reconstructing MPC information could yield unreliable results even with high complexity in implementation and computation. The availability of validation with a ray tracing platform is also not guaranteed, which is dependent on the amount of information known about the propagating environment. In the case of an unknown wireless environment, or when the number of MPCs reaches a certain multitude, identifying peaks and performing manual clustering of MPCs become time-consuming and erroneous.

In light of the challenges mentioned, there is a need for efficient processing of measurements to extract the information of MPC clusters. In the following subsections, the task was approached from a data processing and manipulation perspective, without fitting parameter models. Two well-known clustering algorithms are investigated, as well as the effectiveness of different distance metrics in distinguishing MPCs. A complete workflow for processing raw measurements, applying clustering algorithms, and extracting cluster information is proposed. In the end, the clustering results across different frequency bands are analysed and compared.

Measurement Setup

The measurements are collected in an indoor factory setting with 3 transmitter locations and 12 receiver locations selected to study the propagating condition of line-of-sight (LOS) and non-line-of-sight (NLOS). 20 measurements on 20 pairs of transmitter–receiver settings are conducted. The directions of transmitting and receiving are fixed on the horizontal plane and rotate with a 15° separation, aiming to capture the full range of propagation scenarios, including LOS and NLOS cases. The measurements cover the THz frequency (300 GHz), mmWave frequency (74.25 GHz), as well as sub-6 GHz frequency (6.75 GHz), providing a comprehensive understanding of the channel characteristics at different bands. For each frequency band, the measurement is conducted with two pairs of antenna polarization directions (horizontal–horizontal and vertical–vertical). Detailed measurement configurations are documented in Table *8*.

For each transmitter and receiver location, we obtained measurement data in the following format: (41)

$$H \subset R_{\geq 0}^{T \times P \times I \times J \times M \times N}$$

Details of the variables related to the dimension of the data are listed in Table *9*. In the following experiment and analysis, the elevation scanning angle is 0° only, therefore $\mathrm{J} = 1$ and $\mathrm{N} = 1$.

Table 8 Measurement setup.

Parameter	Sub-6 GHz	mmWave	THz
Frequency (GHz)	6.75	74.25	305.27
Calibrated bandwidth (GHz)	5		
Azi. scanning angles ($\alpha_{TA,RA}$)	$\{-180^\circ, -165^\circ, \ldots, 165^\circ\}$		
Ele. scanning angles ($\alpha_{TE,RE}$)	0°		

Table 9 Variables, parameters, and acronyms used in algorithms and experiments.

T	Measured time steps
P	Number of polarization pairs of transmitter and receiver
I, J M, N	Number of the scanning angles of transmitter azimuth/elevation and receiver azimuth/elevation
H	Measurement data
α_*	$* \in \{TA, TE, RA, RE\}$, the corresponding angles of signals in ray-tracing experiments

Clustering Algorithm

To perform direct identification and clustering of the measurement signal, the signal matrix needs to be converted into data points that fit the corresponding clustering algorithm. With the clustered output, another procedure of post-processing the results is performed to extract characteristic information of the MPC clusters. This section is divided into three parts that describe the three procedures.

Preprocessing: The preprocessing of signal matrix in is shown in Algorithm *1*, separated in terms of two different metrics for evaluating the distance between signals. For classic Euclidean distance, the power of the received signal at the specific time step, as well as the power difference between the current time step and the previous/following steps are included in the feature. The angular difference between signals is represented by the sinusoidal values (cosine and sine) of the transmitter and receiver angles, which aims to differentiate symmetrical angles and keeps the physical continuity of angles at numerical jumps (e.g. $359°$ to $0°$). The complete process of getting the sinusoidal features is described in Algorithm *2*. The number of sinusoidal features is reduced by using only cosine/sine values when all of the angular values are in the monotonic range of cosine/sine functions. For power distance [**Czi2006**], the angle information (departure/arrival) of a signal is fed to compute the multipath distance (MCD), as later shown in Equation (43).

The conditions to exclude points with $\mathrm{p}_*, \forall * \in \{f, b, t\}$ in Algorithm *1* are to filter out points in the measurement where there is no signal received, thus to reduce the size of data later fed into the clustering algorithm and speed up the process.

Algorithm 1 Preprocessing on measurement matrix.

Input: H, $\mathtt{pid}$, $\mathbf{TA}, \mathbf{TE}, \mathbf{RA}, \mathbf{RE}$ Measurement data of the required format, selected polarization index, lists of transmitter's azimuth and elevation angles and receiver's azimuth and elevation angles
Output: l

Preprocessing before using Euclidean distance

$l \leftarrow \varnothing$
for $\mathtt{i}, \mathtt{j}, \mathtt{m}, \mathtt{n} \in [I] \times [J] \times [M] \times [N]$ **do**
  $h \leftarrow H[:][\mathtt{pid}][\mathtt{i}][\mathtt{j}][\mathtt{m}][\mathtt{n}]$
  for $t \in K$ **do**
    $p_t \leftarrow h[t]$, $p_f \leftarrow p_t - h[t-1]$, $p_b \leftarrow p_t - h[t+1]$
    $\boldsymbol{\theta} \leftarrow \mathtt{GetAngles}(\mathbf{TA}, \mathbf{TE}, \mathbf{RA}, \mathbf{RE}, i, j, m, n)$
    if not ($p_f = 0$ and $p_b = 0$ and $p_t = 0$) **then**
      $l \leftarrow l \cup \{(t, \boldsymbol{\theta}, p_f, p_b, p_t)\}$
    end if
  end for
end for

Preprocessing before using power distance

$l \leftarrow \varnothing$
for $\mathtt{i}, \mathtt{j}, \mathtt{m}, \mathtt{n} \in [I] \times [J] \times [M] \times [N]$ **do**
  $h \leftarrow H[:][\mathtt{pid}][\mathtt{i}][\mathtt{j}][\mathtt{m}][\mathtt{n}]$
  for $t \in K$ **do**
    $p_t \leftarrow h[t]$, $p_f \leftarrow p_t - h[t-1]$, $p_b \leftarrow p_t - h[t+1]$
    if not ($p_f = 0$ and $p_b = 0$ and $p_t = 0$) **then**
      $l \leftarrow l \cup \{(p_t, t, \mathbf{TA}[\mathtt{i}], \mathbf{TE}[\mathtt{j}], \mathbf{RA}[\mathtt{m}], \mathbf{RE}[\mathtt{n}])\}$
    end if
  end for
end for

Clustering: Two clustering algorithms, K-means and DBSCAN, are implemented for comparison. The terminology of related terms is detailed in Table *10*.

Algorithm 2 GetAngles().

Input: $\mathbf{TA}, \mathbf{TE}, \mathbf{RA}, \mathbf{RE}, i, j, m, n$ lists of transmitter's azimuth and elevation angles and receiver's azimuth and elevation angles, index of the corresponding sam-pled angle

Initialization
for $\mathbf{L} \in \{\mathbf{TA}, \mathbf{TE}, \mathbf{RA}, \mathbf{RE}\}$ **do**
  Shift all values in $\mathbf{L}$ to be in $[0, 2\pi]$
  if $x \in [0, \pi], \forall x \in \mathbf{L}$ or $x \in [\pi, 2\pi], \forall x \in \mathbf{L}$ **then**
    `cos_only` ← `True`
  end if
  Shift all values in $\mathbf{L}$ to be in $[-\pi/2, 3\pi/2]$
  if $x \in [-\pi/2, \pi/2], \forall x \in \mathbf{L}$ or $x \in [\pi/2, 3\pi/2], \forall x \in \mathbf{L}$ **then**
    `sin_only` ← `True`
  end if
end for

Per-point processing
for $\mathbf{L} \in \{\mathbf{TA}, \mathbf{TE}, \mathbf{RA}, \mathbf{RE}\}$ **do**
  $\boldsymbol{\theta} \leftarrow \varnothing$
  $k \leftarrow$ the corresponding index for the list
  if `cos_only` **then**
    $\boldsymbol{\theta} \leftarrow \boldsymbol{\theta} \cup \{\cos \mathbf{L}[k]\}$
  else if `sin_only` **then**
    $\boldsymbol{\theta} \leftarrow \boldsymbol{\theta} \cup \{\sin \mathbf{L}[k]\}$
  else
    $\boldsymbol{\theta} \leftarrow \boldsymbol{\theta} \cup \{\cos \mathbf{L}[k], \sin \mathbf{L}[k]\}$
  end if
end for
return $\boldsymbol{\theta}$

Table 10 Notations in equations.

$d(m,n)$	Distance between point *m* and *n*
d_{euc}	Euclidean distance
d_{pow}	Originally defined power distance
d'_{pow}	Newly defined power distance
P_m	Power of point *m*
MCD_{mn}	MCD between *m* and *n*
MCD_{AoA}	Angle of arrival component of MCD
MCD_{AoD}	Angle of departure component of MCD
MCD_{τ}	Time difference component of MCD

In the original versions of the two algorithms, n-dimensional points are input, and the Euclidean distance based on all dimensions is used as the metric to determine the proximity of two points:

$$d_{euc}(m,n) = \left(\sum_{i=1}^{n}(m_i - n_i)^2\right)^{1/2} \quad (42)$$

Power distance was introduced to evaluated the proximity of an MPC components to its cluster center:

$d_{pow}(m,n) = P_m \cdot MCD_{mn}$, where n is the cluster centroid in the K-means algorithm and m is the input points to be clustered.

$$MCD_{mn} = \sqrt{\left\|MCD_{AoA,mn}\right\|^2 + \left\|MCD_{AoD,mn}\right\|^2 + \left\|MCD_{\tau,mn}\right\|^2} \quad (43)$$

For components in computing MCD_{mn}:

$$\left\|MCD_{AoA,mn}\right\| = \frac{1}{2}\left\| \begin{matrix} \sin\theta_m \cos\phi_m & \sin\theta_n \cos\phi_n \\ \sin\theta_m \sin\phi_m & -\sin\theta_n \sin\phi_n \\ \cos\theta_m & \cos\theta_n \end{matrix} \right\| \quad (44)$$

$$MCD_{\tau,mn} = \zeta \cdot \frac{|\tau_m - \tau_n|}{\Delta\tau_{\max}} \cdot \frac{\tau_{\text{std}}}{\Delta\tau_{\max}} \quad (45)$$

DBSCAN does not define a centroid for each cluster but finds neighbours for each input point. Therefore, when calculating the distance, the power of both signal points should be considered, rather than just one as in d_{pow} which results in $d(m,n) \neq d(n,m)$. To this end, a variation is derived as $d'_{pow}(m,n) = (|P_m - P_n| + P_{base}) \cdot MCD_{mn}$ for computing the power distance when applying DBSCAN algorithm. The computation of absolute difference ensures symmetry when swapping the input sequence of the two points. The addition of P_{base} serves as the base scalar when two points have similar similar power levels but differ in angles.

For algorithms using both distance metrics, it is necessary to adapt clustering parameters and further scale the inputs before feeding data points. The process flow is shown in Algorithm 3 and the scaling factor for each of the features is shown in Table 11. Lines 5 – 8 in Algorithm 3 shift the power values of all points when using decibel values to be greater than zero, thus guaranteeing that computed power distance is greater than zero.

Algorithm 3 Clustering Process

1: get l from measurement preprocessing
2: **if** Euclidean distance **then**
3: $l \leftarrow \texttt{Scaling}(l)$
4: **else if** Power distance **then**
5: **if** Use decibel values for power **then**
6: $P_{dB} \leftarrow \{10 \cdot \log v[0], \forall v \in l\}$
7: $p_{\min} \leftarrow \min P_{dB}$
8: $v[0] \leftarrow \log v[0] - p_{\min}, \forall v \in l$
9: **end if**
10: choose time scaling factor ζ
11: **end if**
12: choose centroid model (k-means) or density model (DBSCAN)
13: perform clustering, get $c_x \forall x \in l$

Table 11 Scaling factors in clustering with Euclidean distance.

Name	Value
p_t, p_f, p_b in dB	0.2
t	$7.788 \cdot 10^8$
$\boldsymbol{\theta}$	8.0

Post-processing: We propose Algorithm 4 to process the clustered points or the original matrix of the raw signal. For simplicity, the dimension of the matrix processed is $\mathrm{T} \times \mathrm{I} \times \mathrm{M}$, which suits measurement data with only one measuring angle of transmitting and receiving elevations. The algorithm can be further extended to

be compatible with data of higher dimensions where the elevation angles are also included. Algorithm 4 tracks the peak (with power greater than its neighboring angles) of the arriving signals in each time frame and consistently logs the location of peaks, with considerations that the peak might shift in angular domains. It is worth noting that Algorithm 4 can also be used as a preprocessing step to extract the peaks in the raw signals. The advantages of using Algorithm 4 on clustered results lie in the shorter processing time, where it is easier to find local maxima in a frame (in Line 6) when processing a sparse matrix yielded by clustered data. The information of peaks identified by Algorithm 4 in each cluster, e.g. angular values and duration, is then valuable for further microwave applications.

Algorithm 4 Track Local Maxima Over Time

1: **Input:** data points $(p_t, t, \texttt{TxAz}_t, \texttt{RxAz}_t)$ in the same cluster
2: Get `Frames` $(T \times I \times M)$ from signals of the same cluster
3: $\mathbf{P}_{\text{found}} \leftarrow \varnothing$, $\mathbf{P}_{\text{live}} \leftarrow \varnothing$
4: **for** `Frm` $\in$ `Frames` **do**
5: get time stamp `t` and local `maxima` in `Frm`
6: $\mathbf{P}_{\text{new}} \leftarrow \varnothing$
7: **for** each detected peak $(\texttt{i}, \texttt{j})$ in `maxima` **do**
8: `matched` $\leftarrow$ `False`
9: **for** $p \in \mathbf{P}_{\text{live}}$ **do**
10: **if** $(\texttt{i}, \texttt{j})$ is within 1-pixel shift of p **then**
11: Update p with new $(\texttt{i}, \texttt{j})$
12: Add updated p to $\mathbf{P}_{\text{new}}$
13: `matched` $\leftarrow$ `True`
14: **break**
15: **if** not `matched` **then**
16: Create p_{new} with $p.\texttt{t}_{\text{start}} = \texttt{t}$ and information $(\texttt{i}, \texttt{j})$
17: $\mathbf{P}_{\text{new}} \leftarrow \mathbf{P}_{\text{new}} \cup p_{\text{new}}$, $\mathbf{P}_{\text{live}} \leftarrow \mathbf{P}_{\text{live}} \cup p_{\text{new}}$
18: **for** $p \in \mathbf{P}_{\text{live}}$ **do**
19: **if** p is not in $\mathbf{P}_{\text{new}}$ **then**
20: $p.\texttt{t}_{\text{end}} \leftarrow \texttt{t}$, $\mathbf{P}_{\text{found}} \leftarrow \mathbf{P}_{\text{found}} \cup p$
21: $\mathbf{P}_{\text{new}} \leftarrow \mathbf{P}_{\text{live}}$
22: Get the ending time step of signal cluster: $\texttt{t}_{\text{end}}$
23: **for** $p \in \mathbf{P}_{\text{live}}$ **do**
24: $p.\texttt{t}_{\text{end}} \leftarrow \texttt{t}_{\text{end}}$, $\mathbf{P}_{\text{found}} \leftarrow \mathbf{P}_{\text{found}} \cup p$
25: **Return** $\mathbf{P}_{\text{found}}$

Experiments

The scaling factors for each feature used to compute Euclidean distance and power distance are listed in Table 11. For the algorithm of K(Power)-Means, the number of clusters k is the hyper-parameter. For DBSCAN, the neighbor-threshold distance e is the parameter to determine if a cluster should expand to include another point. The searching range of k and e are listed in Table 12.

Table 12 Searching range of hyper-parameters in clustering.

DBSCAN	e for Euclidean distance	$\{2.0, 2.5, 3.0\}$
	e for power distance	$\{0.001, 0.003, 0.006\}$
	P_{base}	$\{0.005, 0.01, 0.02\}$
	ζ	$\{0.1, 0.2, 0.4, 0.8\}$
K(Power)-Means	k	$\{3, 4, \dots, 10\}$

For any time step in the measurements with signals received from any angle, heatmaps are plotted to evaluate if the signal belongs to a certain cluster. For the transmitter–receiver location pairs where there is always only one MPC arriving at a time, as shown in Figure 24(a), or more than one MPCs close to each other as shown in Figure 24(b), the time range of the corresponding MPC cluster is manually identified, with MPCs then clustered based on their time-wise and angular proximity. If there are more than one MPCs arriving at a time, which are also distant in arriving angle and thus do not belong to the same cluster (as shown in Figure 24(c)), clustered results are inspected visually to check if the MPCs are separated correctly.

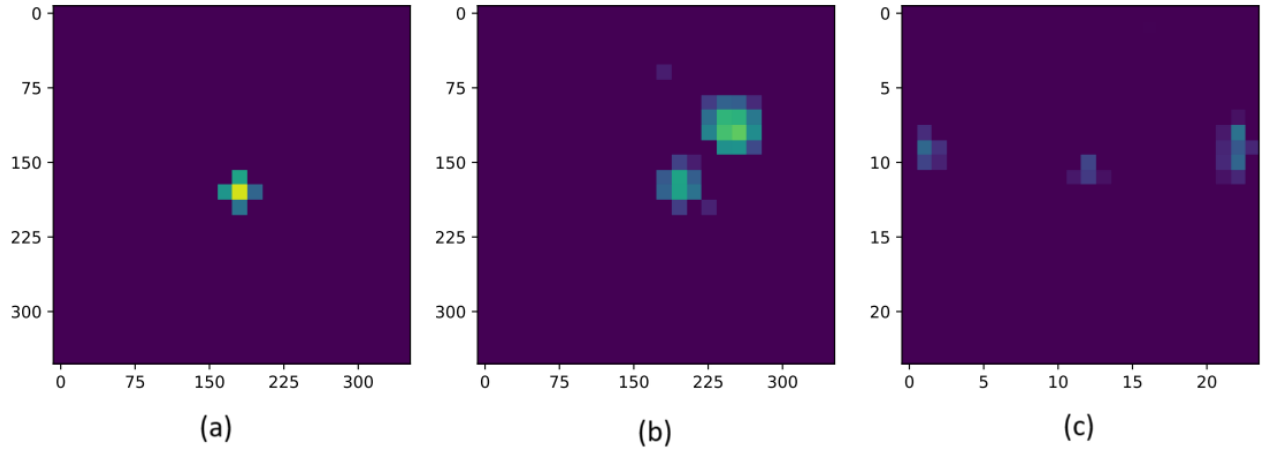

Figure 24 Heatmaps of multi-path components arriving in three different ways

Accuracy of time range separation: The accuracy of time range separation is evaluated only for measurements in which no multipath components (MPCs) from separate clusters arrive simultaneously. In Algorithm 5, each time step is assigned a cluster label based on the majority of cluster assignments for points within the corresponding frame. Ground truth labeling is conducted for selected pairs of transmitter–receiver (Tx–Rx) locations across all three frequency bands. The cases of TX1–RX1 and TX1–RX8 represent line-of-sight (LOS) conditions, while TX2–RX3 and TX2–RX6 represent non-line-of-sight (NLOS) conditions. Accuracy is quantified using the Adjusted Rand Index (ARI), as shown in Table 13. Higher ARI values (approaching 1) indicate stronger agreement between the experimental results and the ground truth. It is observed that DBSCAN with power distance outperforms the other three methods in 7 out of 12 cases, achieving the highest average accuracy. Notably, this method performs best in three out of four cases for the THz frequency band and in three out of four cases for the mmWave band. A general trend is also noted: clustering accuracy tends to increase with higher signal frequencies across all methods. This is attributed to the more rapid attenuation of high-frequency signals, which leads to clearer separation of arriving MPCs and thereby simplifies the clustering task.

Algorithm 5 Identifying MPCs' TIme Range

for $t \in K$ **do**
  $\mathbf{x}_t \leftarrow \{x'\}, \forall x'$ with $x_{\texttt{time}} == t$
  if $|\mathbf{x}_t \geq 1|$ **then**
    $c^t \leftarrow \texttt{mode}(\{c_x, x \in \mathbf{x}_t\})$
  else
    $c^t \leftarrow -1$
  end if
end for
return $\mathbf{c} = \langle c^t \rangle, \forall t \in K$

Table 13 Evaluation accuracy for selected Tx–Rx locations.

			K-means		DBSCAN	
TX	RX	Freq.	Eucl.	p-Dist.	Eucl.	p-Dist.
1	1	THz	0.787	0.835	0.951	0.951
		mmW	0.928	0.727	0.797	0.967
		Sub-6G	0.694	0.395	0.755	0.650
1	8	THz	0.712	0.978	0.862	0.780
		mmW	0.657	0.769	0.832	0.995
		Sub-6G	0.514	0.453	0.494	0.801
2	3	THz	0.990	0.985	1.000	1.000
		mmW	0.733	0.656	0.686	0.921
		Sub-6G	0.740	0.352	0.650	0.638
2	6	THz	0.806	0.750	0.998	0.999
		mmW	1.000	0.651	0.899	0.899
		Sub-6G	0.775	0.425	0.353	0.651
Average			0.778	0.665	0.773	0.854

Accuracy of simultaneous peak separation: The clustering results of the four methods for the multipath components (MPCs) illustrated in Figure 24(b) and Figure 24(c) are visualized and compared. In Figure 25, where the two arriving MPCs are also closely aligned in the angular domain and thus belong to the same cluster, correct clustering is achieved by all methods except K-means with power distance. Although it is practically feasible to separate these MPCs, K-means with power distance fails to correctly classify signals detected at the edge angles of the MPCs, as indicated by red-marked pixels in Figure 25. In contrast, when the two arriving MPCs are widely separated in the angular domain—as shown in Figure 26—and should ideally be assigned to different clusters, none of the four methods yields a perfect solution. The DBSCAN algorithm, as seen in Figure 26 (b) and Figure 26 (d), assigns all arriving signals at the same time step to a single cluster, regardless of the chosen distance metric. Meanwhile, the K-means algorithm succeeds in separating signals that are nearly 180° apart in transmission azimuth. However, K-means with Euclidean distance (Figure 26 (a)) does not distinguish the two noise signals at a 15° receiving azimuth. Similarly, K-means with power distance (Figure 26 (c)) fails to group the signals arriving from a 30° transmitter azimuth (shown in yellow) with other neighboring signals marked in red, despite their angular proximity.

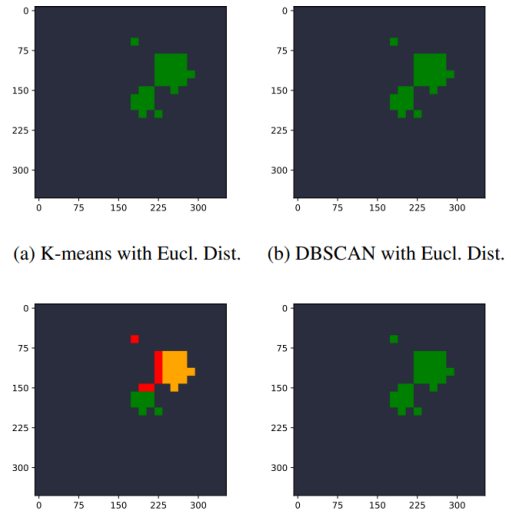

(a) K-means with Eucl. Dist. (b) DBSCAN with Eucl. Dist.

(c) K-means with Power Dist. (d) DBSCAN with Power Dist.

Figure 25 Clustering results for two MPCs in the same cluster arriving at the same time

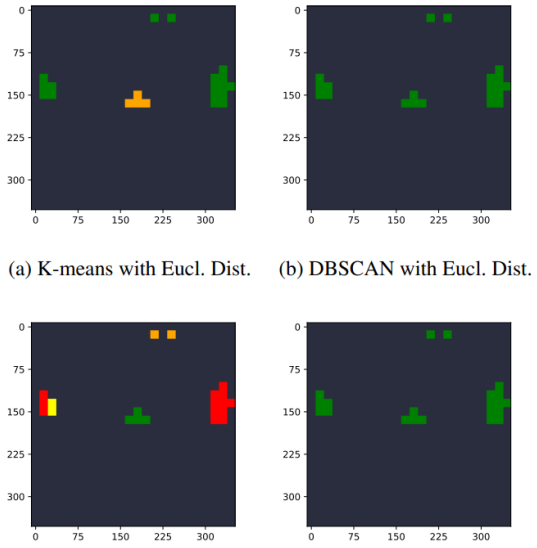

(a) K-means with Eucl. Dist. (b) DBSCAN with Eucl. Dist.

(c) K-means with Power Dist. (d) DBSCAN with Power Dist.

Figure 26 : Clustering results for two MPCs in different clusters arriving at the same time

Conclusions

In this section, two classic clustering algorithms were applied to multiband industrial wireless measurement data. Unlike previous approaches that begin by identifying multipath components (MPCs) from the measurements, a new process flow was proposed—comprising preprocessing, clustering, and post-processing steps—to facilitate the extraction of MPC cluster information.

Building upon insights from prior work, both the power distance metric and the traditional Euclidean distance were evaluated within the clustering algorithms. The effectiveness of clustering was assessed through time-range identification and peak separation tasks. It was found that DBSCAN performs well in identifying MPC

delays when only one MPC arrives at a given time. In contrast, when multiple MPCs arrive simultaneously, K-means demonstrates superior performance in separating them.

Additionally, the proposed method was observed to be particularly effective for clustering high-frequency signals (e.g., in the THz range), attributed to the clearer separation of arriving MPCs resulting from stronger attenuation. Future work will focus on automated parameter tuning of the clustering algorithms and a more detailed analysis of clustering outcomes under line-of-sight (LOS) and non-line-of-sight (NLOS) conditions.

Computer-Vision-Based Fast Indoor Map Generation

An enhanced convolutional model for indoor radio map generation is introduced in this section, with a focus on integrating a novel ray-marching feature. The proposed method incorporates a ray-marching feature alongside a UNet architecture augmented with dilated convolution layers, leading to notable improvements in indoor pathloss prediction accuracy.

Background

The generation of indoor radio maps—crucial for optimizing wireless communication systems such as Wi-Fi and cellular networks—has traditionally relied on computationally intensive ray tracing techniques. While these methods simulate electromagnetic wave propagation with high fidelity, they are resource-demanding and poorly suited for real-time or scalable applications, particularly in dynamic environments. Their limitations are further amplified by the challenges of modeling complex indoor spaces and the need to recompute maps with every change in antenna placement or environmental obstacles. Moreover, ray tracing approaches struggle in scenarios with incomplete input data.

To overcome these limitations, machine learning (ML) models offer a scalable and adaptive alternative. By learning from measurement data, ML algorithms are capable of capturing complex relationships between environmental characteristics and radio wave behavior, thereby enabling efficient and real-time updates of radio maps with minimal computational cost.

In this section of work, convolutional neural networks were enhanced with a novel ray-marching feature to improve path loss (PL) predictions. A transmittance spread feature—derived from wall transmittance values—was introduced alongside other relevant inputs such as frequency and antenna information. An adapted UNet architecture, incorporating dilated convolution layers, was employed to achieve fast convergence and high accuracy in generalizable PL predictions.

The dataset used for the task in this section is from [**Bak2024**] and its complexity increases progressively across the stages. The initial dataset consists of measurements at 868 MHz using an omni-directional antenna, collected from 50 transmitter locations across 25 buildings. The corresponding test set is drawn from 6 unseen buildings, introducing spatial generalization. Subsequently, the dataset is expanded to evaluate generalization across multiple frequency bands by incorporating measurements at 1.8 GHz and 3.5 GHz in addition to 868 MHz. The test set for this stage includes samples at 868 MHz and a previously unseen frequency of 2.4 GHz. Finally, the dataset is extended to include variation in antenna patterns. Five different antennas are used during training—one of which is omni-directional—while the test set includes two entirely new antenna patterns alongside the omni-directional antenna. This stage introduces additional complexity through antenna diversity and pattern generalization. In all cases, the transmitter (Tx) height is fixed at 1.5 m above the floor, with the path loss (PL) sampled on a receiving plane at the same height. The spatial resolution is set to 0.25 m, meaning PL is sampled every 0.25 m. Ray tracing is performed with up to 8 reflections, 10 transmissions, and 2 diffractions per ray path. The input images are in RGB format. The first two channels encode (i) normal incidence reflectance and (ii) incidence transmittance in decibels at each

point in the grid (both zero for air), while the third channel contains the physical distance from the Tx to each point. Each sample additionally includes metadata such as the Tx location, operating frequency, and antenna radiation pattern. The target PL maps are represented as grayscale images, with values ranging from 13 dB to 160 dB.

Method

Data Processing: The original RGB input channels—distance, transmittance, and reflectance—are preprocessed to generate additional feature-engineered channels. Samples of both the original and processed features are shown in Figure 27. All inputs images are resized to 512 by 512 pixels using bilinear interpolation and further augmented during training with flipping and rotation.

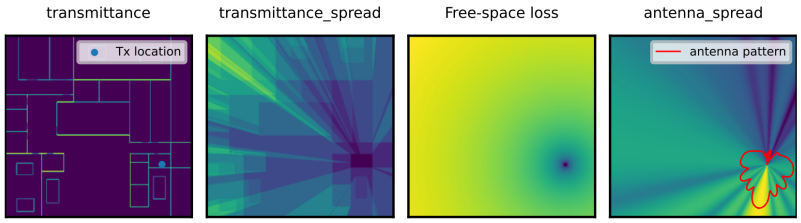

Figure 27 Selected input features for computer-based radio map generation.

Additional Feature 1: Ray Marching-Based Features

The original RGB channels exhibit distinct spatial characteristics, with the reflectance and transmittance channels being particularly sparse (as seen in the sampled transmittance feature in Figure 27). To address this, an alternative representation is derived from these channels to enhance processing efficiency by convolutional filters in U-Net-like architectures, which are limited in their ability to capture non-local dependencies due to the locality of convolution operations.

This enhanced representation enables the model to capture more global spatial relationships. The method is inspired by ray marching techniques: from each transmitter location, rays are cast in the 2D plane, and transmittance and reflectance values are accumulated along each ray using numerical integration. A new value is computed for each pixel as:

$$T_{spread}(x,y) = \int_{x_0,y_0}^{x,y} t(x,y)\, ds \tag{46}$$

The parameter t denotes the individual transmittance or reflectance values of objects (e.g., walls) in the environment. The integration process involves summing contributions along small segments ds from the transmitter's location x_0, y_0 to the target location x, y.

Additional Feature 2: Free-Space Loss

Based on the transmitter location, an additional feature representing the free-space PL is incorporated into the learning input: $L_{\text{fs}} = -10\log(G_t G_r) + 20\log(4\pi) + 20\log(d \cdot f/c)$. d is the propagation distance, c is the speed of light and f is the corresponding signal frequency. G_t and G_r are the gains of the transmitter and receiver antennas and set to 1 in the experiments. This feature is frequency-dependent and provides a more accurate approximation of PL compared to using distance alone.

Additional Feature 3: Antenna Pattern Spread

Based on the transmitter's location and orientation, an additional feature capturing the antenna gain was derived. For this feature, each pixel value is determined by the gain associated with the angle between the pixel's position and the transmitter's orientation.

Convolutional Neural Network Structure

A modified U-Net architecture, referred to as Split U-Net, was devised, incorporating two parallel encoder-decoder streams. One stream was designed to handle sparse input features (transmittance, reflectance) using stacked dilated convolutions for multi-scale feature extraction. The second stream was tasked with processing spatially dense features (distance, antenna pattern, free-space loss, and ray-marching-based feature) using standard UNet structure as described in [**Ron2015**]. The latent representations from both decoder branches were concatenated prior to the final 1×1 convolutional layer, which generates the PL map. This design is based on the intuition that absorption characteristics can be effectively learned from ray-marching-derived features, whereas reflection patterns are better inferred through the surface reflectance data.

Regularized Perceptual Loss

For training, a convex combination of mean squared error (MSE) loss and a perceptual loss based on structural similarity (SSIM) was employed. The total loss function was defined as follows, with $\alpha = 0.8$:

$$L = \alpha \cdot \mathrm{MSE} + (1 - \alpha) \cdot (1 - \mathrm{SSIM}) \tag{47}$$

Results and Discussions

Illustrative qualitative results on a held-out validation set are presented in Figure *28*. When the proposed method was applied to third-stage dataset, training converged after three epochs of optimization, achieving a root mean square error (RMSE) of 7.75 on the training data. On the final test set, RMSE values of 8.09, 10.94, and 11.54 were obtained for Stage 1, 2, and 3, respectively.

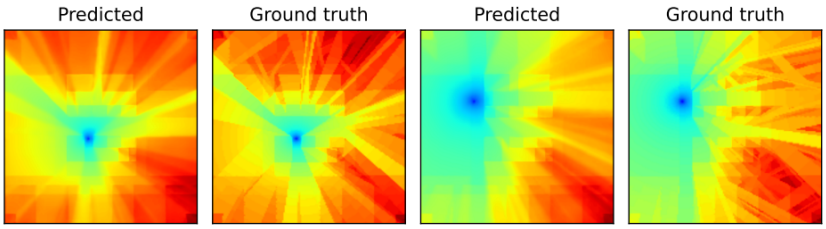

Figure 28 Qualitative results on selected samples.

Based on visual inspection, the reflection effects—particularly in areas farther from the transmitter—remain a challenging aspect of the problem. Potential research directions to address this issue include the application of Vision Transformers (ViTs) and the augmentation of training data through selective ray-tracing simulations. Despite of these limitations, the proposed solution has performed well overall, ranking third in the IEEE ICASSP 2025 First Indoor Path Loss Prediction Challenge (https://2025.ieeeicassp.org/sp-grand-challenges/).

5 Ray tracing approaches for THz channel modeling

Focusing on ray-tracing (RT) simulations, this section quantifies the path loss and shadowing of THz channels in diverse industrial scenarios, by using detailed 3D environmental models defined within TIMES. Furthermore, analysis of the second-order statistics that are critical for system-level THz communication design are presented.

Evaluation of path loss and shadow fading in industrial scenarios

This section aims to evaluating the path loss and shadow fading statistics in industrial scenarios, with two different comparisons in mind. Specifically:

i. Comparing the path loss and shadow fading simple industrial scenarios with real and complex industrial plants, such as Robopac-Aetna Group and the Bi-Rex pilot line [**TIMES2023-4**];
ii. Comparing the path loss and shadow fading in different frequency bands (specifically, 3.7 GHz, 27 GHz, and 300 GHz).

The simulation of signal propagation within the industrial plants is performed using 3DScat RT tool (**[Vit2015]** and **[Fus2015]**). The objective is to extrapolate the major large-scale channel parameters, such as the path loss and the shadowing standard deviation, for base station (BS)-to-node and node-to-node communications at sub-6 GHz, mmWaves, and THz frequencies. The investigation aims to analyse the variation of path loss and standard deviation of shadowing in the considered scenarios for different candidate frequencies and transmitter heights.

Scenario

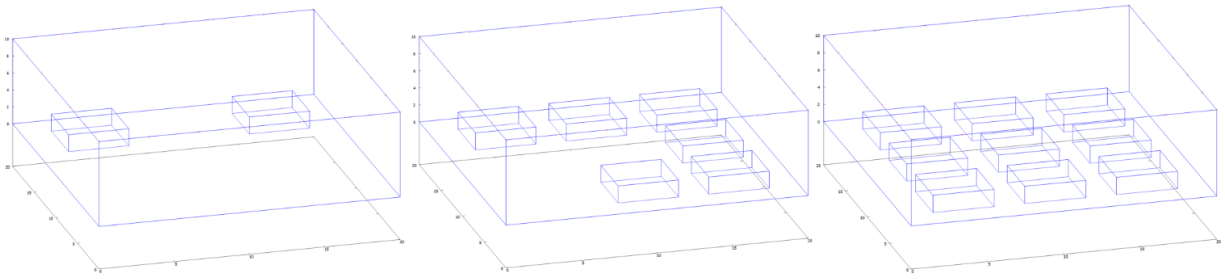

(a) $OD = 0.08$ (b) $OD = 0.24$ (c) $OD = 0.36$

Figure 29 Reference scenario industrial environments.

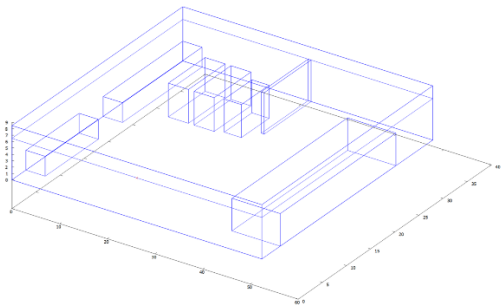

Figure 30 Robopac-Aetna Group industrial environment.

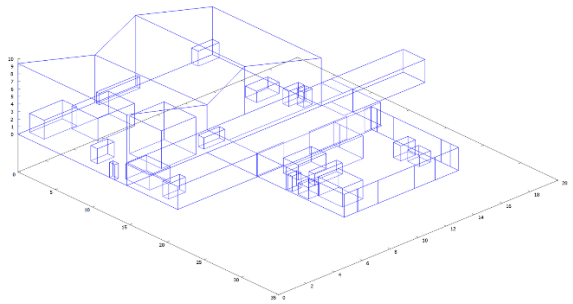

Figure 31 Bi-Rex pilot line.

The industrial scenario considered is a plant of size $W_x x W_y x W_z$ m^3 in which a set of O obstacles with size $O_x x O_y x O_z$ m^3 is located. Obstacles can be classified into sets of M machines of size $M_x x M_y x M_z$ m^3, C closed rooms of size $C_x x C_y x C_z$ m^3, and E additional elements of size $E_x x E_y x E_z$ m^3; therefore O = {M ∪ C ∪ E}. The obstacles' density is defined as $OD = \frac{\sum_{i=1}^{O} A_{O_i}}{A_W}$, where A_{Oi} is the area occupied by obstacle i∈O and A_W is the plant's area. Any element of the plant that may impede the direct communication between TX and RX, such as machinery and panels, is considered as obstacle. The evaluation of channel propagation includes BS-to-node communication, simulating uplink and downlink, as well as node-to-node communication simulating sidelink, where devices can directly communicate without the presence of an intermediate BS. For BS-to-node communication it is considered a transmitter placed in (x_{tx}, y_{tx}, z_{tx}) and a set of R RXs located in ($x_{rx,j}$, $y_{rx,j}$, $z_{rx,j}$) with j∈R. Every RX can either operate as an automated guided vehicle (AGV) or as a sensor located on a machine, hereafter denoted as machine node (MN).

Thus, three distinct links are considered for various node functionalities: BS to AGV (BS2AGV), BS to MN (BS2MN), and a combination of the previous BS to AGV & BS to MN (BS2AGV&BS2MN). The BS has a TX height z_{tx} which is limited to a range of $z_{tx} \in [z_{tx,min}, z_{tx,max}]$, with $z_{tx,min} \geqslant Mz$ and $z_{tx,max} \leqslant Wz$. Regarding the RXs, they have a height of $z_{rx} \in \{0.3, 0.5, 1\}$m for AGVs, $z_{rx,m} \in [0, M_{z,m}]$ for MN located along the edges of machine m∈M , and $z_{rx,m} = M_{z,m} + \delta$ with δ = 0.01m for MN located on top of machine m∈M. In the context of node-to-node communication, a set of T TXs is located in ($x_{tx,k}$, $y_{tx,k}$, $z_{tx,k}$) with k∈T , and a set of R RXs is placed in ($x_{rx,j}$, $y_{rx,j}$, $z_{rx,j}$) with j∈R. Each node, either TX or RX, can function as AGV or MN. Consequently, three different links are evaluated for various nodes functionalities: AGV to AGV (AGV2AGV), MN to MN (MN2MN), and a combination of the previous MN to AGV & AGV to MN (MN2AGV&AGV2MN). For simplicity TXs and RXs in both macro-scenarios (BS-to-node and node-to-node communications) are equipped with omnidirectional antennas.

1) Reference scenario: represents an ideal facility of size 20x20x10m^3 in which it is located a set of M machines arranged unevenly with same size 4x4x2m^3, inter-machine distance d_{M2M} = 2m, machine-wall distance d_{M2W} = 2m, and obstacles' density OD. To that purpose three sub-scenarios were constructed, each comprising M = {2, 6, 9} machines with OD = {0.08, 0.24, 0.36}, respectively (Figure *29*). The walls, floor, and ceiling of the plant are constructed from concrete, while the machines are manufactured from metal and considered as PECs.

2) Robopac-Aetna Group scenario [**TIMES2023-4**]: is a warehouse with size 52.37x35.4x8.5m^3 and OD = 0.23. It consists of C closed rooms divided in some offices and a meeting room, as well as an additional element E (a panel), and M = 3 packing machines with size 4.2x7.6x5.3m^3, as shown in Figure *30*. The construction of the plant walls is based on a concrete foundation, with the offices and conference rooms constructed from

glass and wood, respectively. The ceiling and floor are composed of typical state-of-the-art (SOTA) materials [**Rec2021**]. The panel is made of plywood, while the packing machines are modelled like parallelepipeds composed of metal.

3) Bi-Rex scenario [**TIMES2023-4**]: is a complex industrial plant, as illustrated in Figure *31*, comprising two macro-rooms: the pilot line of size 21.45x13.92x9.36m^3 and a secondary area of size 11.59x8.6x3.025m^3, with OD = 0.08. It is equipped with a set of M = 18 machines, including printers, assembly, packing, and measurement stations, as well as a set of additional elements, E, such as tables and stairs. Signal propagation is evaluated between rooms in a scenario with a not-flat ceiling. The plant walls are constructed from a variety of materials, including concrete, glass, and plywood. The machines are made of metal, while the tables and stairs are constructed from wood and concrete, respectively. The ceiling and floor are composed of SOTA materials [**Rec2021**].

The electromagnetic parameters of the materials for different working frequencies (sub-6 GHz, mmWaves, and THz) are described through the relative dielectric constant ϵ_r and the electrical conductivity σ, listed in Table *14* and derived from [**Rec2021**].

Table 14 RT materials characterization [**Rec2021**].

Frequency	Characterization	Ceiling	Concrete	Floor	Glass	Metal	Plywood	Wood
3.6 GHz	ϵ_r	1.48	5.28	2.73	6.31	0	3.17	1.992
	σ	0.0044	0.12	0.03	0.02	10^7	0.33	0.0185
27 GHz	ϵ_r	1.48	5.25	2.73	6.31	0	2.72	1.993
	σ	0.04	0.61	0.19	0.3	10^7	0.33	0.161
300 GHz	ϵ_r	1.52	5.24	2.73	5.8	0	2.71	1.994
	σ	1.03	4	1.80	5.12	10^7	0.33	2.12

Channel Modelling

Signal propagation in the industrial layout is modelled using a narrowband channel model assuming to be in far field condition, for which $d \gg \lambda$. It is adopted the close-in free space reference distance path model, since it has proven to be superior for modeling path loss over many environments and frequencies [**Ju2023**]. The path loss PL is described as: $PL(d) = c + 10\alpha\log10(d) + \xi$. Where d represents the 3D distance between transmitter and receiver, $c = 20\log10(4\pi/\lambda)$ is the path loss at a reference distance d_{ref} = 1m, α is the PLE, and ξ stands for the additional attenuation caused by shadowing. Shadowing is a phenomenon that occurs due to the existence of obstacles in between TX and RX direct link which generates slow fluctuations. It is a large scale effect modelled as a Gaussian distribution $\xi \sim N(0, \sigma^2)$ zero mean with standard deviation σ.

Numerical Results

This section presents the obtained results in terms of PLE and standard deviation of shadowing for the considered facilities at various frequencies and TX height. The transmitted power is P_t = 0 dBm, TX and RX gains are G_t, G_r = 0 dB, and the working frequencies are f = 3.6, 27, 300 GHz.

A. Path Loss Exponent

The following Figures depict the PLE, α, in relation to the TX height, z_{tx}, and frequency in LoS/NLoS conditions for BS-to-node and node-to-node communications for reference scenarios with OD = {0.08, 0.24, 0.36}, Robopac-Aetna Group, and Bi-Rex plants.

1) Reference Scenario: Results indicate that PLE in NLoS increases with frequency in all scenarios (Figure *32*). This behaviour is closely related to OD and to the layout's specificity. Indeed, the number and type of interactions vary in accordance with the quantity of obstructing elements. In BS2AGV scenario the PLE in LoS is nearly constant at around α=2, instead, BS2MN exhibits an oscillation of PLE with a peak at z_{tx} = 7m, while BS2AGV&BS2MN is a trade-off. NLoS component is strictly related to the variation of the TX height and this behaviour becomes more pronounced at higher frequencies. PLE for BS2MN in NLoS is higher with respect to that of BS2AGV. Regarding PLE variation with frequency (Figure *35*), results indicate that it increases with frequency in NLoS, while it remains nearly constant or decreases in LoS. Also, different PLE behaviours are observed for various OD, as it is closely linked to the specificity of the scenario. Finally, PLE experienced by MN2MN is higher than that of AGV2AGV links, while that of MN2AGV&AGV2MN is a trade-off.

2) Robopac-Aetna Group: Findings highlight that an increase in the frequency leads to an increase in PLE in NLoS, while it remains almost constant in LoS (Figure 32). PLE in LoS/NLoS for BS2AGV is nearly constant at the variation of the TX height, while for BS2MN it decreases in NLoS and increases in LoS. BS2AGV&BS2MN scenario has a PLE behaviour which is a trade-off between those previously described. Regarding PLE variation with respect to frequency (Figure 35), the NLoS components tend to increase, while those in LoS decrease. MN2MN scenario exhibits the highest PLE, AGV2AGV has the lowest, while MN2AGV&AGV2MN is a trade-off in both LoS/NLoS conditions. Finally, it is worth noticing that PLE for node-to-node links is higher than that for BS-to-node communications in LoS/NLoS.

3) Bi-Rex: Results prove that PLE in NLoS increases with the TX height for BS2AGV and BS2AGV&BS2MN, while it remains constant for BS2MN links (Figure *34*). The PLE in LoS for BS2AGV, BS2MN, and BS2AGV&BS2MN is practically unaltered at around α = 2 at f = 27 and 300 GHz, while it is larger at 3.6 GHz. Indeed, in the latter case, links overcome the break-point distance and experience higher attenuation. A more accurate fit would be obtained with a dual-slope channel model, not considered in this section to perform a fair comparison with other frequencies. Regarding PLE variation with respect to frequency (Figure *36*), it increases in NLoS and decreases in LoS. MN2MN scenario exhibits the highest PLE, AGV2AGV has the lowest, while MN2AGV&AGV2MN represents a trade-off. In contrast to other plants this facility presents a different layout, comprising heterogeneous walls and a non-flat ceiling.

The two real industrial settings have similar channel behaviour for node-to-node communications, while they experience opposite trends for BS-to-node links. This finding highlights the influence of a different TX-RX location on channel propagation, and consequently, on network performance.

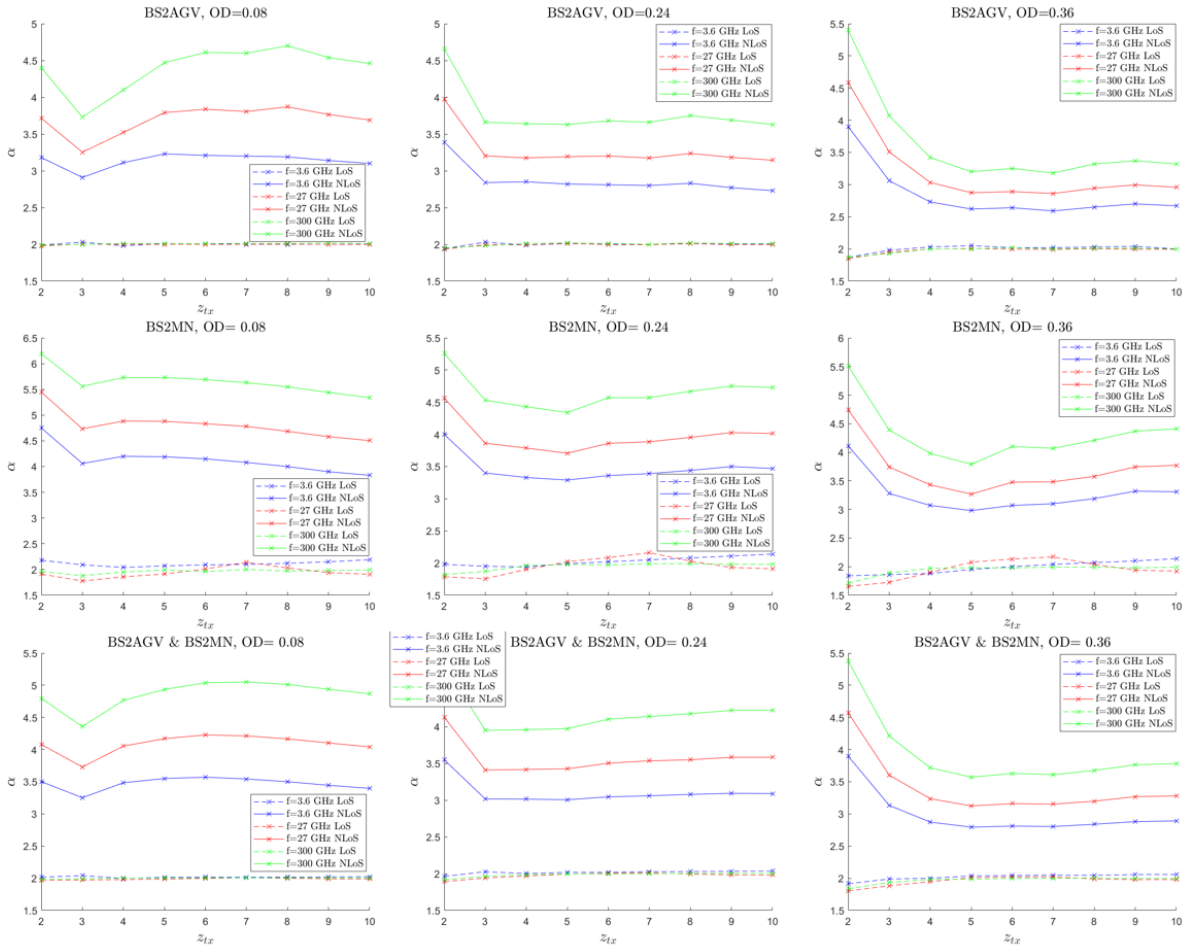

Figure 32: PLE variation with ztx for reference scenarios for BS-to-node links.

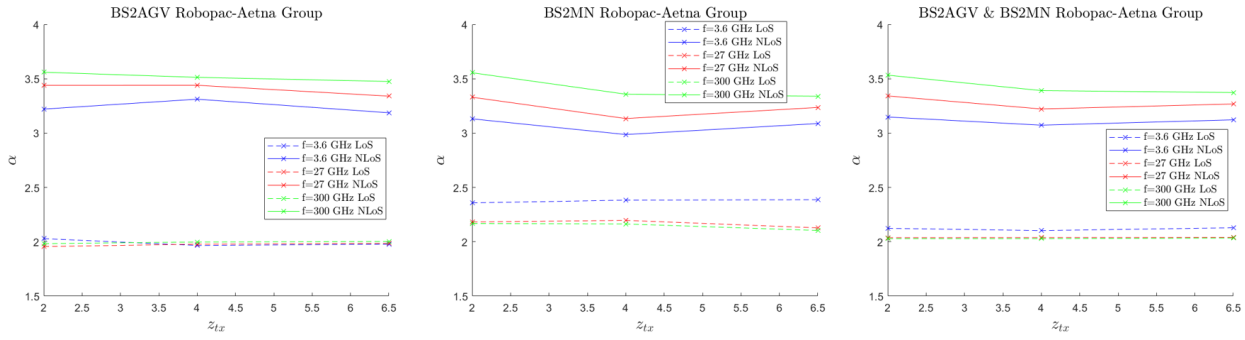

Figure 33 PLE variation with ztx for Robopac-Aetna Group for BS-to-node links.

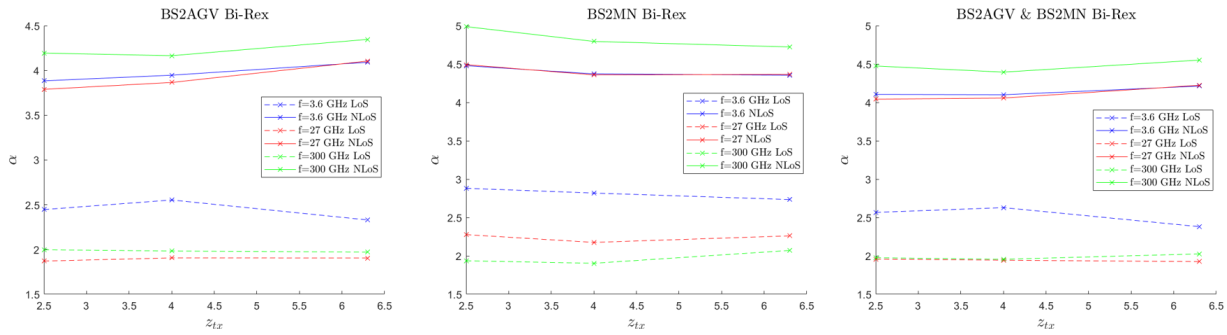

Figure 34 PLE variation with ztx for Bi-Rex for BS-to-node links.

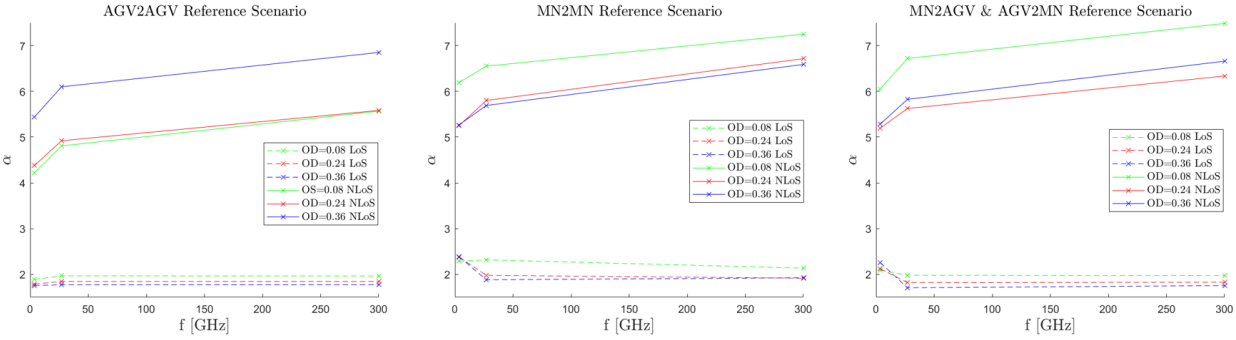

Figure 35 PLE variation with f for reference scenarios for node-to-node links.

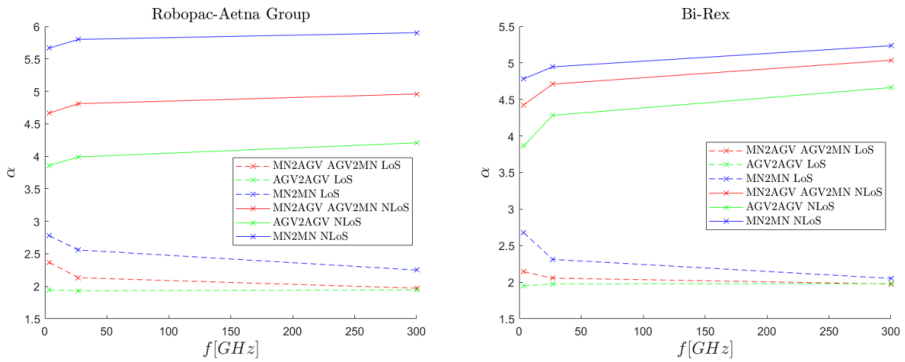

Figure 36 PLE variation with f for Robopac-Aetna Group and Bi-Rex for node-to-node links.

B. Shadowing

Table 28 and Table 29 list the standard deviation of shadowing in LoS/NLoS for BS-to-node and node-to-node links at various frequencies for reference scenarios with OD = {0.08, 0.24, 0.36}, Robopac-Aetna Group, and Bi-Rex plants.

1) Reference Scenario: From results emerge that the shadowing standard deviation in NLoS increases with frequency for all scenarios, whereas in LoS it decreases for BS2MN and increases for BS2AGV and BS2AGV&BS2MN. Also, the standard deviation in LoS/NLoS for BS2MN is greater than that for BS2AGV and its value is closely linked to that of OD. Regarding node-to-node communication, the shadowing standard deviation in LoS for MN2MN and MN2AGV&AGV2MN decreases with frequency, while it oscillates for AGV2AGV. In NLoS it increases with frequency for AGV2AGV and oscillates for MN2MN and MN2AGV&AGV2MN. Also, the one of MN2MN is higher than that of AGV2AGV, while that for

MN2AGV&AGV2MN is a trade-off. Consequently, the standard deviation of shadowing for node-to-node communications is higher than that for BS-to-node links in LoS/NLoS.

2) Robopac-Aetna Group: Findings highlight that the shadowing standard deviation of BS2MN is greater than that of BS2AGV in LoS/NLoS, while that of BS2AGV&BS2MN is a trade-off. In terms of node-to-node communication, the shadowing standard deviation of MN2MN is greater than that of AGV2AGV, while that of MN2AGV&AGV2MN is a tradeoff in both LoS/NLoS.

3) Bi-Rex: Results indicate that the standard deviation of shadowing in NLoS of BS2MN is lower than that of BS2AGV, while that of BS2AGV&BS2MN is a trade-off. Also, it increases with frequency in NLoS condition. For what concerns node-to-node communication, the standard deviation in LoS decreases with frequency, while it increases in NLoS. Additionally, the one of MN2MN is higher than that of AGV2AGV for LoS/NLoS, while MN2AGV&AGV2MN represents a trade-off. Finally, as observed in the previous scenarios, the standard deviation of shadowing for node-to-node communications is higher than that for BS-to-node links in LoS/NLoS condition.

Table 15 Shadowing standard deviation for BS-to-node links in reference scenario, Robopac-Aetna Group, and Bi-Rex.

Parameters			**BS2AGV&BS2MN**		**BS2AGV**		**BS2MN**	
Scenario	f	OD	σ_{LoS}	σ_{NLoS}	σ_{LoS}	σ_{NLoS}	σ_{LoS}	σ_{NLoS}
Reference Scenario	3.6 GHz	0.08	[2.77, 3.40]	[6.03, 9.17]	[0.93, 2.12]	[1.52, 5.15]	[3.19, 5.45]	[4.49, 8.36]
		0.24	[3.62, 4.38]	[7.05, 10.50]	[1.43, 2.59]	[4.07, 7.01]	[3.13, 4.84]	[5.39, 9.70]
		0.36	[4.36, 4.78]	[7.21, 10.19]	[1.96, 2.23]	[4.81, 6.59]	[2.58, 4.82]	[5.33, 7.54]
	27 GHz	0.08	[2.29, 3.13]	[6.48, 10.98]	[0.87, 2.00]	[1.03, 6.79]	[2.05, 3.61]	[2.88, 7.97]
		0.24	[2.85, 4.06]	[9.37, 12.60]	[1.19, 2.90]	[4.45, 9.18]	[2.55, 3.93]	[5.57, 11.67]
		0.36	[3.56, 4.29]	[9.61, 11.09]	[1.54, 1.97]	[5.91, 7.48]	[1.64, 3.32]	[5.15, 6.51]
	300 GHz	0.08	[2.39, 3.14]	[6.82, 12.89]	[0.98, 2.25]	[1.90, 8.51]	[2.29, 3.56]	[4.60, 8.64]
		0.24	[3.09, 4.06]	[12.27, 15.17]	[1.24, 2.64]	[8.61, 11.11]	[2.31, 3.36]	[7.46, 11.72]
		0.36	[3.77, 4.16]	[12.32, 13.77]	[1.86, 2.74]	[8.41, 10.96]	[1.88, 3.46]	[7.41, 9.96]
Robopac-Aetna Group	3.6 GHz	0.23	[3.31, 3.94]	[5.61, 7.18]	[2.48, 2.62]	[5.60, 7.80]	[4.09, 4.22]	[5.02, 6.83]
	27 GHz	0.23	[2.94, 3.96]	[5.82, 6.80]	[2.34, 2.45]	[4.86, 6.28]	[4.05, 4.39]	[5.84, 6.86]
	300 GHz	0.23	[3.12, 3.66]	[6.07, 6.62]	[2.32, 3.03]	[5.24, 6.66]	[4.01, 4.38]	[6.25, 7.16]
Bi-Rex	3.6 GHz	0.08	[2.18, 4.22]	[7.92, 11.03]	[2.23, 2.69]	[6.61, 11.76]	[2.02, 4.02]	[5.59, 7.57]
	27 GHz	0.08	[1.91, 5.62]	[7.92, 12.01]	[1.96, 3.80]	[8.40, 13.67]	[3.01, 5.79]	[6.43, 7.79]
	300 GHz	0.08	[1.71, 4.48]	[9.74, 14.02]	[3.38, 4.70]	[9.58, 14.22]	[3.07, 3.50]	[8.26, 8.41]

Table 16 Shadowing standard deviation for node-to-node links in reference scenario, Robopac-Aetna Group, and Bi-Rex.

Parameters			MN2AGV&AGV2MN		AGV2AGV		MN2MN	
Scenario	f	OD	σ_{LoS}	σ_{NLoS}	σ_{LoS}	σ_{NLoS}	σ_{LoS}	σ_{NLoS}
Reference Scenario	3.6 GHz	0.08	5.31	24.11	3.03	11.31	9.91	25.14
		0.24	5.38	22.51	3.95	16.64	8.75	21.60
		0.36	5.43	18.75	4.24	14.91	5.86	20.30
	27 GHz	0.08	4.62	23.86	3.21	12.62	7.15	23.07
		0.24	5.11	22.93	3.93	19.11	7.56	21.74
		0.36	4.90	19.82	4.06	16.27	5.82	20.84
	300 GHz	0.08	3.98	22.81	3.21	14.52	2.87	20.17
		0.24	4.50	23.74	3.88	21.79	4.20	21.49
		0.36	4.51	20.50	3.95	17.54	4.80	21.50
Robopac-Aetna Group	3.6 GHz	0.23	5.86	15.30	3.65	12.31	8.61	14.90
	27 GHz	0.23	4.81	15.40	3.76	13.57	7.83	14.41
	300 GHz	0.23	3.92	15.94	3.66	14.66	7.67	14.69
Bi-Rex	3.6 GHz	0.08	3.23	13.45	2.55	11.10	7.06	12.70
	27 GHz	0.08	3.11	13.31	2.32	12.43	4.51	12.95
	300 GHz	0.08	3.10	13.98	2.16	14.10	4.70	13.53

Final Remarks

This section investigated signal propagation simulated with the 3DScat RT tool in industrial settings for IIoT applications. It compared reference elementary scenarios with existing industrial plants, such as those of Robopac-Aetna Group and Bi-Rex ([**TIMES2023-4**]). The main goal was the analysis of the variation of PLE and shadowing standard deviation for BS-to-node and node-to-node communications at sub-6 GHz, mmWaves, and THz frequencies in which nodes can either work as AGVs or MNs. It was observed that the investigated scenarios, despite differing in size, obstacle density, and material composition, exhibited comparable trends in terms of PLE and shadowing standard deviation when the working frequency and TX height were varied. Additionally, as expected node-to-node communications have a higher level of PLE and shadowing standard deviation compared to BS-to-node links. Indeed, in the first scenario, the TX is situated at a lower height, resulting in a higher number of obstacles being encountered by the direct path between TX and RX.

Analysis of second-order statistics of industrial THz channels

This section deals with the ray tracing-based analysis second order statistics of the wireless channel at 300 GHz in the indoor industrial environment, focusing on RMS delay spread and coherence bandwidth. Ray tracing simulations are performed using a digital model of the BiREX Pilot Plant consisting of a large rectangular factory hall with concrete walls. The room has a concrete staircase approximately in the middle and along the walls there are several metallic cabinets and various industrial machines. Also, there are few pieces of wooden furniture such as tables and chairs. The model is depicted in Figure 37, where we use colours to distinguish the different materials. The ceiling of the room is made transparent for better visibility of the inner arrangement, but for the ray tracing purposes, it is considered as made of concrete. We utilize three different scenarios in our simulation:

- Sparse clutter (SC) scenario: The clutter level is approximately at 7 %. In this scenario we have five TXs in total, one TX in each corner of the room and one in the middle. RXs are placed in a 10 × 10 grid. TXs are depicted with red spheres, while RXs are shown in blue.
- Dense clutter (DC) scenario, depicted in Figure *37*. The clutter level is approximately at 40 %. In this scenario we increase the clutter level by incorporating several large metallic installations, each differently rotated. Those metallic structures represent industrial machines of a rectangular shape. The TX and RX placement is identical to the Sparse clutter scenario.

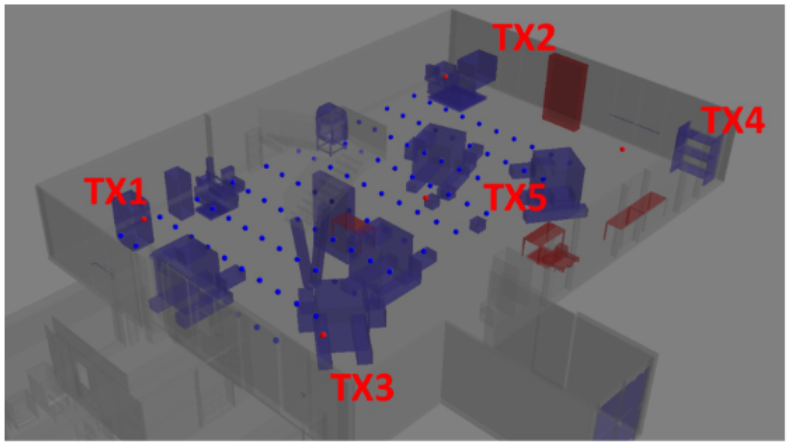

Figure 37 Simulated scenarios of an indoor factory environment. 100 RX positions placed in 10×10 grid and 5 TX locations as depicted above are considered. The depicted Dense clutter (DC) scenario's clutter density is approx. 40%.

The RX and TX placement is different compared to the other introduced scenarios. In this case, there is a central TX and two RX areas, where one area is a LOS area and other group of RX locations experience NLOS. In total we have 20 RX locations. As for the number of trajectories, we simulate 10 random parabolic trajectories with various length and curvature, each with 10 positions of the sensed object. This scenario then assumes 3 antenna setups, (1) omni-to-omni and directive antenna with (2) 4×4 and (3) 8×8 element setups. Thus, simulating this scenario we obtained 6000 Channel Impulse Responses (CIRs).

The result of the ray tracing is a band-unlimited time invariant CIR given as:

$$h''(\tau, \phi, \psi) = \sum_k a_k(\tau, \phi, \psi) \cdot \delta(\tau - \tau_k),$$

where a_k is a complex coefficient representing the power of the k-th MPC, δ is a function locating the MPC in the delay domain and ϕ and ψ represents the angular information for each MPC in terms of azimuth and elevation angles respectively. In this case, the CIR is assumed omni directional. In this work, we compare two situations: (i) omnidirectional TX and omnidirectional RX antennas, and (ii) directive TX and omnidirectional RX antennas. When considering directional antennas, the channel impulse response is multiplied with respective antenna radiation patterns $g_t(\phi, \psi)$ and $g_{r_i}(\phi, \psi)$ representing the TX and RX antennas as:

$$h'(\tau) = \sum_{\phi} \sum_{\psi} h''(\tau, \phi, \psi) \cdot g_t(\phi, \psi) \cdot g_{r_i}(\phi, \psi).$$

The $h'(\tau, \phi, \psi)$ always contains the angular information, but for the ease of manipulation, in the following we drop the ϕ, ψ parameters meaning that $h'(\tau, \phi, \psi) = h'(\tau)$. To emulate beam steering operations, antennas are rotated towards the direction from which the MPC with the maximum energy is received. To this aim, we implemented a two-stage ray tracing procedure. In the first stage, we perform a simulation with omnidirectional antennas with the purpose of finding the best beam direction. In the second stage, we apply the antenna radiation pattern and rotate the antenna towards the best beam direction. For further processing, we limit the bandwidth of the CIR via sinc pulse shaping as $h(\tau) = \sum_\tau h'(\tau) \cdot \mathrm{sinc}(\mathrm{l} - W\tau_m)$, where W is the bandwidth. Throughout this section we limit the channels to 2 GHz of bandwidth.

The PDP is defined as a temporal average of the CIR:

$$P(\tau) = lim_{t \to T_s} \frac{1}{2T} \int_0^{Ts} |h(t, \tau)|^2 dt.$$

Since ray tracing is a deterministic process and the ergodicity holds, we can write the PDP as $P(\tau) = |h(\tau)|^2$. The zeroth-order moment of the PDP represents the received power $P_{\mathrm{RX}} = \sum_\tau P(\tau)$.

RMS delay spread

An important parameter describing multi-path richness or channel dispersion in delay domain is the second-order central moment of the PDP, referred to as the RMS delay spread:

$$D_{RMS} = \sqrt{\frac{\sum_\tau (\tau - \bar{\tau}^2) P(\tau)}{\sum_\tau P(\tau)}}, \text{ where } \bar{\tau} = \frac{\sum_\tau \tau P(\tau)}{\sum_\tau P(\tau)}$$

Figure 38a and Figure 38b show the CDF of the RMS in LOS and NLOS conditions, respectively. In each case, we considered both SC and DC scenarios and different antenna configurations. For a better comparison, we also reported mean values of the RMS delay spread in Tab. I. When calculating the mean value of the RMS delay spread over all RX and TX combinations, we see RMS delay spreads of 8.6 ns to 51 ns in LOS and NLOS respectively, assuming the directive 4×4 to omni antenna setup. When the omni-to-omni is assumed, we report higher values of 48 ns to 55 ns again for LOS and NLOS. The RMS delay spread is higher in NLOS conditions given the lack of a dominant MPC. When considering directional antennas, the RMS delay spread decreases.

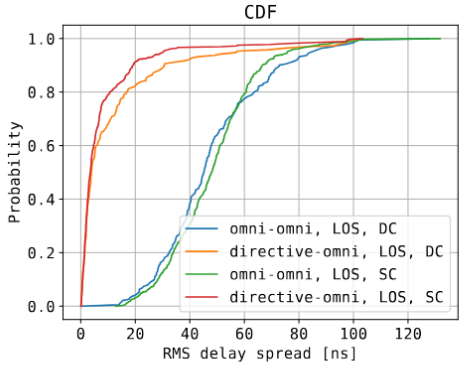

(a) Cumulative distribution function (CDF) of the RMS delay spreads. Comparison of the dense clutter and sparse clutter scenarios in LOS condition.

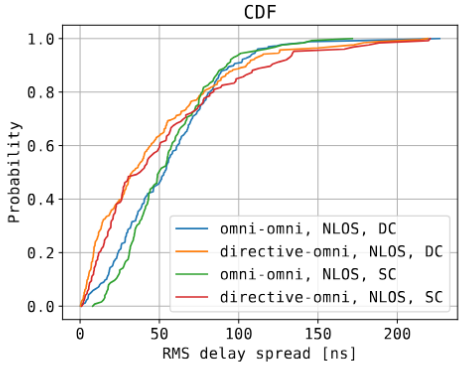

(b) CDF of the RMS delay spreads. Comparison of the dense clutter and sparse clutter scenarios in NLOS condition.

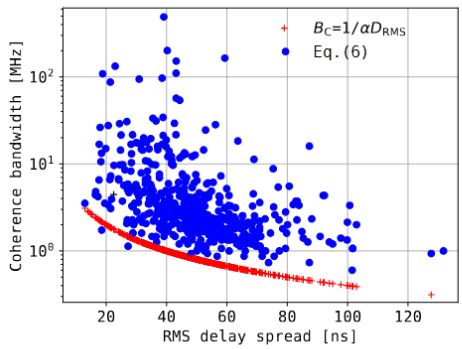

(c) RMS delay spread and coh. BW dependency in LOS positions.

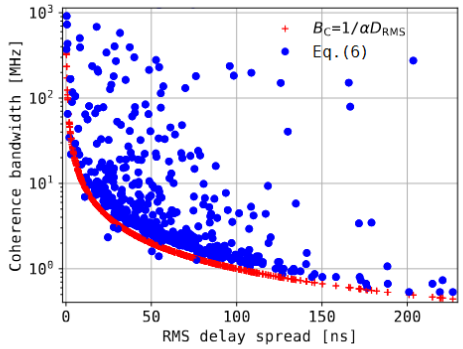

(d) RMS delay spread and coh. BW dependency in NLOS positions.

Figure 38 RMS delay spread and coherence bandwidth under LOS and NLOS conditions.

Comparing the results obtained for the SC and DC scenarios, we do not observe a clear correlation between scatters density and RMS delay spread. In some cases, the RMS delay spread is higher in the DC scenario, while in others the opposite happens. Our intuition is that in some cases a higher clutter density may produce more MPCs, thus the higher delay dispersion. In others, the dense clutter may block the propagating signals,

thus reducing the number of MPCs. We note that in this work we considered 5 bounces (interactions) as the upper limit in our simulations, meaning that a ray is traced up until it interacts five times with the environment before it is either dropped or reaches the RX. Higher number of bounces may produce slightly different results, however, in practical situations the path gain gets below the noise floor after one or two interactions. Our results are in line with other works in the literature. For example, in [**Xin2021**], the RMS delay spread at 140 GHz ranges from 10 ns to 90 ns for LOS and NLOS respectively and in extensive study [**Han2022**], the mean delay spread is around 10 ns, but it can reach up to around 100 ns in specific cases.

Coherence bandwidth

To compute the coherence bandwidth, we define the correlation function $R_{\mathrm{H}}[\Delta f]$ as the Pearson correlation coefficient of the channel transfer function $H[f]$ and a channel transfer function $H[f+\Delta f]$ as

$$R_{\mathrm{H}}[\Delta f] = \frac{E\left[\left(H[f]-\mu_{H[f]}\right)\left(H[f+\Delta f]-\mu_{H[f+\Delta f]}\right)\right]}{\sigma_{H[f+\Delta f]}\sigma_{H[f]}}, \forall \Delta f \in \{0,..,2\ \mathrm{GHz}\}$$

where σ and μ denotes the standard deviation and the mean value of the indexed variables, respectively.

The channel transfer function H[f] has a bandwidth of 2 GHz and the center frequency is set to 300 GHz. By definition, $R_{\mathrm{H}}[\Delta f] = 1$ when $\Delta f = 0$, while $R_{\mathrm{H}}[\Delta f] \leq 1$ when $\Delta f > 0$. The coherence bandwidth is then obtained as:

$$B_{coh} = argmin_{\Delta f>0} \left| R_H[\Delta f] - c \right|,$$

where c is the correlation coefficient. In this work, we consider c=0.7, which is a commonly used value for calculating the coherence bandwidth. In other words, $B_{coh}$is the minimum bandwidth where $R_H[\Delta f] \approx c$. The use of approximation is due to the fact that $R_H[\Delta f]$ is computed for a discrete set of Δf.

A lower bound of the coherence bandwidth can be expressed as a function of the delay spread

$$B_{coh} > \frac{1}{\alpha \cdot D_{RMS}}$$

where α is a proportionality constant. Results for the coherence bandwidth and its lower bound are plotted in Figure 38c (LOS) and Figure 38d (NLOS). The results are shown for SC scenario and both omni-to-directive and omni-to-omni antenna setups. The lower bound is computed assuming $\alpha = 25$ for LOS and $\alpha = 10$ for NLOS.

6 Channel measurements and modeling of RIS in THz bands

This section discusses cascaded RIS channel models, provides initial measurements with 300 GHz RIS prototypes, complemented with ray-tracing-based evaluation of RIS in THz bands.

Cascaded RIS channel model

Figure 39 shows a multiuser MISO downlink communication system featuring a RIS equipped with N reflecting elements, aimed at enhancing communications from an AP with M antennas to a single-antenna user, situated near the RIS.

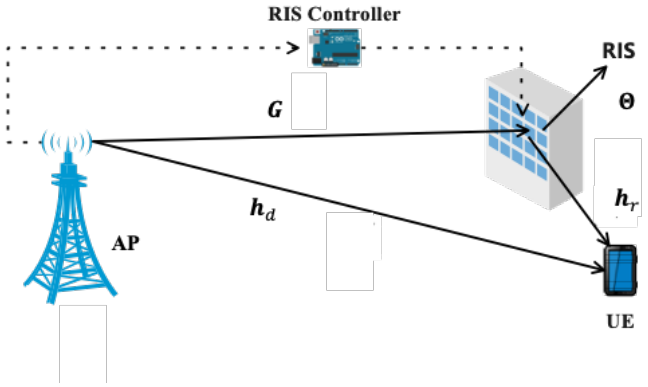

Figure 39 Cascaded channel model.

Because the signal impinges on the RIS and is reflected towards the user, the link between the AP and the RIS is obtained as the cascade of two channels: $\mathbf{G} \in \mathbb{C}^{N \times M}$, which is the baseband equivalent wireless channel between the AP and the RIS, and $\mathbf{h}_r \in \mathbb{C}^{1 \times N}$, the baseband equivalent wireless channel between the RIS and the user. If also the direct link $\mathbf{h}_d \in \mathbb{C}^{1 \times M}$ between the AP and the user is present, the received user's signal can be expressed as

$$y = (\mathbf{h}_r \Theta \mathbf{G} + \mathbf{h}_r)\boldsymbol{x},$$

where Θ denotes the $N \times N$ reflection coefficient matrix and $\boldsymbol{x}$ is the transmitted signal.

The link gains $\boldsymbol{G}, \mathbf{h}_r$ and $\mathbf{h}_d$ follow the propagation model of standard wireless links and can be modelled employing the near-field of far-field channel model depending on the various system parameters. In practice, it is reasonable to assume that the connection between the AP and the RIS is in line-of-sight because both devices are in fixed positions, optimized for improving the system performance, while the nature of the other links depends on the propagation scenario and the user's position.

In general, RIS are passive devices and, accordingly, the coefficient matrix Θ is usually modelled as a diagonal matrix where the main diagonal is a vector of phase offsets. Dimensioning Θ is a very challenging task and it is usually done by solving specific optimization problems, rendered more difficult by the nonconvex constraint that the module of each RIS coefficient is unitary.

By performing an analysis similar to the one proposed in [**Bac2023**], let us analyze the differences in amplitude and phase between the NF and the FF models. A numerical example is reported in Figure *40*, which reports the case of a squared RIS equipped with N = 10,000 radiating elements, located in between a single-antenna BS (and hence M = 1) and a single-antenna UE. To better visualize the scenario, let us focus on the one represented in Figure 41, in which the RIS is located in the XY plane in the origin of the reference system: $\mathbf{r} = (0,0,0)$. The BS and the UE are spaced apart by a distance d_0, and are located symmetrically with respect to the Z axis, such that the BS's coordinates $\mathbf{b}$ and the UE's coordinates $\mathbf{u}$ are as follows: $\mathbf{b} = (-d_0/2,0,\delta)$ and $\mathbf{u} = (+d_0/2,0,\delta)$, where δ is the distance of both the BS and the UE from the RIS on the azimuthal plane, and all entities are located at the same height (otherwise stated, the RIS is not elevated with respect to the UE – we will relax this hypothesis in the remainder of the document).

For our numerical investigation, we consider d_0 = 20m and δ = 4m with respect to the line joining BS and UE. Three frequencies are considered, f_0 = [100,300,1000] GHz, using a spacing across elements equal to $\lambda/2$ and each element's area equal to $(\lambda/4)^2$. For the sake of notation, we define the NLoS link as $\mathbf{g}$, $\mathbf{h}_r\Theta\mathbf{G}$. Amplitude variations between NF and FF models (with each model indicated by the superscript) are reported with dotted lines (using the left axis), whereas phase variations between NF and FF models are represented by the solid lines (using the right axis). While the amplitude variations are negligible, the phase variations are significant, particularly when the carrier frequency increases. This might have an impact, especially when the distance across the devices grows large, thus approaching (or even going beyond) the Fraunhofer distance [**TIMES2023**].

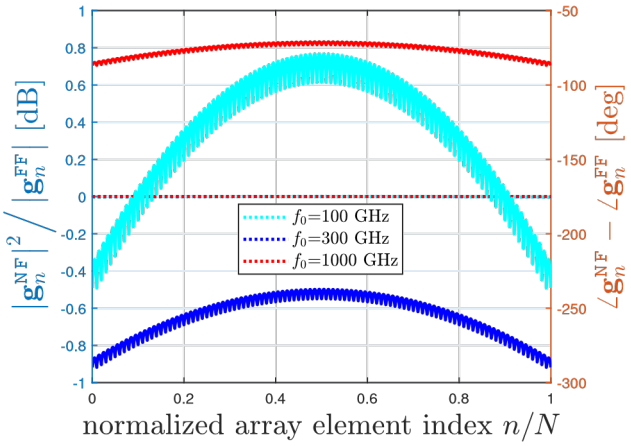

Figure 40 Difference in the amplitude (left axis) and phase (right axis) between the sNF model and the sFF approximation.

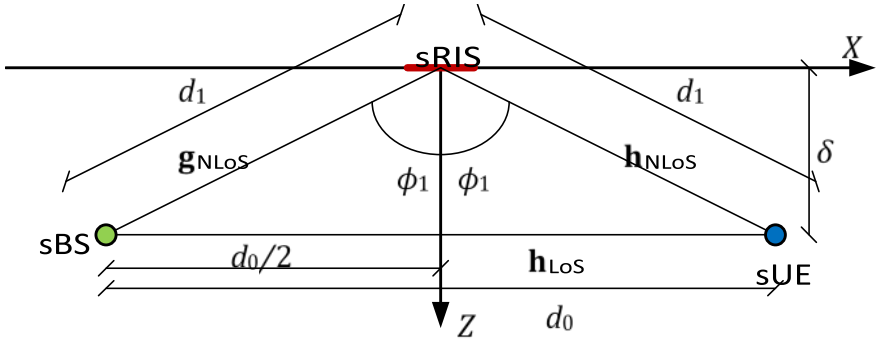

Figure 41 Toy example of sRIS-assisted propagation scenario with symmetric placement of sBS and sUE.

Channel measurements with 300 GHz RISSince the RIS concept is still relatively new, experimentally obtained parameters are essential for developing realistic channel models. This section provides an overview of two measurement campaigns: one conducted with RIS prototypes designed and fabricated within the TIMES project, and another carried out jointly with the TERRAMETA project. The motivation behind the TIMES – TERRAMETA collaboration was to leverage the measurement capabilities of project TIMES and the RIS prototypes developed by TERRAMETA.

Within TIMES WP5, three RIS prototypes were developed: two passive and one active. Comprehensive details of these prototypes can be found in IR5.1 [**TIMES2024**], with the more comprehensive measurements reported in D3.2 [**TIMES2025-2**].

The measurements discussed below were performed with the first passive RIS prototype, which was designed for an incident angle of 0° and a non-specular reflection angle of –30°. This prototype has a diameter of 0.1 m and was fabricated on a silicon wafer. Its operational frequency range extends from 270 GHz to 310 GHz, with optimal performance achieved between 285 GHz and 300 GHz [**TIMES2025-2**, **TIMES2024**].

The TUBS CS used in these measurements, operates in the 300–308 GHz band, with a central frequency near 304 GHz, [**TIMES2023-2**]. Consequently, a frequency mismatch exists between the RIS optimal operational range and the CS measurement band.

Radiation patterns simulated by WP5 are available for incident angles of 0°, –10°, and 10°, at frequencies of both 295 GHz (within the RIS optimal band) and 305 GHz (closer to the CS central frequency), as illustrated in Figure 42. For the purposes of this analysis, comparisons between measurements and simulations are based on the 305 GHz simulation data.

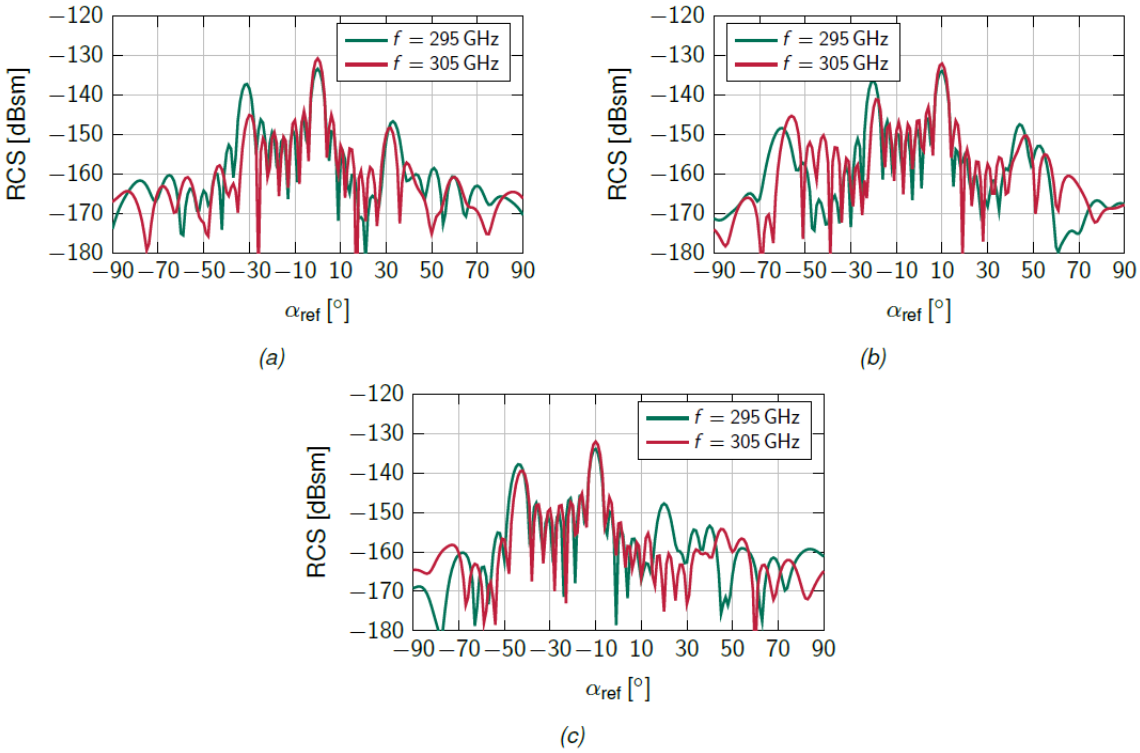

Figure 42 Simulated radiation pattern of the 1st TIMES RIS prototype, provided by WP5: f = 295 GHz and f = 305 GHz: a) $\alpha_{INC} = 0°$; b) $\alpha_{INC} = -10°$, c) $\alpha_{INC} = 10°$

Three passive RIS prototypes were provided by the TERRAMETA project: with 1 bit, 2 bits and 3 bits. Number of bits refers to the phase adjustment capability of the reflected signal and defines the number of possible phase states. The number of phase states is calculated as 2^N, where N is the number of bits. All three RIS prototype patterns are presented in Figure 43. These RISs were designed for an incident angle of 0° and a reflection angle of 30°. It can be observed that the 1 bit RIS exhibits a symmetrical pattern, indicating no difference between reflection angles of 30° and -30°, while the 2 bits RIS shows a 12 dB gain difference between these angles and 3 bits RIS shows a 15 dB gain difference. The difference in gain between the 1 bit and 3 bits RIS, with αREF = 30°, is 4.6 dB. The near–far field boundary of these RIS is 10 m.

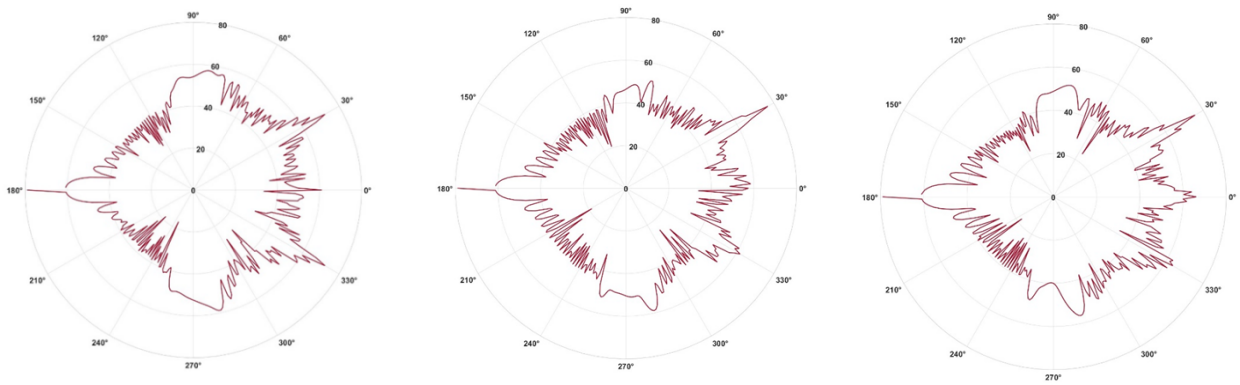

a) b) c)

Figure 43 TERRAMETA RIS prototypes radiation pattern a) 1 bit b) 2 bits c) 3 bits.

Measurement equipment: Measurements were conducted using the TUBS correlation channel sounder, employing high-gain horn antennas with a gain of 26.4 dBi. Detailed description of this equipment was presented in TIMES D3.1 [**TIMES2023-2**].

Measurement environment: Measurements were provided in one of the TUBS lecture rooms (Figure 44). Room has dimensions 13.9 m x 9.5 m.

Figure 44 TUBS lecture room measurement environment.

Measurement scenario: Transmitter (Tx), receiver (Rx) and RIS were fixed on the tripods. Distance between Tx and RIS was fixed, $d_{TX\text{-}RIS}$ = 2.15 m. Distance between Rx and RIS ($d_{RIS\text{-}RX}$) was changed from 0.5 m to 5.5 m. The incident angle (α_{INC}) was fixed at 0°. The reflection angle (α_{REF}) had two values 30° and -30°. Measurements were provided with 1 bit and 3 bits RIS. Setups' parameters presented in Table 1. Schematic view and photo of measurement scenario presented in Figure 45.

Table 17 Measurement setup parameters.

Setup number	RIS	$d_{Tx\text{-}RIS}$, m	$d_{RIS\text{-}Rx}$, m	α_{INC}°	α_{REF}°
1	1 bit	2.15	0.5	0	30
2	1 bit	2.15	0.5	0	-30
3	1 bit	2.15	1	0	30
4	1 bit	2.15	1	0	-30
5	1 bit	2.15	1.5	0	30
6	1 bit	2.15	1.5	0	-30
7	1 bit	2.15	2.15	0	30
8	1 bit	2.15	2.15	0	-30

9	1 bit	2.15	3.5	0	30
10	1 bit	2.15	3.5	0	-30
11	1 bit	2.15	4.5	0	30
12	1 bit	2.15	4.5	0	-30
13	1 bit	2.15	5.5	0	30
14	1 bit	2.15	5.5	0	-30
15	3 bits	2.15	0.5	0	30
16	3 bits	2.15	0.5	0	-30
17	3 bits	2.15	1	0	30
18	3 bits	2.15	1	0	-30
19	3 bits	2.15	1.5	0	30
20	3 bits	2.15	1.5	0	-30
21	3 bits	2.15	2.15	0	30
22	3 bits	2.15	2.15	0	-30
23	3 bits	2.15	3.5	0	30
24	3 bits	2.15	3.5	0	-30
25	3 bits	2.15	4.5	0	30
26	3 bits	2.15	4.5	0	-30
27	3 bits	2.15	5.5	0	30
28	3 bits	2.15	5.5	0	-30

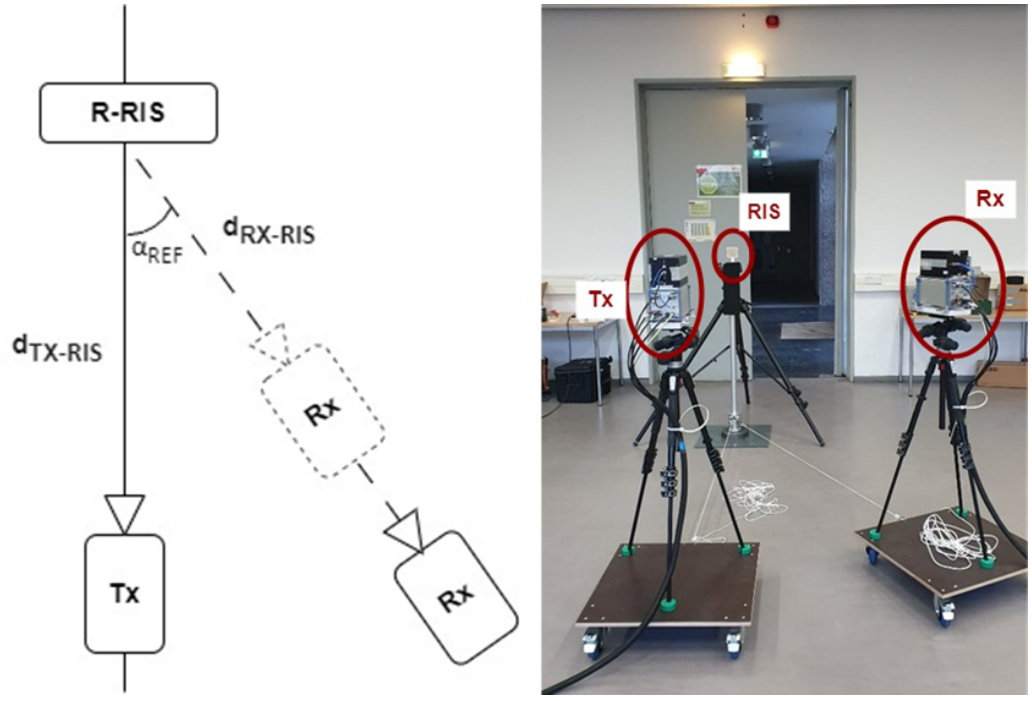

a) b)

Figure 45 Measurement scenario a) schematic view from above b) photo.

Measurements results: The initial measurements step involved evaluating the symmetry of the RIS radiation pattern. Figure 43 presents a comparison of measured path gain (PG) for the link Tx-RIS-Rx at of reflection angles of 30° and -30° for both 1-bit and 3-bit RIS prototypes. For the 1-bit RIS, the measured values at 30° and -30° are nearly identical, within the equipment's measurement uncertainty (±2.8 dB), confirming the symmetry of the radiation pattern and aligning with simulation results. For the 3-bit RIS, simulation results indicated a 15 dB difference between reflection angles of +30° and -30°. The corresponding differences observed in the measurements are summarized in Table 18. Starting from a distance of 1.5 m, noticeable deviations appear between the measured data and the expected values.

Table 18 3bit RIS offset between measured values with reflective angles of 30° and -30°.

d_{RIS-RX}, m	$PL_{30°} - PL_{-30°}$, dB
0.5	-3.0449
1	-4.411
1.5	-6.5321
2.15	-16.793
3.5	-9.3722
4.5	-13.6987
5.5	-10.343

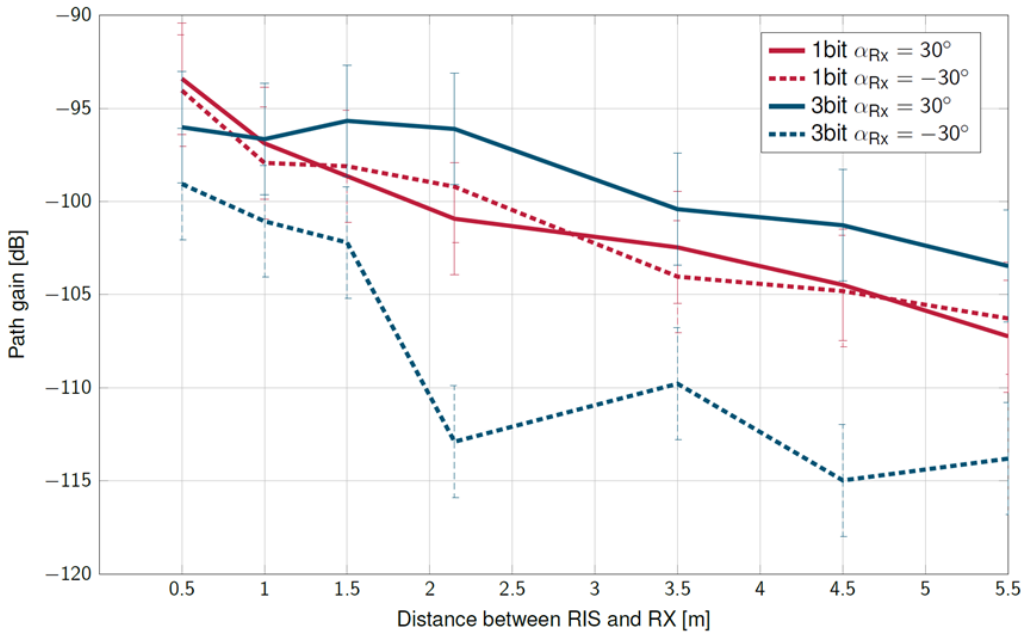

Figure 46: Comparison of measured path gain for link Tx-RIS-Rx for αREF = 30° and αREF = -30°.

There are two possible explanations for this behaviour. The first is that the observed distance corresponds to the “one-third of the near-field” criterion, which defines the transitional region between the reactive and radiative fields. The second explanation is that maintaining precise alignment at short distances is more challenging and requires a specially aligned setup. To determine which explanation is correct, the

measurements with the 3-bit RIS were repeated using an improved setup. This setup included a cross-laser alignment system and a rail mechanism that allowed for changing the distance between the receiver and the RIS without altering the reflection angle (Figure 47). Additionally, measurements were extended up to a distance of 11 meters.

a *b*

Figure 47 Improved measurements setup.

For a more detailed analysis, the next step involved comparing the measured results with values calculated using the radar equation:

$$P_{RX} = \frac{P_{TX} \cdot G_{TX} \cdot G_{RX} \cdot \sigma}{(4\pi)^3 \cdot d_{TX-RIS}^2 \cdot d_{RIS-RX}^2}$$

where P_{RX} – received power; P_{TX} – transmitted power; G_{TX}, G_{RX} – Tx and Rx antennas gain; σ – radar cross section, obtained from RIS simulated radiation pattern; $d_{TX\text{-}RIS}$, $d_{RIS\text{-}RX}$ – distances between Tx and RIS and RIS and Rx respectively.

The PG was calculated by subtracting the transmitted power and antenna gains from the received power. A comparison of the measured and calculated PG values for the 1-bit and 3-bit RIS at a reflection angle α_{REF} = 30° is shown in Figure 48. For the 3-bit RIS, two measurement sets are presented—labeled "1st" and "2nd"—corresponding to the initial setup and the improved alignment setup, respectively.

It can be observed, the improved setup eliminated the pronounced deviation from this constant offset in the region below 1.5 m that was present in the initial 3-bit measurement results. Furthermore, both the 1-bit and 3-bit RIS exhibit an almost constant offset of approximately 5.5 dB from the values predicted by the radar equation.

This offset can be explained by a combination of factors. From a physical perspective, the main contributor is the production offset of the RIS prototype, which was evaluated to be approximately 3 dB based on VNA measurements. From a measurement perspective, additional discrepancies arise due to the error margin of the CS system of ±2.8 dB and potential misalignment errors. These measurement-related uncertainties are difficult to quantify accurately but should be considered when interpreting the results.

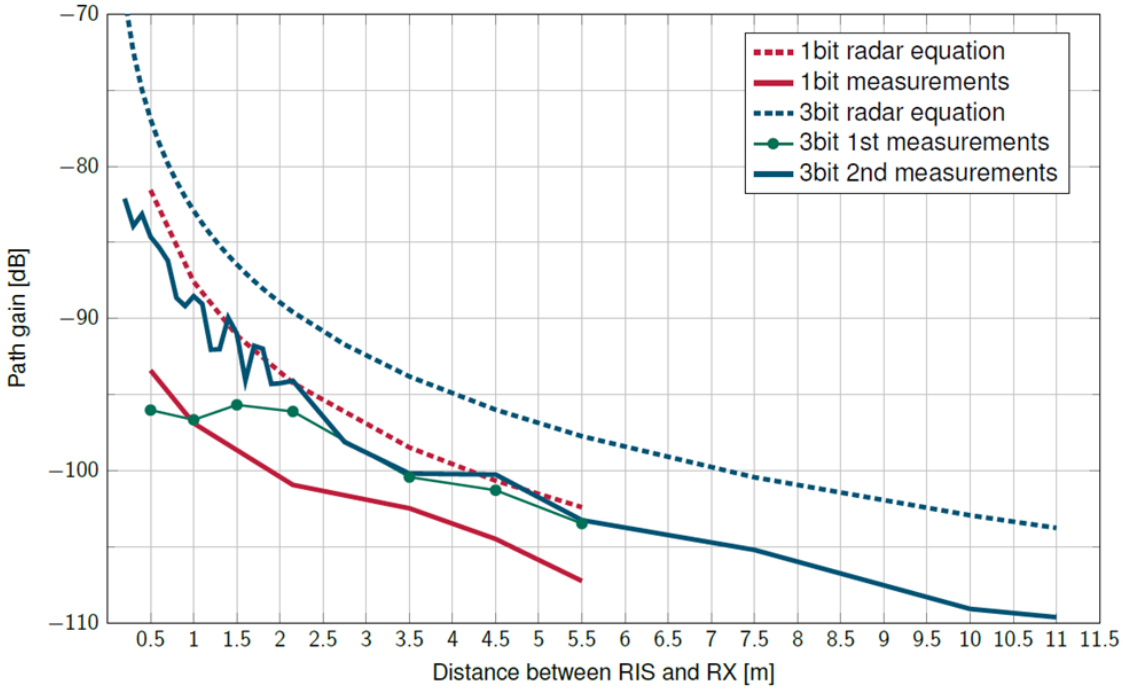

Figure 48 Comparison of Tx-RIS-RX link PG calculated by radar equation and measured data, αREF = 30°.

Figure 49 shows the measurement results for both RIS prototypes, adjusted by a constant offset of 5.5 dB. With this adjustment, the results exhibit good agreement with the radar equation across both near-field and far-field regions. This confirms the applicability of the radar equation even in the near-field region—an important observation, especially considering that the use of THz frequencies, combined with the increasing physical size of RIS structures, shifts the communication almost to the near-field region.

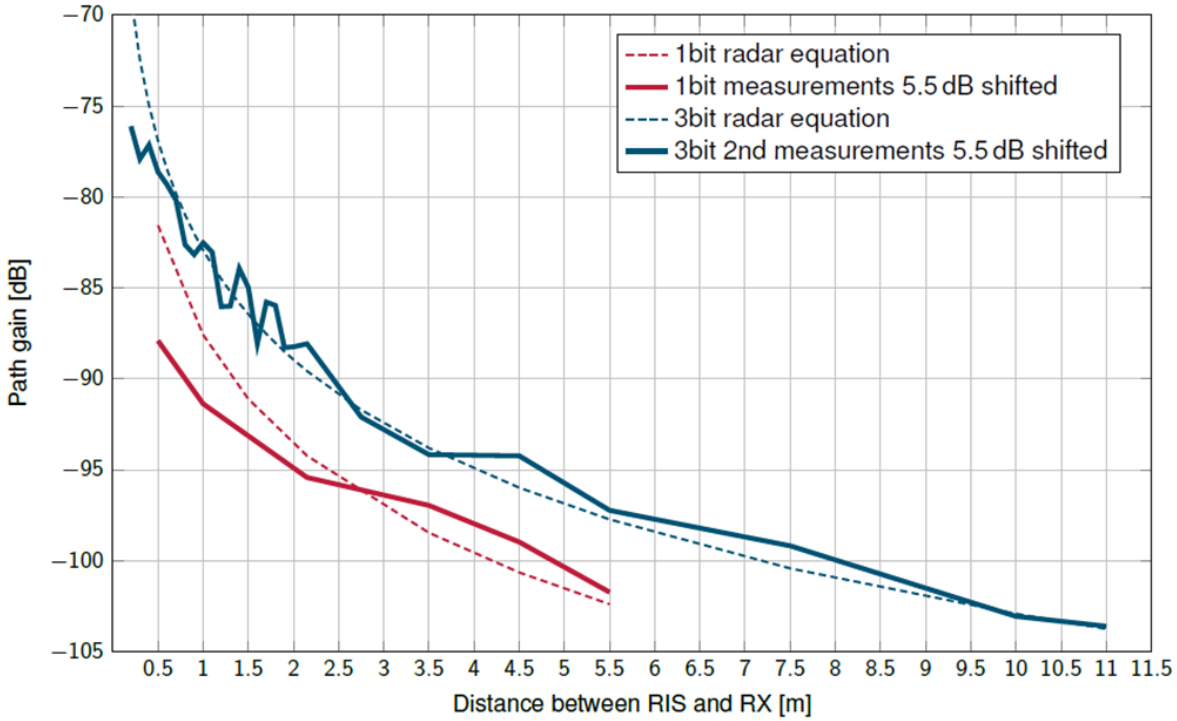

Figure 49 Comparison of measurements results for 1bit RIS and 3bit RIS shifted to constant off-set of 5.5 dB and values calculated with the radar equation.

However, it is still can be observed that conventional radar equation overestimate PG in near-field regions. A possible way to address this limitation was suggested by colleagues from the TERRAMETA project, based on the measurements results presented above [**Loe2025**], [**Ale2024**]. The approach suggests a distance-adaptive radar equation in which the power loss exponents are no longer constant but vary smoothly as functions of the respective link distances. In this approach the TX–RIS and RIS–RX distances are classified into three regimes: near, mid, and far field. These regimes are defined with respect to the Fraunhofer distance (d_{FH}), where the near field corresponds to distances less than d_{FH}, and the boundary between the mid and far field defined as $k \cdot d_{FH}$ where *k* is empirical value derived from the measurements.

The adjusted radar equation includes distance-dependent exponents p_{TX} and p_{RX}, replacing the fixed exponent values typically used. The adjusted bistatic radar equation is given by:

$$P_{RX} = \frac{P_{TX} \cdot G_{TX} \cdot G_{RX} \cdot \sigma}{(4\pi)^3 \cdot d_{TX-RIS}^{p_{TX}} \cdot d_{RIS-RX}^{p_{RX}}}$$

The values p_{TX} and p_{RX} are expressed by weighted interpolation:

$$p_X = w_{1,X} \cdot p_{1,X} + w_{2,X} \cdot p_{2,X}$$

The weight $w_{1,X}$ and $w_{2,X}$ determine how strongly each regime influences the resulting exponent and are computed using logistic functions:

$$w_{1,X} = \frac{1}{1 + e^{-s \cdot (d_X - d_{\mathrm{dash},X})}}$$

where, d_X denotes the relevant distance ($d_{TX\text{-}RIS}$, $d_{RIS\text{-}RX}$) and $d_{dash,X}$ is the transition distance between two adjacent regimes. The parameter s is a logistic function parameter that control the sharpness of transition between the regimes **[Loe2025]**.

Extraction of the large-scale parameters from the RIS-included channel measurements

In the next phase, measurements were conducted using the first RIS prototype developed under the TIMES project [**TIMES2024**]. This prototype was designed for an incident angle (α_{INC}) of 0° and a reflection angle (α_{REF}) of -30°. The measurements aimed to investigate the impact of RIS on channel parameters under various combinations of incident and reflection angles as well as different distances between the RIS and Rx (Figure *50*).

Three incident angle values were used: 0°, +10° and -10°. For each incident angle, reflection angles ranged from –35° to +30° in 5° increments, with the fixed distances: d_{TX-RIS} = 1.3 m and d_{RX-RIS} = 2 m.

In the distance-dependence measurements, the incident angle was fix at 0°, d_{TX-RIS} was 1.3 m, d_{RX-RIS} was varied from 1.5 m to 3 m, in step of 0.5 m, for reflection angles: -35°, -30°, -25°, and +30°.

Each setup (position) was measured in three variants: 1) with the RIS prototype; 2) with a metal plate of the same size and shape, positioned identically to the RIS; 3) without the RIS or metal plate.
Detailed description of measurements scenarios and results are presented in [**TIMES2025-2**].

Based on the angle combination measurements, the following parameters were extracted: 1) relative PG (ΔPG), quantifies the difference in PG values between the setups with and without the RIS, Table *19*; 2) root mean square (rms) delay spread (DS); 3) rms DS excluding the main component (Tx – RIS – Rx path), referred to here as excluding rms DS, Table 20 – Table 22.

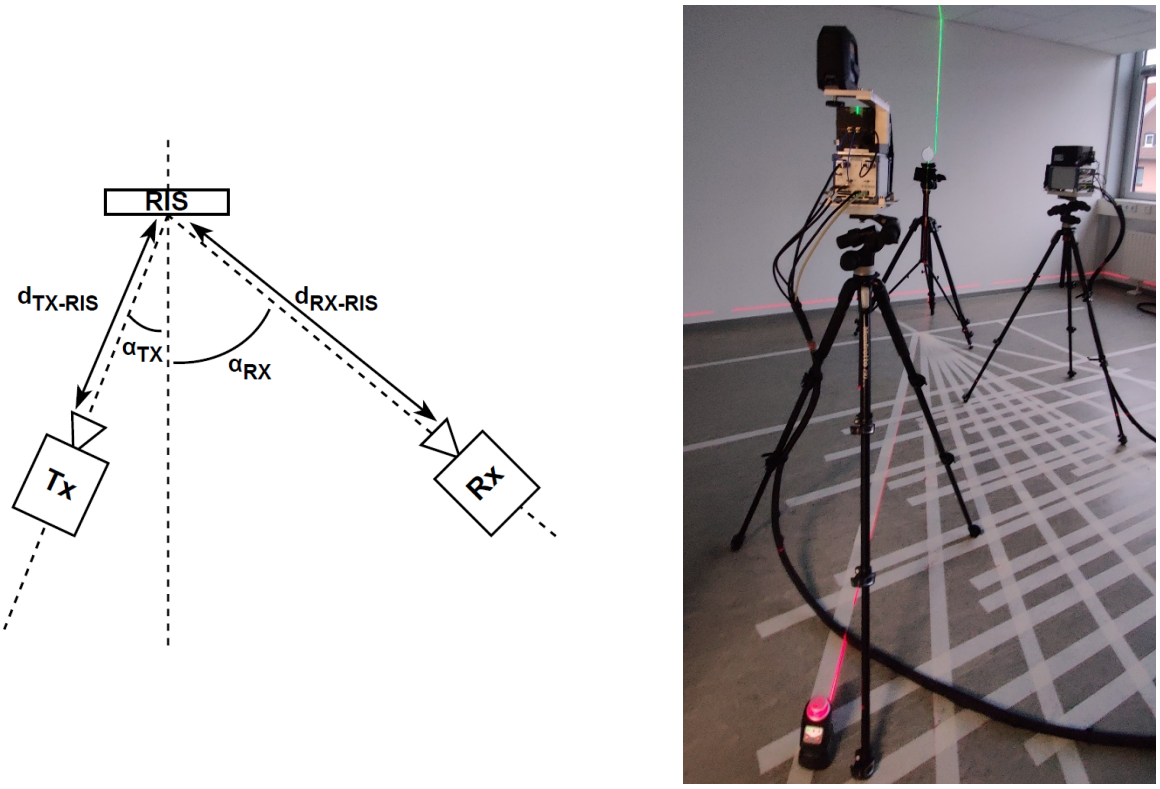

a b

Figure 50 Investigation of RIS influence on the channel parameters with different αINC, αREF combinations: a) schematic view; b) photo of setup.

Table 19 Relative PG values.

α_{INC}°	α_{REF}°	ΔPG, dB	α_{INC}°	α_{REF}°	ΔPG, dB	α_{INC}°	α_{REF}°	ΔPG, dB
0	-35	41.2	-10	-35	7.9	10	-35	7.3
0	-30	31.7	-10	-30	0.6	10	-30	7.6
0	-25	13	-10	-25	29.8	10	-25	18.8
0	-20	8	-10	-20	27.5	10	-20	-1
0	-15	-0.1	-10	-15	10.4	10	-15	16.8
0	-10	2.9	-10	-5	11.2	10	-10	59.5
0	-5	10	-10	0	13.3	10	-5	26.7
0	30	34.6	-10	10	47.8	10	0	13.9
0	10	7.7						

Table 20 Values of the rms DS and excluding rms DS, αINC = 0°.

α_{REF}°	DS with RIS, ns	excl.DS with RIS, ns	DS without RIS, ns	excl. DS without RIS, ns
-35	0.81	25.01	6.42	6.77
-30	1.07	12.4	3.96	3.58
-25	2.76	7.2	3.33	4.27
-20	7.57	7.86	3.86	3.78

-15	13.28	16.85	14.73	16.05
-10	1.46	1.34	1.37	1.27
-5	3.41	4.38	2.28	2.64
10	3.09	3.09	5.71	5.71
30	0.93	10.67	6.98	7.25

Table 21 Values of the rms DS and excluding rms DS, αINC = -10°.

α_{REF}°	DS with RIS, ns	excl.DS with RIS, ns	DS without RIS, ns	excl. DS without RIS, ns
-35	12.03	14.61	3.22	2.29
-30	5.46	5.63	4.23	3.97
-25	1.14	24.75	3.29	2.68
-20	0.6	13.55	4.98	5.12
-15	1.76	4.26	3.67	3.3
-5	11.2	3.45	2.49	2.02
0	13.3	3.98	1.72	1.58
10	1.53	2.51	0.6	0.59

Table 22 Values of the rms DS and excluding rms DS, αINC = 10°.

α_{REF}°	DS with RIS, ns	excl.DS with RIS, ns	DS without RIS, ns	excl. DS without RIS, ns
-35	5.27	9.46	4.09	3.84
-30	1.38	0.76	0.96	0.39
-25	1.8	0.89	0.79	0.71
-20	6.14	8.32	4.22	3.94
-15	1.97	2.22	1.62	1.37
-10	1.57	0.95	0.5	0.5
-5	2.41	3.48	0.57	0.55
0	2.41	2.76	1.61	1.56

During the distance-depended measurements d_{TX-RIS} was fixed at 1.3 m, while the d_{RX-RIS} was varied from 1.5 m to 3 m in step of 0.5 m. Measurements were conducted for the following angle combinations: α_{INC} = 0° and α_{REF} = -35°; α_{INC} = 0° and α_{REF} = -30°; α_{INC} = 0° and α_{REF} = 30°.

From these measurements RIS RCS values were extracted using the radar equation These extracted RCS values are necessary for calibrating the RIS radiation pattern, which will be used in ray tracing simulations. The results are presented in Figure *51*.

The highest RCS values were obtained for the angle combinations of 0° incidence and -35° reflection, even though the designed reflection angle was -30°. The variation in RCS values with distance does not exceed ±2.5 dBsm, which is within the measurement equipments margin of error. The mean RCS values are 3.8 dBsm for α_{REF} = -35°, 0.45 dBsm for α_{REF} = -30° and 0.9 dBsm for α_{REF} = 30°.

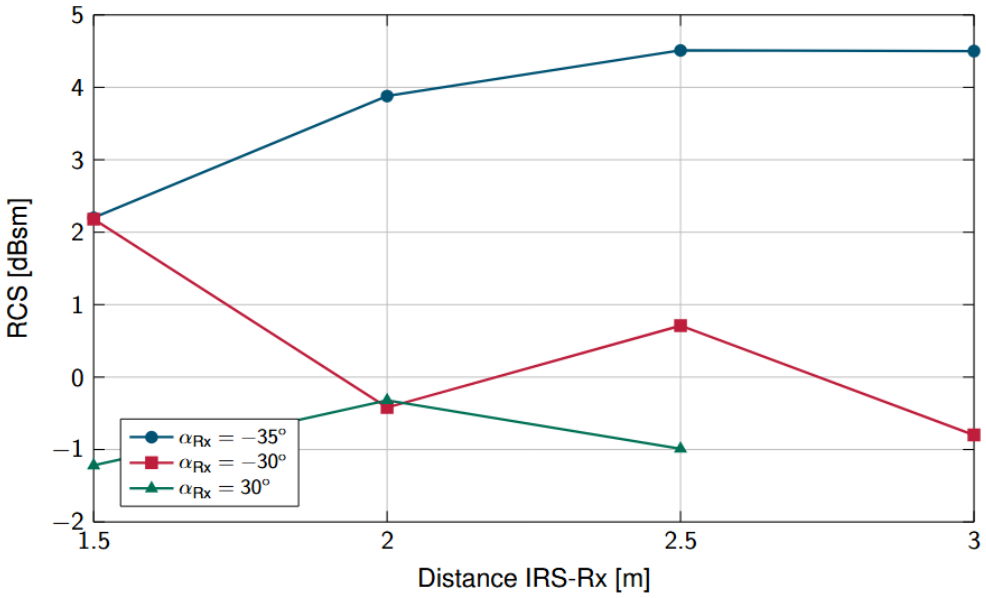

Figure 51 RCS value dependence from distance between RIS and Rx.

To investigate the influence of the RIS on the power angular profile (PAP), “omni-directional” azimuth scanning measurements were conducted in an industrial environment. The measurements included two setups with different Tx and Rx positions, as shown in Figure 52. Each setup was measured both with and without the RIS. Measurements were taken using an azimuth angle step of 10°. Detailed description of measurements and results presented in TIMES D3.2 [**TIMES2025-2**].

Based on characterization measurements, which showed symmetry in the reflected beam at 30° and -30°, the Rx in Setup 1 was positioned to capture the main Tx-RIS-Rx peak at an incident angle of 0° and a reflection angle of -30°. In Setup 2, the Rx was positioned to capture the main peak at 0° incident angle and 30° reflection angle.

Scenario 2 was also measured using the TERRAMETA Project 1-bit RIS (described in the previous section) as part of a joint measurement campaign. This allows for a comparison of the impact of two different RIS configurations on both the PAP and angular spread (AS).

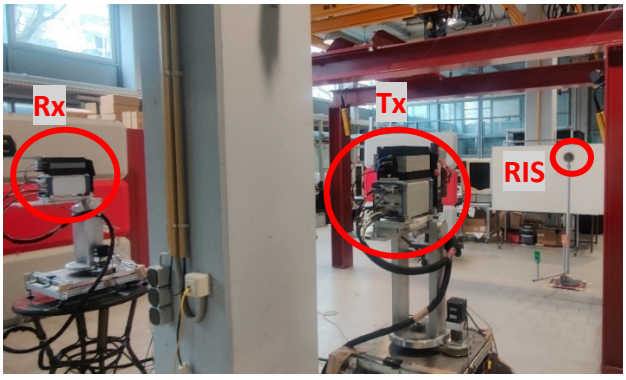

a

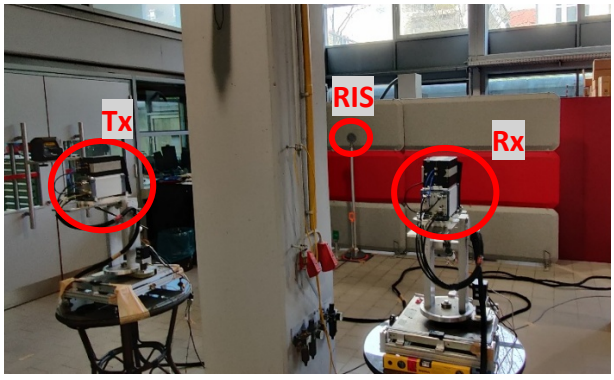

b

Figure 52 "Omni-directional" RIS assisted channel measurements in an industrial environment: a) Setup 1; b) Setup 2.

The normalized PAP for all three setups is presented in Figure *53*. The angular spread (AS) values for both AoD and AoA are shown in Table *23* and Table *24*.

In Setup 1, clear TIMES RIS peak is observed at 0° AoD and 30°, corresponding to a -30° reflection angle for the RIS. It can be observed that, in the absence of the RIS, the channel exhibits more multipath components arriving from a wider range of directions, resulting in higher AS values for both AoD and AoA. This can be attributed to the RIS ability to focus energy in a specific direction, thereby reducing the number and intensity of other angular components. As a result, the angular profile becomes more concentrated, leading to a reduced AS.

In Setup 2, RIS peak was expected at the combination of 0° AoD and 330° AoA, corresponding to a 30° reflection angle. However, the TIMES RIS peak is weak, possibly due to alignment issues. As shown in the characterization measurements [**TIMES-D3.2**], the maximum reflection does not occur exactly at 30°, but is instead shifted slightly, occurring between 30° and 35°. In contrast, the same setup measured with the TERRAMETA RIS shows a clear peak at the expected angle combination, Figure *53*e. In this setup, the AS is observed to be higher with both RIS configurations than without. This can possibly be explained by additional scattering components introduced by the RIS, which are noticeable at angle combinations around an AoD values of 10° and 20° and AoA values of 340° and 350°.

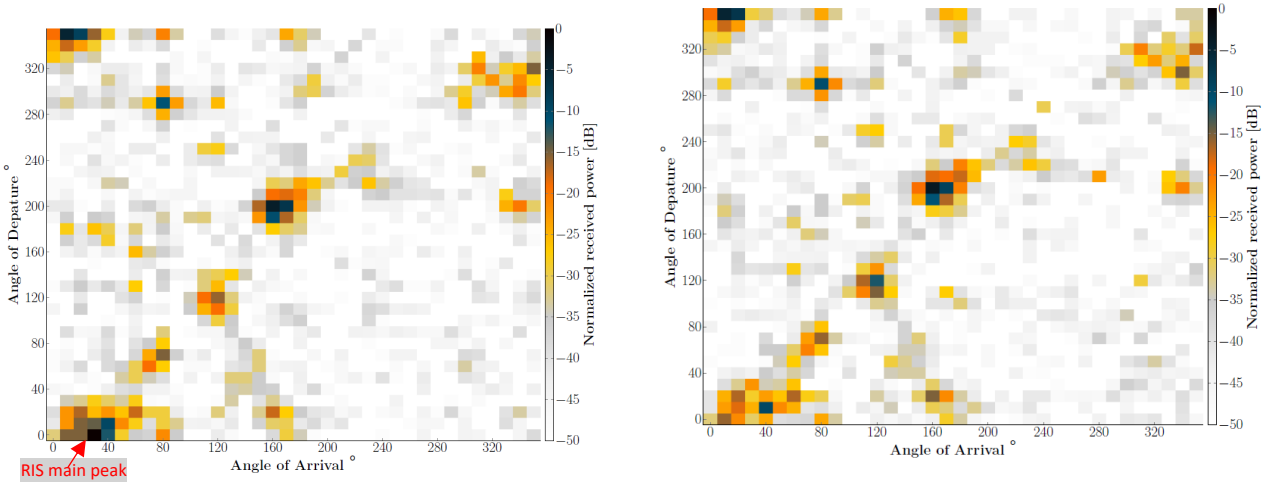

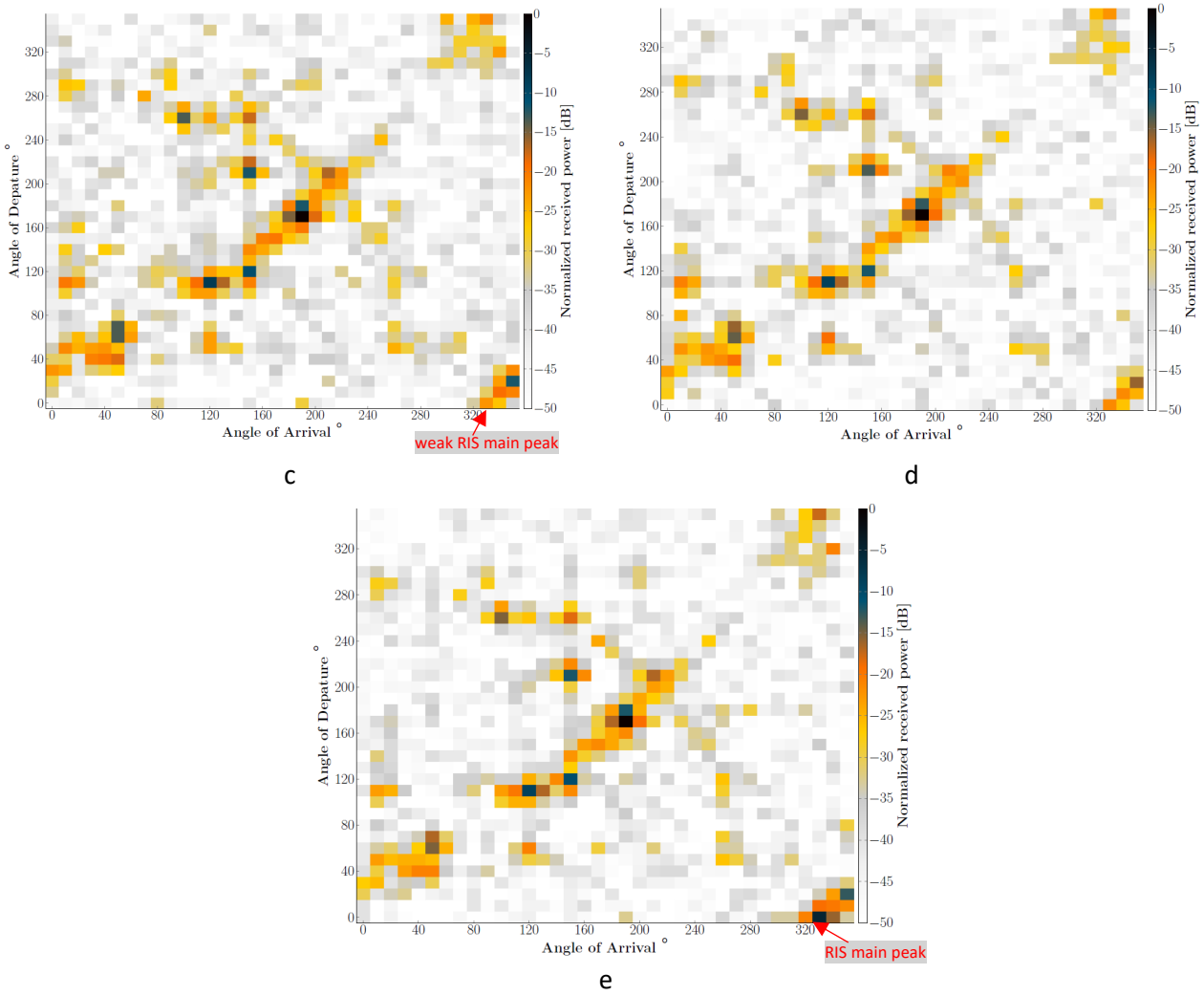

Figure 53 Measured normalized PAP with and without RIS: a) with TIMES 1st prototype RIS, setup 1; b) without RIS, setup 1; c) with TIMES 1st prototype RIS, setup 2; d) without RIS, setup 2; e) with TERRAMETA 1bit RIS, setup 3.

Table 23 AoD values for measured setups.

	AS AoD°, with TIMES RIS	AS AoD°, with TERRAMETA RIS	AS AoD°, without RIS
Setup 1	52.2	-	56.6
Setup 2	44.2	52.5	42.9

Table 24 AS AoA values for measured setups.

	AS AoA°, with TIMES RIS	AS AoA°, with TERRAMETA RIS	AS AoA°, without RIS
Setup 1	49.2	-	53.5
Setup 2	45.1	52.6	43.8

Ray tracing for RIS-assisted channels

The main purpose of integrating RIS into a wireless communication system is to enable connectivity in scenarios where a direct link between the Tx and Rx is unavailable or where the LOS component is too weak to ensure reliable communication. Therefore, one of the key steps in evaluating RIS-assisted channels is to assess the potential PG improvement introduced by the RIS. This improvement can be quantified by comparing the direct Tx–Rx path with the RIS-assisted Tx–RIS–Rx path under different RIS angle configurations and various environmental conditions.

Experimental investigation of such effects through measurements is inherently limited due to the time and effort required. Ray tracing offers a promising alternative, as it enables simultaneous prediction of both the direct and RIS-assisted propagation paths with high accuracy. Additionally, ray tracing provides flexibility in adapting simulations to specific environments by incorporating a 3D model of the scene and implementing the radiation patterns of both Tx and Rx antennas. This is especially important for communication in the low-THz frequency range, where high-gain directional antennas are typically used, and their radiation patterns significantly influence the channel characteristics.

The following section presents the ray tracing simulation setup, which is based on the end-to-end Tx–RIS–Rx measurement scenario in an empty room, previously introduced and described in detail in TIMES Deliverable D3.2 [**TIMES2025-2**].

Implementation of RIS in the SiMoNe Ray Tracing Tool

The ray tracing simulations described in this section were conducted using the SiMoNe framework, developed at TU Braunschweig. SiMoNe is designed for integrated simulations that combine ray-based propagation modeling with link- and system-level analysis. The tool is described in detail in TIMES Deliverable D2.2 [**TIMES2023-4**].

In SiMoNe, RIS-assisted communication is implemented by decomposing the scenario into two independent ray tracing tasks: one from the Tx to the RIS, and another from the RIS to the Rx. Instead of modeling the RIS as a complex non-specular surface within the ray tracer, it is treated as an intermediate node. The incoming and outgoing rays are then combined in a postprocessing step using a flexible mathematical model.

This implementation assumes far-field operation, where the RIS surface is uniformly illuminated by the Tx. If this assumption does not hold—such as in the case of large RIS surfaces or near-field conditions—additional postprocessing techniques, like surface rasterization, may be applied to ensure accurate modeling.

RIS functionality, such as beam steering, is incorporated during the postprocessing stage using codebooks or gain patterns that are functions of both the AoA and AoD. To enhance computational efficiency and reduce memory usage, insignificant paths can be filtered out at this stage [**Her2025**].

A complete description of the RIS implementation in the SiMoNe ray tracing tool, including the integration of RIS radiation patterns, will be provided in TIMES Deliverable D4.4.

Verification of the SiMoNe Ray Tracing Tool for RIS-Assisted Channels

As described in TIMES Report IR5.1 [**TIMES2024**], three RIS prototypes were developed within the framework of TIMES Work Package 5: two passive and one active.

The 3D model of the simulated environment is shown in **Error! Reference source not found.**. The room dimensions are 6 m × 6.6 m × 2.5 m. The radiation pattern of the first RIS prototype, simulated for an incident angle of 0° and frequency of 305 GHz, that aligned with the measurement equipment central frequency [**TIMES2025-2**], was provided by TIMES Work Package 5, **Error! Reference source not found.**.

According to this simulated radiation pattern, the designed non-specular RIS reflection occurs at an angle of –30.4°, with a radar cross section (RCS) of –87.3 dBsm. The specular reflection peak is located at a reflection angle of 0°, with an RCS of –72 dB. However, as demonstrated in the previous section, the measurement results indicate that the maximum non-specular reflection occurs at –35°, with an RCS of 3.8 dBsm. For the angle combination closest to the expected maximum: –30° reflection and 0° incidence, the average RCS was measured to be 0.45 dBsm.

The unrealistically low RCS values in the simulated pattern are attributed to software limitations, highlighting the need to adjust the radiation pattern before its use in the simulations. This adjustment was performed by setting the designed RIS non-specular reflection angle combination to the 0 dBsm. This method was chosen because the designed RIS non-specular reflection is expected to occur at a reflection angle of –30.4° with an incidence angle of 0°. The closest available measurement combination, -30° reflection and 0° incidence, yielded an average RCS of 0.45 dBsm. The adjusted radiation pattern shown in **Error! Reference source not found.**.

However, it should be noted that this adjustment does not provide accurate absolute amplitude values, as precise adjustment would require characterization measurements of the radiation pattern, which are not feasible with the CS system. Therefore, the analysis focuses primarily on comparing the angular behaviour of the amplitudes rather than their absolute values.

The ray tracing simulations were conducted using high-gain directional antennas with a half-power beamwidth (HPBW) of 8°, as specified in TIMES Deliverable D3.2 [**TIMES2025-2**].

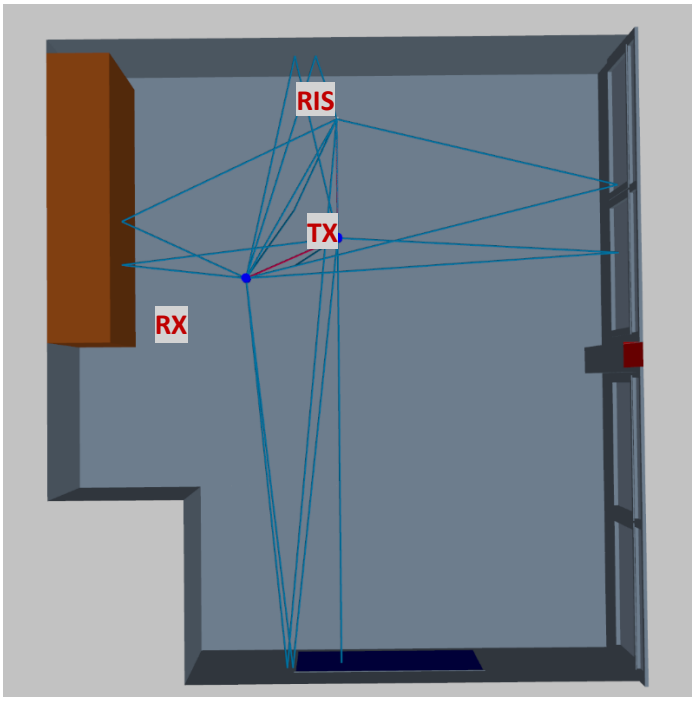

Figure 54 Ray tracing scenario

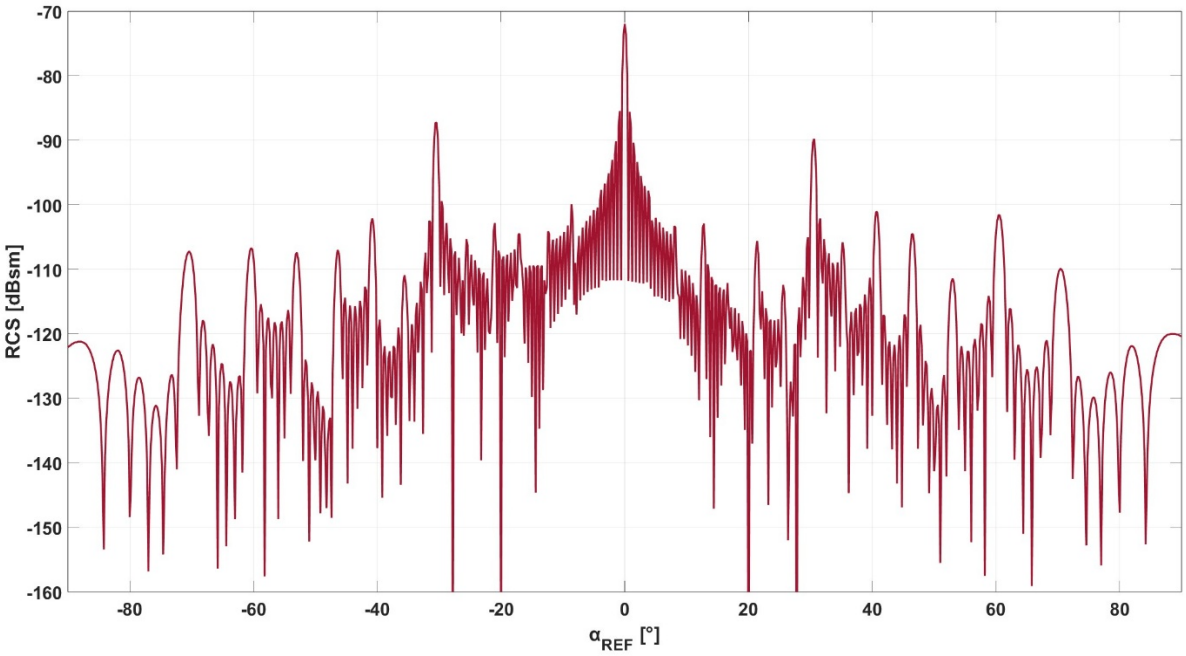

Figure 55 Radiation pattern of the first TIMES RIS prototype, incident angle 0°, f=305 GHz

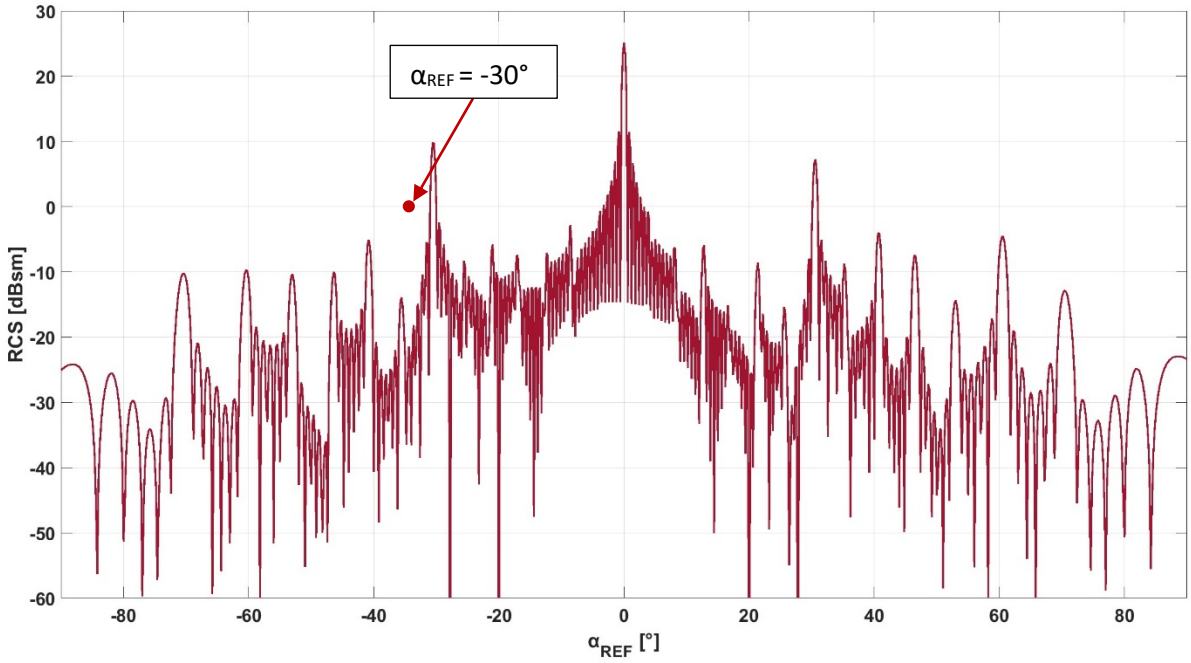

Figure 56 Adjusted radiation pattern of the first TIMES RIS prototype, incident angle 0°, f=305 GHz

It is important to note that the PG values reported here, both for measurements and ray tracing, include the antenna gains. This approach is used because the direct Tx – Rx path falls within the side lobes of the antenna patterns, making it more appropriate to compare the measured and simulated results without removing the

antenna effects. Therefore, the reported PG corresponds to the total radio channel PG, including antenna influence.

Measurements and simulation results of PG values of Tx – RIS – Rx path for the various reflection angle in case of 0° incidence angle, d_{TX-RIS} = 1.3 m, d_{RIS-RX} = 2 m provided in **Error! Reference source not found.**. The same comparison was made for the measurement and ray tracing results in case of fixed reflection angles: -35°, -30° and -25° in case of various distances between the RIS and Rx**Error! Reference source not found.**.

Table 25 Measured and ray tracing PG values, dTX-RIS = 1.3 m, dRIS-RX = 2 m, αINC = 0°

α_{REF}°	PG_{MEAS}, dB	PG_{RT}, dB	$PG_{RT} - PG_{MEAS}$, dB
-35	-46.4	-71.53	-25.13
-30	-51.6	-48.73	2.87
-25	-65.6	-62.73	2.87
-20	-81.9	-88.53	-6.63
-15	-75.3	-80.83	-5.53
-10	-77.1	-59.03	18.07
-5	-55	-52.53	2.47
10	-74.6	-65.03	9.57
30	-50.4	-53.03	-2.63

Table 26 Measured and ray tracing PG values, dTX-RIS = 1.3 m, αREF = -35°, αINC = 0°

d_{RIS-RX}, m	PG_{MEAS}, dB	PG_{RT}, dB	$PG_{RT} - PG_{MEAS}$, dB
1.5	-45.6	-69.13	-23.53
2	-46.4	-71.53	-25.13
2.5	-48.6	-73.53	-24.93
3	-52.1	-75.13	-23.03

Table 27 Measured and ray tracing PG values, dTX-RIS = 1.3 m, αREF = -30°, αINC = 0°

d_{RIS-RX}, m	PG_{MEAS}, dB	PG_{RT}, dB	$PG_{RT} - PG_{MEAS}$, dB
1.5	-46.3	-46.23	0.07
2	-51.6	-48.73	2.87
2.5	-50.6	-50.63	-0.03
3	-54	-52.23	1.77

Table 28 Measured and ray tracing PG values, dTX-RIS = 1.3 m, αREF = -25°, αINC = 0°

d_{RIS-RX}, m	PG_{MEAS}, dB	PG_{RT}, dB	$PG_{RT} - PG_{MEAS}$, dB
1.5	-64.5	-60.13	4.37
2	-65.6	-62.73	2.87
2.5	-72.4	-64.63	7.77
3	-75.3	-66.23	9.07

It can be observed from Table 25 - Table 28 that the largest discrepancies between the measured results and the adjusted ray tracing simulation results occur at reflection angles of –35°, –10°, and 10°, with differences of –25.13 dB, 18.07 dB, and 9.57 dB, respectively. The deviation at –35° can be attributed to the fact that the measured maximum non-specular reflection was found at –35°, whereas the simulated pattern predicts a higher PG at –30.4° This explains the large discrepancy in the Table 26.The differences at –10° and 10° can be explained by the very narrow RIS radiation RIS pattern, where even a 0.5° step can cause significant RCS variations. All other data points exhibit an approximately constant offset of less than 7 dB between measurements and simulations. This offset can be attributed to several factors. First, the maximum RCS observed in the measurements occurred at –35°, differing from the predicted –30° maximum in the radiation pattern. Additionally, the adjustment of the simulated results was performed using the closest available measurement angle combination rather than the exact predicted angle, due to the limited angular resolution achievable with the CS measurement system. Finally, the measurement equipment itself has an inherent error margin of ±2.8 dB.

In the next step, the PG values of the direct Tx–Rx path were compared between measurements and ray tracing simulations. This comparison serves two purposes: first, to evaluate the PG improvement achieved by introducing the RIS-assisted channel, and second, to further verify the correctness of the antenna pattern implementation in the ray tracing tool, particularly since the direct path lies within the side lobes of the antennas.

However, due to the physical dimensions of the CS units, it is not feasible to accurately perform this comparison for RIS–Rx distances greater than 1.5 m in the current measurement setup. At larger distances, the Tx and Rx units obstruct the antenna side lobes with their own bodies. For the same reason, accurate comparisons are also not possible at small reflection angles.

The comparison results for three reflection angles (–35°, –30°, and –25°), under the conditions of 0° incidence angle, a Tx–RIS distance of 1.3 m, and a RIS–Rx distance of 1.5 m, are presented in Table 29**Error! Reference source not found.**. As expected, the results show a good match between the measurements and ray tracing simulations. This validates the simulation approach and makes it feasible to extend the prediction of direct Tx–Rx PG values to setups where such measurements were not possible due to physical limitations of the measurement system.

Table 29 Measured and ray tracing PG values of direct Tx-Rx path, dTX-RIS = 1.3 m, dRIS-RX = 1.5 m, αINC = 0°

α_{REF}°	PG_{MEAS}, dB	PG_{RT}, dB
-35	-101.5	-94.2
-30	-93.6	-94.6
-25	-99.7	-95.8

Table 30presents the results of PG improvement achieved using the Tx–RIS–Rx path, for both measurements and ray tracing, under the specified scenario. A mismatch exists only at –35°, for reasons explained above. For –30° and –25°, the PG improvement values from simulations and measurements differ by approx. 1 dB.

Table 30 Measured and ray tracing PG improvement values achieved by using RIS-assisted channel

α_{REF}°	Meas. PG_{LOS} - PG_{RIS}, dB	RT. PG_{LOS} - PG_{RIS}, dB
-35	-55.9	25.07

-30	-47.3	48.37
-25	-35.2	35.67

The presented ray tracing approach based on TUBS SiMoNe framework, validated against measurement results, serves as a solid foundation for the prediction and analysis of RIS-assisted channels. By decomposing the Tx–RIS–Rx path into two segments and integrating RIS functionality through postprocessing, the simulation framework offers flexibility and practical applicability for various environments. The comparison with measurements confirms the general reliability of the method, particularly for estimating power gain improvements and analysing the impact of different RIS configurations. However, the accuracy of the results strongly depends on the quality of input data, especially the validity of the RIS radiation pattern. Overall, with the proper input data, the provided ray tracing method provides an efficient and scalable tool for supporting the design and deployment of RIS-assisted communication systems.

7 Conclusions

This deliverable has provided a detailed analysis and extension of channel models applicable to industrial environments operating at sub-THz frequencies. Through the integration of theoretical modeling, empirical measurements, and machine learning, this deliverable contributes to THz channel characterization in industrial settings in the following key directions:

- Accurate modeling at sub-THz frequencies, including near-field and RIS-specific effects, and ISAC, which are not covered in traditional models.
- Ray-tracing tools, calibrated with real-world measurements, providing high-fidelity predictions that are essential for validating simulation-based models.
- Machine learning methods that significantly enhance model flexibility, thus enabling adaptive THz channel reconstruction in complex industrial layouts.
- The extended models and extracted parameters (e.g., PLE, shadowing, clustering) developed within TIMES and captured in this deliverable, which are consistent across frequency bands.

These results provide a solid foundation for continued standardization and deployment of THz communication systems in industrial applications, thus contributing to the inclusion of THz into the next generation industrial communications systems.

8 References

[**3GPP2018**] 3GPP TR 38.901, "Study on channel model for frequencies from 0.5 to 100 GHz," 2018.

[**Ale2024**] George C. Alexandropoulos, Bo Kum Jung, Panagiotis Gavriilidis, Sérgio Matos, Lorenz H. W. Loeser, Varvara Elesina, Antonio Clemente, Raffaele D'Errico, Luís M. Pessoa, Thomas Kürner "Characterization of Indoor RIS-Assisted Channels at 304 GHz: Experimental Measurements, Challenges, and Future Directions", arXiv:2412.07359, https://doi.org/10.48550/arXiv.2412.07359

[**Bac2023**] Giacomo Bacci, Luca Sanguinetti, and Emil Björnson. Spherical wavefronts improve MU-MIMO spectral efficiency when using electrically large arrays. IEEE Wireless Communications Letters, 2023.

[**Bak2024**] S. Bakirtzis, C. Yapar, K. Qui, I. Wassell, and J. Zhang, "Indoor radio map dataset," IEEE Dataport, 2024, https://dx.doi.org/10.21227/c0ec-cw74

[**Bak2025**] Stefanos Bakirtzis, Çağkan Yapar, Kehai Qiu, Ian Wassell, Jie Zhang, "The First Indoor Pathloss Radio Map Prediction Challenge", 2025 IEEE International Conference on Acoustics, Speech and Signal Processing - ICASSP 2025, Hyderabad, India.

[**Bal2005**] Constantine A Balanis. *Antenna theory: analysis and design*. Wiley-Interscience, 2005.

[**Bjo2020**] Emil Björnson and Luca Sanguinetti. Power scaling laws and near-field behaviors of massive mimo and intelligent reflecting surfaces. *IEEE Open Journal of the Communications Society*, 1:1306–1324, 2020.

[Bjo2021] E. Bjornson, O. T. Demir, and L. Sanguinetti, "A primer on near-field beamforming for arrays and reconfigurable intelligent surfaces," CoRR, vol. abs/2110.06661, 2021.

[Bre2001] L. Breiman, "Random Forests," in Machine Learning, 2001.

[**Cha2022**] Christina Chaccour, Mehdi Naderi Soorki, Walid Saad, Mehdi Bennis, Petar Popovski, and Mérouane Debbah, "Seven Defining Features of Terahertz (THz) Wireless Systems: A Fellowship of Communication and Sensing", IEEE Communications Surveys and Tutorials, Vol. 24, No. 2, 2022.

[Cho2018] Han, Chong and Chen, Yi, "Propagation Modeling for Wireless Communications in the Terahertz Band," IEEE Communications Magazine, vol. 56, no. 6, pp. 96–101, 2018

[**Code**] https://www.tu-braunschweig.de/fileadmin/Redaktionsgruppen/Institute_Fakultaet_5/IFN/forschung/abt_mobilfunksysteme/channel_model_tu-bs.zip

[Czi2006] Czink, Nicolai, Pierluigi Cera, Jari Salo, Ernst Bonek, Jukka-Pekka Nuutinen, and Juha Ylitalo. "A framework for automatic clustering of parametric MIMO channel data including path powers." In IEEE Vehicular Technology Conference, pp. 1-5. IEEE, 2006

[**Deh2023**] Saeid K. Dehkordi et al. Multi-static Parameter Estimation in the Near/Far Field Beam Space for Integrated Sensing and Communication Applications. 2023. arXiv: 2309.14778[eess.SP].

[**Do2023**] Heedong Do, Namyoon Lee, and Angel Lozano. Parabolic wavefront model for line-of-sight mimo channels. IEEE Transactions on Wireless Communications, 2023.

[**Fan2019**] Jiancun Fan and Ahsan Saleem Awan, Non-Line-of-Sight Identification Based on Unsupervised Machine Learning in Ultra Wideband Systems", IEEE Access, vol. 7, pp. 32464-32471, 2019, doi: 10.1109/ACCESS.2019.2903236.

[**Fri2016**] Fricke, A.; Rey, S.; Peng, B.; Kürner, T.; et al.: TG3d Channel Modelling Document (CMD). IEEE 802.15 Document 15-14-0310-19-003d, electronic publication (61 pages), Macau, China, March 2016.

[**Fri2019**] Benjamin Friedlander. "Localization of Signals in the Near-Field of an Antenna Array". In: IEEE Transactions on Signal Processing 67.15 (2019), pp. 3885–3893. doi: 10.1109/TSP.2019.2923164.

[Fus2015] F. Fuschini, E. M. Vitucci, G. Falciasecca, M. Barbiroli, and V. Degli Esposti, "Ray tracing propagation modeling for future small-cell and indoor applications: A review of current techniques," Radio Science, 2015.

[**Han2022**] C. Han, Y. Wang, Y. Li, Yi Chen, N. A. Abbasi, T. Kürner, A. F. Molisch "Terahertz Wireless Channels: A Holistic Survey on Measurement, Modeling, and Analysis" IEEE Communications Surveys & Tutorials, vol.24, no2, third quarter 2022

[**Her2025**] Christoph Herold , Thomas Kürner, "A Concept for the Efficient Integration of Reconfigurable Intelligent Surfaces into a Ray Tracing Framework", 48th IRMMW-THz, Montreal, 2023

[**Hua2018**] Hongji Huang, Jie Yang, Hao Huang, Yiwei Song, and Guan Gui, "Deep Learning for Super-Resolution Channel Estimation and DOA Estimation Based Massive MIMO System", IEEE Transactions on Vehicular Technology (Volume: 67, Issue: 9, September 2018)

[**IEEE802.15**] https://mentor.ieee.org/802.15/documents?is_dcn=ChannelTransfer&is_group=003d

[**Kir2021**] Anil Kirmaz, Diomidis S. Michalopoulos, Irina Balan, and Wolfgang Gerstacker, "LOS/NLOS Classification Using Scenario-Dependent Unsupervised Machine Learning", IEEE PIMRC, Helsinki, Finland, September 13-16, 2021.

[**Lem2021**] Filip Lemic , Sergi Abadal, Wouter Tavernier, Pieter Stroobant , Didier Colle, Eduard Alarcón, Johann Marquez-Barja, and Jeroen Famaey, "Survey on Terahertz Nanocommunication and Networking: A Top-Down Perspective", IEEE JOURNAL ON SELECTED AREAS IN COMMUNICATIONS, VOL. 39, NO. 6, JUNE 2021

[**Li2021**] Li, Xianjin, et al. "Integrated sensing and communication in 6G: The deterministic channel models for THz imaging." 2021 IEEE 32nd Annual International Symposium on Personal, Indoor and Mobile Radio Communications (PIMRC). IEEE, 2021.

[**Liu2022**] Liu, An, et al. "A survey on fundamental limits of integrated sensing and communication." IEEE Communications Surveys & Tutorials 24.2 (2022): 994-1034.

[**Loe2025**] Lorenz H. W. Loeser, Thomas Kürner "Towards a Heuristic Path Loss Model for RIS Links" URSI-B EMTS 2025, Bologna, 23–27 June 2025.

[**Jae2014**] S. Jaeckel, L. Raschkowski, K. Borner, and L. Thiele, "Quadriga: A 3-d multi-cell channel model with time evolution for enabling virtual field trials," IEEE transactions on antennas and propagation, vol. 62, no. 6, pp. 3242–3256, 2014.

[**Ju2023**] S. Ju and T. S. Rappaport, "142 GHz Multipath Propagation Measurements and Path Loss Channel Modeling in Factory Buildings," in ICC 2023 - IEEE International Conference on Communications, 2023, pp. 5048–5053.

[**Mol2012**] Molisch, Andreas F. Wireless communications. Vol. 34. John Wiley & Sons, 2012.

[**Ngu2022**] Dinh C. Nguyen, Ming Ding, Pubudu N. Pathirana, Aruna Seneviratne, Jun Li, Dusit Niyato, Octavia Dobre, and H. Vincent Poor, “6G Internet of Things: A Comprehensive Survey”, IEEE INTERNET OF THINGS JOURNAL, VOL. 9, NO. 1, JANUARY 1, 2022

[**Pen2015**] B. Peng, T. Kürner “A Stochastic Channel Model for Future Wireless THz Data Centers” 2015 International Symposium on Wireless Communication Systems (ISWCS), 25-28 August 2015.

[**Pet2020**] V. Petrov, T. Kurner and I. Hosako, "IEEE 802.15.3d: First Standardization Efforts for Sub-Terahertz Band Communications toward 6G," in IEEE Communications Magazine, vol. 58, no. 11, pp. 28-33, November 2020, doi: 10.1109/MCOM.001.2000273

[**Pri2013-1**] S. Priebe, M. Kannicht, M. Jacob, and T. Kürner, “Ultra broadband indoor channel measurements and calibrated Ray tracing propagation modeling at THz frequencies,” submitted to J. Commun. Netw., 11 pages, 2013.

[**Pri2013-2**] S. Priebe, T. Kürner "Stochastic Modeling of THz Indoor Radio Channels", IEEE Transactions on Wireless Communications, vol. 12, no. 9, pp. 4445-4455, September 2013.

[**Ram2018**] Mohammed Ramadan, Vladica Sark, Jesús Gutiérrez and Eckhard Grass, “NLOS Identification for Indoor Localization using Random Forest Algorithm”, WSA 2018; 22nd International ITG Workshop on Smart Antennas

[**Rec2021**] Recommendation ITU-R, “Effects of building materials and structures on radiowave propagation above about 100 MHz,” P.2040-2, 09/2021

[**Rey2017**] S. Rey, J. M. Eckhardt, B. Peng, K. Guan, T. Kürner “Channel sounding techniques for applications in THz communications: A first correlation based channel sounder for ultra-wideband dynamic channel measurements at 300 GHz," 2017 9th International Congress on Ultra Modern Telecommunications and Control Systems and Workshops (ICUMT), Munich, Germany, 2017, pp. 449-453

[**Ron2015**] O. Ronneberger, P. Fischer and T. Brox, "U-Net: Convolutional Networks for Biomedical Image Segmentation", MICCAI 2015.

[**Sar2018**] R. Saravanan and P. Sujatha, “A State of Art Techniques on Machine Learning Algorithms: A Perspective of Supervised Learning Approaches in Data Classification,” in 2018 Second International Conference on Intelligent Computing and Control Systems (ICICCS), 2018, pp. 945–949.

[**TIMES2023**] SNS TIMES Deliverable D4.1 - intermediate report on PHY layer enhancements for THz links supporting sensing and communication functionalities, 2023.

[**TIMES2023-2**] SNS TIMES Deliverable D3.1 - Initial channel measurements in industrial environments at sub-THz frequencies, 2023.

[**TIMES2023-3**] SNS TIMES IR3.1 State-of-art Channel Models in industrial environments at sub-THz frequencies, 2023.

[**TIMES2023-4**] SNS TIMES D2.2 Definition of scenarios for software simulation, 2023

[**TIMES2024**] SNS TIMES IR5.1 Initial prototypes of antennas and IRS, 2024

[**TIMES2025**] SNS TIMES IR3.3 Intermediate Report on Channel Measurements in Industrial Settings with IRS at Sub-THz Frequencies, 2025

[**TIMES2025-2**] SNS TIMES D3.2 Channel Measurements in Industrial Settings with IRS at Sub-THz Frequencies, 2025

[**Tre2002**] Harry L. Van Trees. Optimum Array Processing: Part IV of Detection, Estimation, and Modulation Theory. Wiley, 2002. isbn: 978-0-47109390-9. doi: 10.1002/0471221104.

[**Vit2015**] E. M. Vitucci, V. Degli-Esposti, F. Fuschini, J. S. Lu, M. Barbiroli, J. N. Wu, M. Zoli, J. J. Zhu, and H. L. Bertoni, "Ray Tracing RF Field Prediction: An Unforgiving Validation," International Journal of Antennas and Propagation, vol. 2015, pp. 1–11, 2015.

[**Wan2019**] Jing-Ling Wang, Yun-Ruei Li, Abebe Belay Adege, Li-Chun Wang, Shiann-Shiun Jeng, Jen-Yeu Chen, "Machine Learning Based Rapid 3D Channel Modeling for UAV Communication Networks", 2019 16th IEEE Annual Consumer Communications and Networking Conference, CCNC 2019.

[**Xin2021**] Y. Xing et al., "Millimeter wave and Sub-THz indoor radio propagation channel measurements, models, and comparisons in an office environment," IEEE Communications Letters, vol. 25, no. 10, 2021.